UNIVERSITY OF CALIFORNIA, SAN DIEGO

The Importance of Landslides and Flooding Events in Harvesting and Sequestering Macroscopic Carbon along Active Margins: The Eel Basin, Northern California

A thesis submitted in partial satisfaction of the requirements
for the degree Master of Science

in

Earth Sciences

by

Justin S. McCullough

Committee in charge:

Professor Neal Driscoll, Chair
Professor Lisa Tauxe
Professor Graham Kent

2009

The Thesis of Justin S. McCullough is approved, and it is acceptable in quality and form for publication on microfilm and electronically:

_____

_____

_____

Chair

University of California, San Diego

2009

TABLE OF CONTENTS

LIST OF FIGURES

LIST OF TABLES

ACKNOWLEDGEMENTS

I'd like to thank, first and foremost, my advisor, Neal Driscoll, for the many educational and financial opportunities given to me during the past three years. Working alongside Neal is always intoxicating, sometimes quite literally, for he makes learning enjoyable and has many exciting ideas and funny stories.

I'd also like to thank Graham Kent and Lisa Tauxe for being such great teachers and allotting their time towards being on my committee.

Thank you to the entire Driscoll Lab for creating a warm environment in which we could all share scientific ideas.

Thanks to Caren Duncanson, Pam Buaas, and Jane Teranes for always being so helpful and kind while guiding me through the Earth Sciences program as both an undergraduate and masters student.

I'd like to thank Professor Dariusz Stramski for allowing me to use his laboratory and Vanessa Wright, Julia Uitz, and Florence Lahet who were never hesitant in helping me with whatever I needed in his lab.

Thanks to Kurt Schwehr for assisting me with the startup of this project and sharing his knowledge of, and data from, the Eel margin. Also, thank you to Alex Hangsterfer for showing me the operational methods of using the Coulter Counter and to Niki Bilsley for collecting the grain size data for the entirety of core 07PC.

I thank my parents Judy Adamson and Kenneth and Cheryle McCullough for always supporting and trusting all of my endeavors.

Lastly, thank you to my girlfriend, Mary Gillespie, who has helped me greatly with the emotional struggles I had while finishing this thesis.

This thesis, in part, is currently being prepared for submission for publication of the material. McCullough, Justin S.; Driscoll, Neal W. The thesis author was the primary investigator and author of this material.

ABSTRACT OF THE THESIS

The Importance of Landslides and Flooding Events in Harvesting and Sequestering Macroscopic Carbon along Active Margins: The Eel Basin, Northern California

by

Justin S. McCullough

Master of Science in Earth Sciences

University of California, San Diego, 2009

Professor Neal Driscoll, Chair

Roughly half the sediment that flows into the oceans is delivered by small rivers that drain tectonically active mountain belts. Their high sediment yield implies that a disproportionately high fraction of particulate organic carbon is also delivered to the oceans by these rivers. The fate of the coarse grained particulate carbon derived from living and soil biomass, which originates as fixed atmospheric carbon, is an important but

poorly understood issue. Only by landsliding, triggered by heavy rainfall or earthquakes, will significant amounts of fresh, modern carbon be exported from mountain belts. Flood discharge from severe storms efficiently transports the organic matter from steep, mountainous catchments to adjacent oceans as turbidity currents. The resultant deposits are a potential proxy for landslide occurrence and large flood events. Rapid burial in subsiding offshore basins makes active continental margins prime settings for significant organic carbon sequestration. To demonstrate these concepts, new core data is presented, along with existing geophysical data from the offshore Eel basin, northern California. Rapid burial of terrestrial organic matter derived from coastal mountains occurs in growth synclines and slope basins that have been actively accumulating sediment for millions of years. Significant preservation of biomass-derived carbon in offshore depocenters at active margins has wide implications for longer-term carbon budgets, essentially because the living biomass represents a renewable carbon resource that can be transferred from the biosphere to the lithosphere.

Introduction

1. Introduction

The numerous small drainage basins of wet, tectonically active mountain belts have high sediment yield because of rapid hillslope erosion and efficient river transport [4, 36, 60]. Mass wasting is an erosional agent characteristic of rugged orogenic terrains, where large storms [35, 36] and major earthquakes [41, 71] trigger swarms of landslides (Figs. 1 and 2). Slope failures remove vegetation, soil and bedrock from hillsides, and transport this mix of debris towards the base of hillslopes and into channels (Figure 3). Landslides constitute a major mechanism not only for erosion, but also for forest disturbance [2, 25, 28, 85] and the physical removal of biomass. The bulk of sediment yield in montane catchments occurs during storm-generated flood discharge, and in such cases sediment transport is largely contemporaneous with sediment supply. However, landslides triggered by earthquakes often do not connect directly to the valley floors, depositing debris instead on hillslopes [77]. In addition, coseismic failures may dam rivers if discharge is insufficient to mobilize debris in the channel (Figure 4). In either case, a delay is introduced between sediment production and transport, and sediment remobilization occurs during subsequent storms [71, 81]. Nevertheless, almost all the mass-wasted debris is routed through and out of mountain belts by storm flows on time scales of tens to thousands of years [5, 36, 71, 75, 81].

The focus of this work is the fate of modern biomass-derived organic matter liberated by mass wasting in orogenic belts (Figs. 1 and 2). Is most of the modern organic carbon mineralized (respired) back to the atmosphere, or does a significant fraction of this organic matter survive transport and burial to enter the geological reservoir? If it is preserved, what can be inferred about the processes of carbon liberation, transportation,

and sequestration? Rapid erosion accomplished through mass-wasting, efficient fluvial transport and potential for rapid burial in subsiding offshore basins suggests to us that active continental margins constitute prime settings for significant sequestration of biomass-derived organic carbon.

1.1 Organic carbon export from mountain belts

Landslides in mountain belts strip soil and bedrock from hillslopes, remove standing biomass, break up stem material, and mix the resulting biomass carbon with carbon from soils and bedrock, as well as with inorganic debris [2, 25, 28, 85]. It is therefore worthwhile to inventory the different sources of organic carbon in such terrains, and to outline how to distinguish these components in the resulting sediment discharge. These components will be somewhat modified during transport and deposition by exchange with the surficial (ocean and atmosphere) carbon reservoirs. The two main organic carbon pools are the fresh or modern carbon contained in the living terrestrial biomass, and the old or fossil carbon contained in the bedrock [42, 43, 74]. Soils represent a mixed layer comprising weathered bedrock chiefly at the base and sub-fossil biomass (humus) near the surface. Oxidation can occur in aerated soil and colluvium.

In mountain belts, the most important hosts for kerogen, the fossil form of organic carbon, are fine-grained marine mud-rocks and their metamorphic equivalents (e.g., [33, 89]). The average organic carbon content of marine shale worldwide is 1% by weight [50, 89]. The kerogen dispersed in these fine-grained muddy rocks is largely unreactive (refractory), old (essentially infinite age by ^{14}C), with elemental ratios (such as C:N) and ^{13}C isotopic signatures that depend on the origin (terrestrial or marine) and thermal

maturity of the organic material [89]. Compared to the fossil carbon from bedrock, living terrestrial biomass yields detrital carbon that is reactive, young (present-day ^{14}C age), with elemental ratios (e.g., C:N) higher than kerogen, and ^{13}C isotopic signatures that are generally lighter [48]. These and other chemical analyses have been conducted on key organic compounds (biomarkers) in soils and sediments to determine the source of organic matter found in offshore sediment cores [20, 74].

To compare the relative abundance of the biomass and fossil carbon pools in humid mountain belts, a representative biomass density for montane forest of 400 t/Ha is assumed (e.g., [7]). The living biomass on hillslopes will then contain approximately the same amount of carbon as the kerogen dispersed in about a 1m thick layer of bedrock. Therefore, the fresh biomass carbon component of fluvial sediments will be heavily diluted by bedrock fossil carbon in mountain belts where bedrock landsliding is prevalent. Bedrock landsliding might explain, at least partially, the old (>10,000yr) ^{14}C ages for suspended sediment in rivers draining some orogenic belts, such as Taiwan [40]. It is emphasized here, however, that only through mass wasting (Figure 1 and 2) will significant amounts of carbon from living biomass be eroded from mountain belts. Other erosional processes like rilling and sheet wash concentrate in the soil layer, and mainly extract the sub-fossil biomass (humus) and weathered bedrock components of the available carbon sources.

In addition to their chemical differences, the modern biomass carbon and the fossil kerogen tend to be concentrated in distinctly different size fractions of sediments fluxed from mountain belts. Biomass carbon debris (living and soil) generated through landsliding is generally associated with the coarse size fraction [48, 49]. Indeed, vascular

plant remains are the dominant form of particulate organic carbon (POC) in sand-size and coarser material (>63μm), reaching concentrations of a few weight percent [48, 49]. On the other hand, the kerogen component is adsorbed on to the surface of clays (<3μm; [33, 43]). Recent research has shown that the clay-bound kerogen carried by big rivers is modified by exchange with the surficial carbon reservoirs during offshore transport and deposition (see [42] and below), however, along active margins this exchange appears limited [48]. If this is correct, at active margins the refractory organic carbon component is basically recycled from bedrock reservoir back to bedrock reservoir without significant modification en route. The living and sub-fossil biomass, which originates as fixed atmospheric carbon, is exported by landsliding and fluvial processes from the mountain system (see below), and is deposited with the coarse grained sediment fraction at active continental margins [48]. However, the significance of this component in terms of the long-term global carbon budget is poorly understood at present.

The small rivers that deliver large quantities of sediment and biomass carbon from active orogens typically drain either onto a narrow shelf or directly into a deep ocean basin [35, 36, 60, 65, 75]. Few of these rivers discharge through substantial flood plains, deltas, estuaries or wide continental shelves, where a large proportion of organic carbon can be oxidized and returned to the atmosphere [3, 42], as discussed later. The final factor needed for effective sequestration of the biomass carbon is rapid burial in proximal depocenters. Hedges and Keil [33] suggest that shallow marine deltas account for 45% of organic carbon burial globally, while the remainder of continental shelf areas account for another 45%. Hydrodynamic sorting of sediment sizes in the offshore implies that the fresh particulate biomass carbon will be deposited in nearshore deltas with the coarse

fraction, whereas the clay-bound kerogen will be distributed more broadly across the shelf and into deeper water with the fine fraction. A particular virtue of active continental margins is that tectonic activity produces structurally controlled subsiding depocenters, which provide accommodation space for the preservation of organic carbon supplied to the margin from adjacent coastal ranges [19]. One active margin was selected to attempt to characterize and quantify the trapping efficiency of sediment and the preservation potential of biomass organic carbon over geologically significant time scales: the Eel River margin of northern California (Figure 5).

1.2 Carbon transport to and burial in active margin depocenters

New marine geophysical and recently published sediment geochemistry data from the Eel River basin, offshore northern California, are combined to show that sands delivered to the margins are rich in particulate organic carbon in the form of fresh plant debris [48, 49], and that this organic matter is preserved in shelf and slope depocenters.

The basin is situated in a tectonically active convergent margin that allows for erosional processes to dominate. The continual encroachment of the northward migrating Mendocino triple junction produces transpressional regional uplift identified by a series of folds and thrust faults (Figure 6). Onshore, uplift rates are as high as 4mm/yr, resulting in cliff elevation and exposure of subsurface rocks [65, 66]. The Eel River delivers sediment from a relatively small, rugged catchment, with a drainage area of 8640km^2 and a maximum elevation of 2000m [65]. Both the Eel and the Mad River to the north discharge into the basin and occupy subsiding synclines striking NNW across the Gorda/North American convergent plate margin. The Eel River has the highest sediment

yield, relative to its drainage basin area, in the contiguous United States, contributing approximately 90% of the total sediment budget [60, 84]. The Eel River traverses mostly through the Mendocino Range (northern Coast Range) and minimally in the western belt of the Klamath Mountains to the northeast. Both ranges are composed of underlying Cretaceous deep-water sedimentary and mafic marine volcanic rocks of the Franciscan Formation, which include highly sheared, unstable serpentinites. Overlying the Franciscan Formation are Tertiary sedimentary mud- and siltstones with alluvial deposits interspersed [8, 66]. It is earthquakes and steepening of folds, creating fractured and brecciated rocks, in highly active tectonic regions, like that of the Eel margin, that lead to slope failures and sediment mobility, promoting the transport of large quantities of sediment offshore [60, 69].

Over the past 80 years the gauging station at Scotia (Figure 5C) has recorded annual total suspended sediment (TSS) discharge ranging from 10-30Mt/y for silt and clay [84, 88]; fine sand and coarser suspended sediment averages about 25% of TSS [83], and bedload has been estimated at approximately 10-20% of TSS [8]. The data show a strong annual correlation between the average suspended sediment load and annual water discharge of the Eel River (Figure 7A)[84]. Also, annually averaged discharge of the Eel River and precipitation over the coastal mountains of northern California have been documented for the time period between 1930 and the early 1990's and show a strong correlation (Figure 7B). Snowfall in the region is minimal and its contribution to runoff in the Eel River is usually insignificant [8]. This results in a coherent relationship between discharge and precipitation, in which the majority of rainwater has no residence time and rapidly flows downhill. This is an important factor controlling the sediment

budget of the Eel margin. Coherency allows for high water discharge during storms and, hence, large amounts of sediment, to enter the ocean when there exists large storm waves offshore. Storm waves facilitate across shelf transport that leads to a greater propensity of hyperpycnal flows to carry a large percentage of the suspended sediment load past the relatively narrow shelf, which extends 10-20km offshore.

The Eel River is a storm-dominated system where most sediment is discharged during winter floods [84]. For example, the 1995 Eel River flood alone delivered 25Mt of suspended sediment, about one eighth of the annual TSS discharge from the Mississippi [60]. In addition, ~0.24 Mt of terrigenous particulate organic carbon (POC) were discharged during this flood [49]. Based on data collected from the four major southern California rivers, it has been shown that small, mountainous rivers discharge hyperpycnal concentrations of sediment during such flood events. A hyperpycnal flow is one that is denser than the ambient fluid into which it flows and has been shown to have a critical concentration of ≥40g/L [92]. During a large storm flood event in the latter part of February 1969, these rivers exhibited instantaneous suspended sediment concentrations, recorded at 1 – 4 hour intervals, which breached the hyperpycnal threshold more regularly than daily averages. This revealed the character of hyperpycnal flows to be event driven on time scales of a few hours (also see 57). Similar to southern California rivers, Eel River discharge is dominated by event driven floods, which produce hyperpycnal plumes that flow along the seafloor and are capable of traveling great distances past the shelf, effectively depositing on the continental slope.

Sediment geochemistry, bathymetry and seismic reflection data acquired from the northern Californian shelf and slope as part of the STRATAFORM Program [65]

document the efficient transport and deposition of clastic sediments, including POC, sourced from coastal mountains. Two points can be deduced from the coring data: (1) During the 20th century, roughly 20% of the sediment has been trapped on the shelf between 50m and 150m, with another 20% deposited on the slope. The remaining 60% of the discharge is not accounted for and is either sequestered on the inner shelf in water depths less than 50m, or has bypassed the shelf and slope region and is delivered to the deep sea; (2) The coarse fraction is characterized by high concentrations of vascular plant debris and carbon with ^{13}C values and C:N ratios indicative of terrigenous biomass carbon [48, 49]. Plant debris sand-sized and larger is primarily wood and is concentrated in close proximity to the river mouth (10-30km), where it comprises up to 2% of the surface sediment by weight in the region dominated by coarse sediment (>63μm). Farther offshore, at 70m water depth, the coarse (sand) fraction is <10% by weight, but accounts for approximately 25% of the total organic carbon of the surficial sediment [48]. Settling-velocity experiments show that the sand-sized plant fragments, even though less dense, sink at a rate similar to that of fine quartz sand, implying that a majority of the sand-sized and larger plant fragments predominantly accumulate in the subaqueous delta portion of the Eel Syncline [49] (Figure 5). The aerial distribution of the sands deposited in the Eel subaqueous delta is roughly delineated by the seaward deflection of the 50m bathymetric contour (Figure 3C). Less than 3% of the annual Eel/Van Duzen sediment load is deposited in the subaerial deltas [84].

On the upper continental slope approximately 50km north of Cape Mendocino, between 250 – 600m water depths, exists a large failure [21]. This failure, the Humboldt Slide, lies within a subsiding, shallow bowl shaped depression that has been functioning

as a depocenter for terrigenous sediment [69]. Present near the toe of the slide are wavy bed-forms originally thought to be formed by retrogressive failure and rotation during a mass-wasting event [24]. To assess the true origin of these features, Schwehr et al. (2007) analyzed the sedimentary fabric characterized by anisotropy of magnetic susceptibility. It was shown that these sediment waves (Figure 8) were not a consequence of post-depositional deformation, but were in fact primary depositional features and a possible depositional site for the missing Eel River sediment budget, for which only 40% is accounted (see 1). The Humboldt slide is a good candidate for deposition because its location is seaward of a relatively narrow shelf ~30km northwest of the Eel river mouth and net bottom flows are dominantly northward and seaward during storms when most sediment is transported offshore [67].

High-resolution chirp seismic data **(**Figure 5A**)** show that the Holocene sediment thickness varies markedly along the Eel margin in response to active tectonic deformation, and ranges from a few meters over anticlines to greater than 40m in the Eel Syncline [19]. Multi-channel seismic and exploratory well data along the Eel margin (Figure 5B) show that this deformation is long lived and has accommodated sediments discharged by the Eel River on time scales of millions of years (15 My)[17]. The sequestered organic matter in the Eel Syncline is thus removed from the short-term carbon cycle because continued subsidence protects the deposited sediments from subsequent erosion associated with glacial sea level fluctuations. Furthermore, the seismic data also indicate that the bathymetry and subsurface structure are not well correlated (Figure 5). The seismic data reveal a large depocenter on the Eel Shelf, a repository not recognized using bathymetric data alone. This has led other researchers to

believe that river-borne sediment discharge bypasses the narrow shelves along active margins, and therefore to underestimate the importance of active margins as long-term repositories of terrigenous organic carbon.

Rapid sediment burial rates and the high likelihood of organic carbon preservation within those sediments are also indicated by the obvious presence of gas in the section (Figure 5). Anomalously low backscatter in side scan sonar data from the region of the subaqueous delta has been attributed to shallow gas [19]. Analysis of surface sediment cores shows that most of the gas along the Eel margin is biogenic in origin [22], generated by microbial reduction of the sedimentary organic matter to methane. Methanogenesis occurs only if burial rates are high enough to prevent oxidation of organic matter as it passes through the sulphate redox zone in the shallow subseafloor. The delivery of most of the organic carbon to the shelf in storm deposits, a feature the Eel has in common with other active margins, satisfies this requirement.

This “Introduction” chapter, in part, is currently being prepared for submission for publication of the material. McCullough, Justin S.; Driscoll, Neal W. The thesis author was the primary investigator and author of this material.

Methodology

2. Methodology

In 2001, 7 large-diameter (~10cm) piston cores were acquired from the Eel River Basin during R/V Thompson cruise TTN136B. Three cores were selected for this study on the basis of their locations at the toe of the Humboldt slide within a discrete sediment wave discussed above (Table 1). A visual analysis and description for each core was conducted that included: lithographic depiction, color (using a Munsell Soil Color chart), approximate grain size from visual analyses, and presence of POC. The core sites were determined using differential GPS, yielding ≤10m accuracy [78]. Core 01PC recovered almost 8m of sediment, however, during retrieval, an unknown length in the middle of the core was lost overboard. The missing section was subsequently labeled section 5 and assumed to be ~10cm (pers. comm., Kurt Schwehr). Because the length of the jettisoned piece of core is not known accurately, only the first 508cm, which overlies the missing section, was used for this analysis. Also missing from core 01PC is the top ~200cm of sediment due to over-penetration of the corer. This was initially determined by a comparison with the corresponding trigger core, which cannot be correlated with the piston core, and later confirmed with radiocarbon dating. The lengths of cores 02PC and 07PC are 786.5cm and 755cm, respectively, and lack voids within all sections. Comparison of piston and trigger cores reveals that cores 02PC and 07PC are almost complete and only missing ~5cm from the surficial sediment (Figure 9, Table 1).

Sediment samples were collected at ~20cm intervals for the entire length of cores 02PC and 07PC and for the upper 508cm of core 01PC. Upon further examination, it was apparent that the cores display a repeating depositional pattern. That is, the layers exhibit normal grading separated by distinct coarse-grained packages that often had sharp

erosional bases. These fining-upward packages were on the order of tens of centimeters thick. Within some of these packages, a transition from coarse to fine sediment was noted. To confirm that these layers were characterized by normal grading, additional samples were collected at the top and base of each package. Each sample was approximately 50 g, spanning a depth of 1.5 – 2.5cm. The samples were weighed before and after being dried at 80 – 100°C in order to determine the water weight of each sample. The water weight was multiplied by 3.5%, the amount of salt in seawater, to determine the true mass of the sediment. The dried sample was then wet sieved at 63μm using distilled water and a rubber policeman to disaggregate cohesive clay minerals. Sieving continued until it was no longer apparent that sediment was passing through the sieve. The fine-grained material was funneled into a brown mason jar and refrigerated to prevent authigenic mineral and biotic growth. Due to time constraints, only a portion of the fine-grained material of samples from core 01PC (20 of 51) and 02PC (56 of 71) were further analyzed. The remaining coarse sediment was dried again and weighed to determine the coarse weight percentage of each sample (Tables 2 and 3).

The fine fraction of each sample was analyzed using a Beckman Coulter Multisizer™ 3 Coulter Counter®, following the methodology of Poppe et al. (2003), to produce a detailed grain size spectrum. A pipette was used to add the fine sediment-water mixture to an electrolyte solution, in this case thrice filtered seawater at .2μm, until a suspended sediment concentration of 2 – 3% was obtained, measured by the machine. The machine operates as follows. As a grain travels through an aperture separating two electrodes between which an electric current flows, electrical impedance is produced. This impedance is measured and converted to a voltage pulse that is proportional to the

volume of the grain that produced it. The software assumes each particle is spherical. At least three baselines were measured before any sediment was added, which would then be averaged and subtracted from each sample run to determine the actual grain size distribution. For each sample, typically three runs were obtained and the software determined an average. Because each aperture can only size particles from 2 – 60% of the aperture diameter, two apertures were utilized; the 200 and 30μm apertures. Therefore, the size range of which the machine can size grains using these two apertures is .6 – 120μm. After analyzing with the 200μm aperture, the fine sediment-water mixture was sieved at 20μm before analysis with the 30μm aperture began. The averaged runs for each aperture were combined using the Multisizer 3 software, which allows the user to bin the data into multiple size ranges of the user's choice. Before completing all samples for core 02PC, the coulter counter had undergone maintenance, effectively biasing the data. This occurred after analyzing sample 26 at 361cm depth in the core.

Pelagic and benthic species of foraminifera were picked from the coarse fraction of each sample. Calcareous tests of planktonic organisms were also periodically sampled from the core, when visible, and lightly washed. Due to the mixing of old, upwelling ^{14}C depleted oceanic waters with ocean surface waters and a delay in the exchange rates between atmospheric carbon dioxide and ocean bicarbonate, it is essential to correct radiocarbon dates obtained from marine carbonates. A correction of 350 years was used as a reservoir correction on dates measured by the National Ocean Sciences Accelerator Mass Spectrometry (NOSAMS) Facility at Woods Hole Oceanographic Institution. The correction was linearly interpolated between the locations of Sunset Bay, Oregon (ΔR 437yr) and Bolinas Bay, California (ΔR 232yr), which are part of the radiocarbon

calibration curve of the Marine04 database [37]. Lab reported ages indicate radiocarbon years before present, where present corresponds to AD 1950. Twelve unspecified marine carbonate samples from core 01PC and 20 unspecified marine carbonate, 9 foraminifera, and 10 particulate organic carbon samples from core 02PC were radiocarbon dated (Table 4).

This “Methodology” chapter, in part, is currently being prepared for submission for publication of the material. McCullough, Justin S.; Driscoll, Neal W. The thesis author was the primary investigator and author of this material.

Results

3. Results

Deposition on the Humboldt slide has preserved thick layers of vascular plant debris, which are not observed in other cores acquired along the Eel Margin [14, 48, 49, 83, 84]. Pulverized terrestrial plant debris is prevalent throughout all three cores, representing at least a couple percent particulate organic carbon (POC) by volume, based on visual estimations. The cores also exhibit many distinct layers consisting of >90% POC by volume, ranging from less than half a centimeter to approximately 8cm (Figure 10B). The majority of this POC is vascular plant debris. Observed within some of the organic layers are pieces of wood several centimeters in length (Figure 11), suggesting transport by hyperpycnal processes. There are a total of 16, 20, and 11 layers that are almost entirely POC in cores 01PC, 02PC, and 07PC, respectively (Table 5).

The downcore volumetric distribution of the fine-grained sediment fraction does not exhibit significant variability, however, the coarse weight percent (>63 μm) distributions show a notable signature (Figure 12, Table 2, Appendix). The visual analysis of the fining-upward packages in the cores is corroborated by the coarse grain-size data, which have a fining upward trend in a majority of these packages. Distinct, abrupt contacts are often observed at the base of the relatively coarse-grained sediment and the underlying fine-grained sediment. Nevertheless, not all packages show definitive normal grading or a distinct contact separating coarse- from fine-grained sediment. Some of these discrepancies may be the consequence of bioturbation with the burrowing activities of benthic organism in the sediment column obscuring the contact between packages. For example, seven of the eleven fining-upward packages that don't exhibit an abrupt change in the coarse weight percentage across the boundaries are bioturbated.

Upon examining all of the grain size data, two fining-upward boundaries initially defined by visual analyses from core 01PC were reinterpreted based on the coarse-grain size distribution. This grain size distribution also led to the addition of 1 and 3 fining-upward boundaries in cores 01PC and 02PC, respectively. After a complete analysis, it was determined that cores 01PC, 02PC, and 07PC have a total of 15, 18, and 19 fining-upward packages, respectively (Table 6).

Radiocarbon dates of marine carbonates, corrected for reservoir effects (350yr), were used to calculate sediment accumulation rates using least squares analyses for cores 01PC and 02PC (Figure 13). Accumulation rates at both core sites changed significantly between 2670 and 2510yrs BP. Core 01PC had a threefold sedimentation rate increase from .66mm/yr to 2.14mm/yr and core 02PC had a twofold increase from 1.74mm/yr to 3.60mm/yr. Wood samples were not used in the regression because it is possible for this organic material to be retained in river catchments for tens to hundreds of years before being transported offshore and deposited. Core 07PC was then correlated to core 01PC and 02PC using the grain size data.

Linear accumulation rates calculated from ^{14}C ages were used to date the fining-upward packages and the layers of POC (Table 7). The depths defining the bases of the POC layers and the fining-upward packages were used to calculate the time at which these event beds were emplaced. Given the range of ^{14}C ages, two lines with the same slope, representing the sedimentation rate, were determined in such a way to envelope 95% of the ^{14}C ages to place upper and lower age constraints on each event bed (see Figure 13). This proved to be the most conservative method for developing an age model because foraminifera and other marine carbonates were scarce throughout the core,

resulting in a limited and non-uniform distribution of radiocarbon ages. Some of the events had insufficient biological material in close proximity to secure radiocarbon dates and thus an accurate age estimate. Where possible radiocarbon dates above and below an event bed were used to define its age of emplacement. The most recent POC layer to be deposited in core 02PC was dated based on radiocarbon dating of a vascular stem within the layer (Table 4). The stem was calculated to have an age of 345 ± 30yr BP and this age was assumed to be the upper limit for the time of deposition of this POC layer. This layer probably represents the most recent Cascadia margin earthquake that occurred in AD 1700 (see discussion).

Based on the coarse grain size distribution, it was possible to spatially correlate the fining-upward packages of all three cores. The largest peak in the grain size data was used to correlate the three cores, with the interpolated radiocarbon dates for cores 01PC and 02PC used as an independent check on the accuracy of the correlation. The radiocarbon dates of the fining-upward package that contains the largest percent of coarse-grained material observed in cores 01PC and 02PC have similar ages and provide confidence that the correlation based on grain size is robust. The POC layers within the overlapping sections of cores 01PC and 02PC are also in agreement with the core correlation (Figure. 14). The number of fining-upward packages for the time interval of overlap between the two cores (~3800 – 2400yr BP) increases landward with core 01PC having 8 fining-upward packages and core 02PC having 12 fining-upward packages (Figure 8). The systematic increase in the number of fining-upward packages in a landward direction is consistent with sediment accumulation rates across a sediment wave (Figure 8). Sediment waves, or antidunes, migrate upslope and upcurrent towards

the sediment source [46], with sediment accumulation being most rapid on the stoss side, or upslope limb. Such a growth pattern, with a more complete section being deposited on the stoss side and a less complete section on the lee side, is predicted by the lee wave model for antidune growth [23]. Core 01PC is located on the downslope limb of the sediment wave and has fewer fining upward packages than does core 02PC, which is located on the upslope limb of the same sediment wave (Figure 8). In addition to having more fining upward packages, the thicknesses of the individual packages in core 02PC and core 07PC are greater than those observed in core 01PC (Figure 15A).

A marked change in accumulation rates is observed in both cores at ~2600yr BP (Figure 13). Accompanying this change in accumulation is a change in the thickness of the fining-upward packages as well as their duration. After 2600yr BP the observed packages are all thicker than 30 cm, whereas only about half of those deposited before this time are as thick (Figure 15B). Furthermore, the packages that are younger than 2600yr BP are all more than 190 years in duration, with an average of ~335yr. Those that are older than 2600yr BP span no more than 320yr and have an average of ~119yr. A 5-period moving average of the fining-upward packages older than 2600yrs BP shows a predominant peak at an age span between 90-100yr (Figure 15C).

This “Results” chapter, in part, is currently being prepared for submission for publication of the material. McCullough, Justin S.; Driscoll, Neal W. The thesis author was the primary investigator and author of this material.

Discussion

4. Discussion

4.1 Sediment yield

Precipitation, wild fires and earthquakes are three mechanisms that contribute to hillslope instability and the development of landslides in humid, forested, mountainous landscapes like that of the Eel River drainage basin. The abundance of particulate organic carbon (POC) deposited at the toe of the Humboldt slide in the Eel Margin reflects the interplay of these mechanisms. Here we explore the importance of these processes in the Eel River drainage basin.

4.1.1 Precipitation

Erosion is regulated by a variety of factors associated with soils, geology, topography, vegetation coverage, and climate [95], however, sediment entrainment into and transport within the fluvial system is dominated by precipitation events. Despite the mechanism of liberation, it is through rainfall that sediment is transported to channels and eventually to the offshore environment. Not only is rainfall needed to transport sediment through the routing system, it can also produce sediment by triggering landslides. During storm events, rainwater infiltrates porous, permeable soils and bedrock, increasing pore fluid pressures and increasing the weight of the sediment carapace. Pore pressures effectively reduce the normal stress [91] applied to the ground surface (due to gravity) and an increase in pore pressure reduces the frictional resistance between interparticle contacts. As soils and bedrock become oversaturated, the weight increases, as does the potential for landslides. The steep terrain in the Eel Basin and friable rocks of the Franciscan Formation make the watershed more susceptible to landsliding.

4.1.2 Wildfires

Sediment liberation and watershed behavior in forested landscapes are drastically altered as a result of wildfires. Burning results in the destruction of surficial vegetation through drying soil and the combustion of the understory and organic material that bind soil aggregates [10, 38, 39, 87, 95]. In many studies [11, 34, 38, 76, 87, 95], an increased occurrence of dry ravel, the physical movement of sediment due to gravity, is documented immediately following a fire as a result of the loss of binding organics. It is well documented that wildfires cause an increase in surficial erosion due to two processes that contribute to a reduction in soil infiltration rates: rain splash and soil hydrophobicity [38, 63, 87, 95]. The litter layer that is deposited on forest floors protects the underlying soil, stores water, and regulates infiltration. The loss of this protective layer can be detrimental to the health of soil because rain splash seals pores and is highly erosive [38, 63, 95]. As organic molecules volatilize within the soil due to intense heating, they condense on mineral soil particles resulting in a negatively charged layer that repels water [63, 87]. This repellency keeps water on the surface, diminishing the amount of water infiltrating into the soil. The reduction in water infiltration results in an increase of overland flow upon subsequent storms. Overland flow, or surface runoff, occurs rarely in fully vegetated landscapes [34, 54] due to infiltration, but causes accelerated erosion rates through sheetwash, rilling and gullying after a wildfire [6, 11, 38, 87, 95]. These erosional processes liberate large amounts of surficial sediment, and sediment yields the first year after a fire may be up to two or three orders of magnitude larger than from non-burnt areas [39, 63].

Much research has been conducted following wildfires for the study of the generation of debris flows, a mechanism of transporting large amounts of sediment to valley floors. There is general agreement that these debris flows are generated as overland flow collects sediment over large areas. As sheetwash converges to form rills and gullies, enough sediment is entrained to produce a debris flow [11, 95]. Increased runoff may also scour channels, incorporating wood and sediment from riverbanks [38, 55, 87, 95]. Debris flows documented as being caused "by failure of discrete landslides on hillslopes" (see 10) occur mostly in regions that experience some degree of tectonism, which plays a significant role in landslide initiation. Cannon and Gartner (2005) point out the importance of determining whether landsliding can be truly attributed to wildfires and not simply to extreme precipitation events. Shortly after a fire, when infiltration rates are low, it is improbable for saturation to occur to the degree that will trigger landsliding. Many months after a fire, however, vegetation mortality will result in diminished water repellency [9, 11, 55, 63, 87] due to reduced evapotranspiration [10, 54, 87] and increased root decay [10, 38, 55, 87, 95]. These factors will cause soil and bedrock to be more susceptible to landsliding, assuming revegetation of the landscape is relatively slow. Despite the potential for landsliding well after the occurrence of wildfires, surficial erosion processes dominate sediment liberation in the majority of the studied basins (76%; Cannon and Gartner 2005). In summary, wildfires generally increase the concentration of woody debris and sediment on slopes and in channels [87]. Channel deposits have the potential to dam rivers, as evinced in Idaho [55], the importance of which will be discussed below. The deposition of charcoal and charred debris is also

expected after wildfires and has been observed [34, 55, 56, 63], although few studies have described wildfire-related sediment deposits.

4.1.3 Tectonism and earthquakes

Most tectonism occurs at plate boundaries where folding, faulting and other modes of deformation of the lithosphere are prevalent, which increases elevation and slope that ultimately enhances the erodibility of bedrock. The transpressional tectonic regime typical of some convergent margins, which characterizes the Eel River drainage basin, results in extensive folding and faulting, creating narrow valleys and steep slopes. Shearing the bedrock during faulting and folding at relatively shallow depths (i.e., several km) generates internally fractured cataclastic rocks [91]. Highly fractured, friable bedrock is susceptible to failure in response to seismic activity and heavy precipitation [16, 29, 82]. Earthquake-triggered landsliding has been extensively documented and studied. For example, the 1999 Taiwanese Chi-Chi earthquake with a magnitude (M_w) 7.6 resulted in over 20,000 landslides. Although most landslides were confined to hillslopes [18], such events have the potential to fill the narrow valleys that are characteristic of tectonically active regions. These channel obstructions of bedrock, soil, and biomass effectively create natural dams. One such landslide (.125 km^3), occurring on Tsaoling Mountain, deposited 20% of the sliding volume into the valley of the Chingshui River, creating the .046 km^3 Tsaoling Lake (Figure 4)[13].

Many landslide dams are short lived. Of the dams studied by Costa and Schuster (1988) that were documented as failing, 80% had failed within 6 months of formation. Dam stability is, however, controlled by several variables, which include, but are not

limited to, dam height, dam volume, watershed area, and rock type. Many landslide dams have remained stable for hundreds of years or more. Those that do fail, most commonly fail through overtopping, when the height of the water reaches that of the dam, causing headward stream erosion and breaching of the dam [16]. When a dam fails, the energy stored behind the dam is released, resulting in extensive flash floods capable of causing intense damage to surrounding forests, entraining more sediment and biomass, and effectively pulverizing the sediment within the slurry as it travels downslope at great speeds (Figure 16).

Areas not subjected to landslides during an earthquake are likely to be preconditioned to fail due to the loss of cohesion and frictional strength. Ensuing rainfall may cause more landslides to occur. This was the case in Taiwan ~2yrs after the Chi-Chi earthquake during typhoon Toraji. The typhoon triggered ~30,000 more landslides, of which 80% occurred in areas that had not failed during the earthquake [18]. Using a model based on measurements of river discharge and suspended-sediment concentrations of the Choshui River, Dadson et al. (2004) estimated coseismic sediment supply to the river catchment independently of transport capacity. Sediment discharge into the ocean was 2.5 times greater during typhoon Toraji than when compared to concentrations during typhoon Herb, which occurred ~3yrs before the earthquake. This demonstrates that more sediment is liberated during precipitation events that occur after an earthquake than during precipitation events alone. In a case study of landslides in Humboldt County, California, data indicate the same, that the occurrence and magnitude-frequency of shallow landslides is greater after an earthquake (M_w >6) followed by precipitation than solely experiencing a large precipitation event [31].

All three mechanisms of sediment liberation – precipitation, wildfires, and tectonism – have the potential to decrease the strength of soil and bedrock making the hillslopes more susceptible to landsliding. Precipitation alone can produce landsliding if soil and bedrock become saturated to a depth at which increased pore fluid pressures and weight of the sediment carapace are large enough to overcome lithostatic pressures. Wildfires, through a reduction in evapotranspiration and root strength, may also cause mass wasting. The presence of burnt debris and charcoal would suggest that wildfires played a role in sediment production. Lastly, the continuous lithospheric deformation that is common at plate boundaries may result in diminished rock strength and increased hillslopes. This produces friable bedrock that is more susceptible to failure when disrupted by seismic activity (i.e., earthquakes) or by precipitation events.

Sediment cores acquired from offshore of the river mouth and across the Eel Margin show no evidence of burnt organic material. It is, therefore, difficult to invoke fires as the trigger mechanism for the liberation of vast amounts of POC observed in the cores. Delivery of the large deposits of vascular plant debris and bedrock to valley floors is most likely triggered by earthquakes and large precipitation events. This material may obstruct channels and, during subsequent winter storms, large precipitation events, in addition to causing landslides to preconditioned soil, will lead to the development of natural dams. Liberated material of the Eel River basin, including bedrock of relatively weak shale and mudstone, characteristic of the Franciscan Formation, will lack resistance to erosion and any dam constructed of this material will likely fail [47, 77]. The rapid failure of the dam and consequent flow might explain the thick layers of pulverized organic material observed in slope cores (01PC, 02PC, and 07PC).

4.2 Sediment deposition

Extending through the western regions of Northern California and entering the Pacific Ocean in central Humboldt County, the Eel River is an event-driven system, dominated by floods, that carries most of its annual sediment during a few days in the winter months. The coherency between precipitation and water discharge results in very turbid, and therefore dense, waters that create hyperpycnal flows upon entering the ocean. These flows play a large role in the transportation, burial and preservation of carbon in the form of terrestrial plant debris and kerogen that have been liberated from mountain slopes. Hyperpycnal flows deposit rapidly, on the order of several hours, and are capable of producing sediment packages many centimeters thick. Accumulation of sediment at such high rates allows for terrigenous carbon to be buried to depths were oxidation cannot take place or is at least limited [89]. Once buried tens of meters, this organic carbon becomes insolubilized and diagenetically altered to form kerogen. Therefore, the organic layers representative of floods are important predictors of methane gas generation for it is the pyrolysis of kerogen that produces methane. The discharge of methane through gas blowouts can play a significant role in slope failures and mass wasting, possibly generating tsunamis [19].

Large deposits of vascular plant debris, abundant throughout the cores, indicate the liberation of enormous amounts of biomass from montane catchments and it is concluded that through hyperpycnal processes the layers comprised of almost entirely POC are deposited in the deep ocean. As hyperpycnal flows travel across the seafloor, momentum is lost and the suspended sediment progressively settles out of the flow, depending on particle size and density; large, dense particles settle first, followed by finer

particles. The sand-sized pulverized plant material settles uniformly and deposits as layers of solely POC. To investigate hyperpycnal processes, researchers have studied the Choshui River and its offshore deposits. It has been estimated that two-thirds of the 143 Mt annual suspended-sediment discharge of the Choshui River following the Chi-Chi earthquake was transported under hyperpycnal conditions [18]. This was based on a post-earthquake suspended-sediment rating curve, and it was inferred that these hyperpycnal plumes developed at least four times after the earthquake, during the typhoon season. Based on the background suspended-sediment rating curve, the authors estimated that only one hyperpycnal event would have occurred if the earthquake had not ruptured. In order to document the impact of such hyperpycnal events on the seafloor, boxcore samples and CHIRP profiles were obtained before and after Typhoon Mindulle in 2004. Suspended-sediment measurements were also taken from Choshui River for the days before, during, and after the typhoon [58]. The data show that sediment concentrations (190 – 200g/l) breached the hyperpycnal threshold during the typhoon. The authors suggest that such high concentrations may be a result of landslide debris erosion and transport. Resultant changes in grain size and carbon source existed directly offshore of the river mouth. Before the typhoon, surficial sediments were mostly sand (97 – 100%) and C:N and ^{13}C values were indicative of a marine origin. After the passing of the typhoon, the amount of sand had significantly diminished (<5%) and organic ratios were then indicative of a terrestrial origin. The lack of coarse material suggests that typhoon derived sand had been transported to greater depths within hyperpycnal flows. This evidence from Taiwan supports the suggestion of the preservation potential of earthquake-driven geomorphic processes (i.e., landslides) in foreland stratigraphy [18]

and shows that hyperpycnal processes are capable of transporting terrestrial carbon past the continental shelf, paralleling what is seen on the Eel margin.

4.3 Carbon sequestration

Assuming the Eel margin is representative of active margins in general, the observations above suggest that, over time, significant amounts of biomass-derived carbon harvested by landsliding in the coastal mountains may accumulate in long-lived continental margin depocenters. It has been estimated that >10Gt/y of sediment is discharged from small mountainous rivers, most of which drain catchments that border the Pacific Rim [60]. This represents at least half the global sediment budget of 20Gt/y: the remaining half is delivered by a mere handful of very large river systems, such as the Amazon, the Ganges-Brahmaputra and the Yangtze [59, 60]. It is assumed that the same proportions apply to the discharge of organic carbon from montane catchments, i.e., ~0.1Gt/y, given a typical riverine POC content of about 1% by weight of TSS (e.g., [50]). Even though the global carbon and sediment fluxes from large river systems and small mountainous catchments might be similar, the processes and environments at the river mouths are markedly different. Large continental rivers typically flow across broad passive margins and their clastic and particulate organic loads travel through a sequence of alluvial, estuarine and deltaic environments. Estuaries efficiently trap and sort sediment [26, 53, 73], and tidal reworking of estuarine sediment tends to increase oxidation depth in the surficial sediment [96]. Thus, estuaries recycle carbon in a similar way to that observed on wide, tidally influenced shelves [3, 42]. In contrast, the lower reaches of active margin drainage systems, such as the Eel River margin (Figure 5), are

generally steep with small estuaries and narrow deltas. For such environments, most of the riverine particulate organic matter is efficiently transported and deposited without being reworked and oxidized. New carbon isotopic and C:N ratio data from the Eel margin clearly show that the clay-bound kerogen component of the Eel River discharge retains its terrigenous signature and is not replaced with marine carbon [48]. Even though the modern biomass carbon fraction borne by small mountainous rivers is more reactive than the kerogen, it also retains its terrigenous signature [48], thus indicating significant transfer of carbon from the biosphere into the lithosphere.

An upper bound for the flux of biomass carbon eroded by landsliding in active mountain belts is derived and compared to other carbon fluxes. Globally, $2 – 3 \times 10^3$Gt of organic carbon reside in terrestrial plant tissue and soil humus [33, 68]. About 10% of this carbon resides in the productive environments of humid, tropical to temperate mountain belts, based on the global distribution of forest cover. The landslides that occurred in the northern Venezuelan coastal mountains (Figure 1) and in central Taiwan (Figure 2) are the response to extreme rainfall and earthquake triggering events, respectively. On the order of 10% of the standing biomass has been removed by landsliding in these two particular examples. On average, one to two high magnitude flash flood and landslide events per century have occurred in northern Venezuela since the 17th century [45]. Similarly, landslide-generating earthquakes as large as the 1999 Chi-Chi event occur about twice per century [79] (although it should be noted that much landsliding in Taiwan is caused by the 2 – 3 typhoons that strike the island on average each year [36]).

Previous studies reported landslide disturbance rates of one to several percent per

century for mildly active areas like Puerto Rico [28] and Central America [25], to >10% per century for highly active mountains like Papua New Guinea [70, 80]. Taking 10% per century as a representative disturbance rate, a landslide rotation period of 1000 years is obtained. This return period compares to an average in situ tree replacement interval of 100 years [25], and natural wildfire rotation periods of a few hundred years for tropical rainforests [15]. Thus, an upper bound on biomass carbon supplied by landsliding in mountain belts would be around 0.1 Gt C/y, a figure comparable to the annual rate of global POC discharge estimated for small, mountainous catchments. Even though this upper bound to biomass carbon production rate is equivalent to all of the organic carbon delivered by small rivers, it is clearly an over estimate because some will be respired during transport and deposition, and some will be sequestered in terrestrial depocenters. The biomass carbon yield rate by landsliding is an order of magnitude smaller than present day human-induced burial rates estimated for wetlands, agricultural lands and similar anoxic terrestrial sinks [86]. Despite the present-day order of magnitude difference, the landslide generation process is a mechanism for carbon sequestration that has operated at active continental margins over much of geologic time.

4.4 Recorded processes

The fining-upward packages and layers of POC document major changes within the river system. The POC layers may record onshore landsliding, events that are short lived and capable of liberating the large amounts of biomass from hill slopes required to deposit such thick layers of organic material observed in the cores. The fining-upward packages, on the other hand, record long term changes due to climate variability.

Radiocarbon dating of biological material present in the cores made it possible to calculate rates of sediment accumulation on the Humboldt Slide. Using these rates, the fining-upward packages and POC layers were individually dated.

4.4.1 Earthquakes

Landsliding in the Eel River drainage basin is partly enhanced due to continuous deformation of the lithosphere. It is quite possible that the layers of POC represent onshore earthquakes, causing landslides that liberate biomass and sediment. Dammed river channels often result in flashfloods, commonly arising from overtopped natural dams, which pulverize organic material en route to its deposition in the ocean. In this scenario, those POC layers in close proximity to one another probably represent one earthquake's sediment yield that has been distributed by multiple surges during successive storm events during winter seasons. The organic layers increase in frequency and magnitude downcore, suggesting that landslides, and potentially earthquakes, occurred more frequently in the past.

In order to assess whether Holocene Cascadia earthquakes are recorded at the Humboldt Slide as layers of POC, several earthquake chronologies were examined for comparison. Five earthquake chronologies have been compiled by Witter et al. (2003) spanning a distance of 610km along the Cascadia Subduction Zone (CSZ), from middle Washington to Northern California. These widely separated ages were obtained from buried intertidal marsh soils, representative of relative sea level rise caused by coseismic subsidence, and sandy tsunami deposits. One other chronology representing earthquakes associated with the subduction of the lithosphere was utilized based on similar

stratigraphic displacements near and around Humboldt Bay [14]. Also examined was a chronology based on turbidite sequences from the Juan de Fuca Canyon offshore northern Washington thought to record Cascadia earthquakes [27].

The POC layers in cores 01PC and 02PC have been plotted against seven independent chronologies for earthquakes (Figure 17). Each dash in the Humboldt Slide chronology represents one POC layer within a fining-upward package. The POC layers that are within a few centimeters from one another and within the same fining-upward package are assumed to represent an earthquake event with multiple transport events. Ground shaking where friable bedrock is prevalent results in landsliding and the deposition of sediment on hillslopes and valley floors. In areas where landsliding does not develop, hillslopes are predisposed to failure and will likely do so upon subsequent storms. It is multiple storm surges after an earthquake that may be responsible for closely spaced POC layers deposited offshore. The chronology of raised terraces and buried marsh soils near Humboldt Bay, indicative of coseismic uplift and subsidence, respectively, correlates fairly well with POC layers within the first three fining-upward packages observed in core 02PC at the Humboldt Slide. This raises the possibility that deposition of layers of POC at the Humboldt Slide is the consequence of earthquakes and subsequent flushing by precipitation events. All of the other chronologies compiled here (except at Sixes River) have evidence for at least three earthquakes occurring after 2000yr BP, with three of the chronologies exhibiting four earthquakes with similar ages. Therefore, it can be argued that at least three earthquakes have ruptured 850 km of the CSZ. The record at the Humboldt Slide is unlike any of the other chronologies northward, having a higher recurrence interval before ~3000yr BP.

Heaton and Hartzell (1986) suggest that plate movement at the CSZ is strongly coupled with earthquakes of M_w >8 and hypothesize that ruptures occur as either a sequence of several great earthquakes closely spaced in time or as a single giant earthquake, both of which have occurred along the Nankai trough [93]. It is recognized that coseismic slip at active continental margins occurs beneath forearc basins (e.g., Aleutian, Mexico, Peru, southern Chile, and southwest Japan subduction zones) and that these basins are typically separated by transverse gravity highs that overlie regions of lower coseismic activity, termed accommodation zones (e.g., Alaska and Japan)[93]. It has been suggested that these gravity highs are likely to be regions that accumulate interseismic strain and that typical forearc basins, such as those along the CSZ, are seismically segmented, capable of producing a variety of rupture modes and large earthquakes. The last great earthquake along the Cascadia margin occurred in AD 1700 and is represented in all of the chronologies, showing the present potential for subduction related earthquakes to rupture a substantial length of the Cascadia margin. Similarly, many of the prior earthquakes rupture the length of the margin and Clarke et al. (1992) propose the likelihood that such earthquakes have magnitudes of $M_w \geq 8.4$. The earthquakes documented in some chronologies and not others are attributed to the segmentation of the subduction zone and probably constrain the size of those earthquakes to less than M_w 8.5 [94]. Here it is suggested that the large magnitude earthquakes may play a dominant role in liberating the large amounts of biomass observed in the cores from the Humboldt slide (Figure 10).

To determine whether it is only large magnitude earthquakes that are responsible for the liberation of vast amounts of biomass, it is necessary to examine modern sediment

accumulation at the Humboldt Slide since no earthquake of considerable magnitude has ruptured for over 300 years. Sedimentation near the toe of the Humboldt slide is anomalously high [1], however, seismic reflection data imaging the main body of the slide offers insight into a changing sedimentation regime (Figure 18). Gardner et al. (1999) identify what they term a transparent drape; a thin veneer of sediment that does not conform to the sedimentation regime of the underlying sediment. This drape does not show the typical characteristics of an upslope-migrating sediment wave. Instead, it is more akin to the deposition of hemipelagic sediment that uniformly covers the seafloor. This suggests that there has been no recent hyperpycnal flow, potentially triggered by an earthquake, capable of transporting large amounts of sediment and biomass to the continental slope. It may be that hyperpycnal flows off the shelf are required to form sediment waves. If correct, then sedimentation and carbon burial at the Humboldt slide may be largely controlled by coseismic landsliding onshore, followed by precipitation-controlled deposition offshore.

4.4.2 Climate

Ocean-atmosphere interaction is a key aspect in understanding the earth's climate and, in the past few decades, scientists have increased their efforts in understanding this interface. Extensive analyses of Pacific Ocean climate records, including sea surface temperature (SST), sea level pressure (SLP), and surface winds, have revealed significant interdecadal variability in the climate regime of this ocean basin, which has been termed Pacific Decadal Oscillation (PDO). A major signature of PDO is anomalously low SSTs and SLPs in the central North Pacific [30, 51, 52]. This intensification of the Aleutian

Low pressure system results in strong cyclonic flow in the North Pacific, resulting in enhanced westerly and southerly winds that pull warm air and water from the equatorial regions toward the west coast of North America [30, 52]. The enhanced Aleutian Low and narrow belt of warm SST along the west coast of North America is characteristic of the positive phase of PDO; predominantly, the California Current travels south along the coast, bringing cold waters from the polar regions. The Oyashio Current is also affected, as its cold waters migrate further south along the Japanese coast during this positive phase [62]. The negative phase of PDO is simply the opposite of the aforementioned characteristics: a relaxing of the Aleutian Low, colder waters along the west coast of North America, and more easterly wind directions. The empirical record of PDO is rather short (a little more than a century of recorded SST and SLP) and is supported by an air-temperature reconstruction based on chronologies of tree-ring widths in North America [62]. The temporal spectrum of PDO varies depending on the analysis technique applied, however, several studies show consistent periodicities. Minobe (1997, 1999) found PDO periodicities to be in the 15–to–25 year and 50–to–70 year ranges. Chao et al. (2000) and Tourre et al. (2001) also found similar periodicities of 12–to–25 and near 70 years. There exists some agreement that PDO polarity reversals have occurred in 1890 [62], 1925, 1947, 1977 [30, 52, 62] and, arguably, 1998 when the PDO index, based on monthly SST anomalies in the North Pacific, dropped to negative through the present day, with a positive excursion from 2002 to 2006. It may be that the Pacific has entered into a negative phase of PDO, which will cause detrimental effects to those regions in North America experiencing drought conditions that will presumably continue for many years.

The warm SSTs along the coast of California, associated with the positive phase of PDO, create an environment that is more favorable for evaporation. This produces a greater likelihood that atmospheric convective processes will dominate and occur for longer periods of time, generating larger storms that naturally result in greater amounts of rainfall. An increase in precipitation will not only increase river discharge from the catchment, it will also increase the amount of sediment that is eroded and entrained by the fluvial system. More sediment being delivered to river channels will increase the probability of hyperpycnal flows to develop. Larger storm waves associated with intense storms and enhanced hyperpycnal flows of greater sediment content both contribute to sediment traveling farther offshore and being deposited at greater water depths. During the negative phase of PDO, storms are of lesser magnitude and sediment deposits at similar water depths offshore are expected to be finer grained. This scenario is consistent with the sedimentation that is observed at the Humboldt Slide. The base of the fining-upward packages may document the onset of the positive phase of PDO when storms are more intense. The transition from coarse to fine sediment within each fining-upward package represents the regime shift from a positive to a negative PDO phase or of some similar climatic oscillation that has been occurring for the past few millennia.

Using the accumulation rates based on radiocarbon dating, the age of each fining-upward package was calculated. Before ~2600yr BP, the majority of the packages span less than 120yr and a 5-period moving average reveals a peak at 90-100yr. This periodicity is somewhat similar to that of PDO of 100-140yr to experience both a positive and a negative phase (see above). After ~2600yr BP, packages are deposited much less frequently, spanning no less than ~200yr. The changes in the climate regime that these

packages record are more regularly documented before ~2600yr BP. After this time, the signal is not as well developed, suggesting that the climate forcing became weaker. These data show, however, that for the past several thousand years, a PDO-like climate shift occurred in the Pacific Ocean that became systematically weaker in the past two thousand years.

This "Discussion" chapter, in part, is currently being prepared for submission for publication of the material. McCullough, Justin S.; Driscoll, Neal W. The thesis author was the primary investigator and author of this material.

Conclusions

5. Conclusions

On the basis of core observations, it is postulated that a significant quantity of biomass carbon is eroded from humid active mountain belts as a consequence of earthquake and precipitation-induced landslides and storm-dominated fluvial discharge to the ocean. We purport that there exists a tectonic control on sedimentation and, ultimately, on carbon sequestration in the Eel Margin. The key to validating this assertion lies in the marine record along active margins. Determining the amount of biomass-derived carbon preserved in offshore depocenters is the critical first step toward understanding the export of biomass in detritus from coastal mountain catchments.

To summarize, humid active margins are the settings of considerable biomass carbon erosion, transport, and sequestration, drawing carbon directly from the biosphere into the lithosphere. These carbon sinks might be important in the global carbon cycle on geologic time scales of 10,000 years and longer and may serve as a proxy for determining the timing of seismic events.

This "Conclusions" chapter, in part, is currently being prepared for submission for publication of the material. McCullough, Justin S.; Driscoll, Neal W. The thesis author was the primary investigator and author of this material.

Appendix

Appendix

Appendix includes all data associated with the analyzed sections of cores 01PC, 02PC, and 07PC. Included for each section, from left to right: magnetic susceptibility data from Schwehr et al. (2007) in red; a photograph of the core; dates of POC layers and the bases of fining-upward packages using the two methods described in the methodology; a depiction of the core, with the legend (below) defining coarseness and fineness based on visual estimations; the coarse-grained weight percentage in blue; and the fine-grained volumetric percentages with clay in pink and silt in green. The coarse grain size data for core 02PC is thought to be biased due to an instrumental defect of the sieve used for those particular samples because all samples have a significantly smaller percentage than samples from the other cores. The relative coarseness of each sample throughout the core, however, is accurate for the same sieve was used for each sample. The dashed lines across the graphs represent those bases that have been reinterpreted (see text).

This appendix, in part, is currently being prepared for submission for publication of the material. McCullough, Justin S.; Driscoll, Neal W. The thesis author was the primary investigator and author of this material.

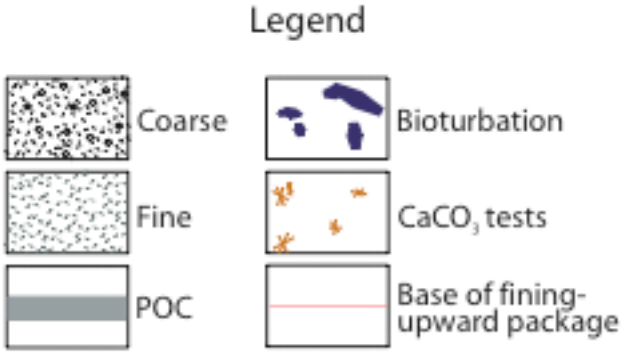

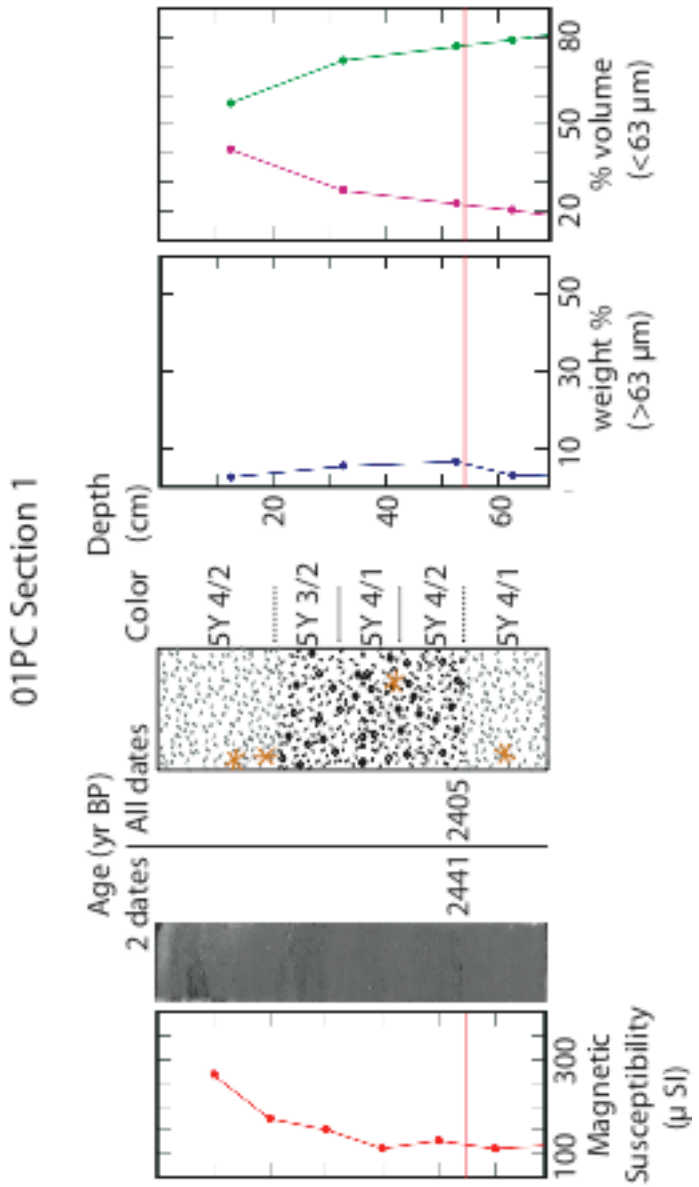
01PC Section 1
Age (yr BP)
2 dates
All dates
2441
2405
Color
5Y 4/2
5Y 3/2
5Y 4/1
5Y 4/2
5Y 4/1
Depth
(cm)
20
40
60
10
30
50
weight %
(>63 µm)
20
50
80
% volume
(<63 µm)
100
300
Magnetic
Susceptibility
(µ SI)

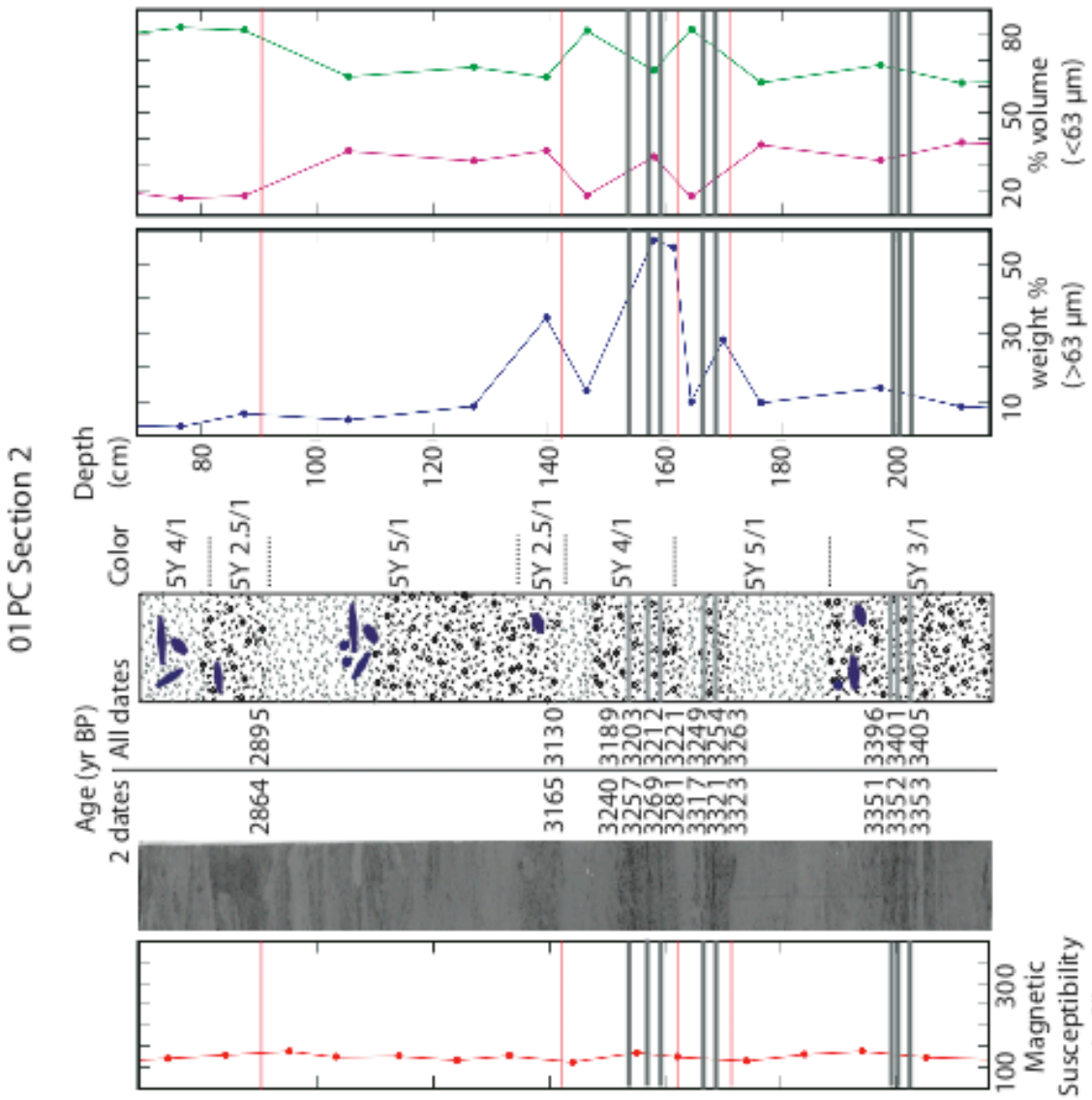
01PC Section 2
Age (yr BP)
2 dates
All dates
Color
Depth (cm)
2864
2895
3165
3130
3240
3257
3269
3281
3317
3321
3323
3189
3203
3212
3221
3249
3254
3263
3351
3352
3353
3396
3401
3405
5Y 4/1
5Y 2.5/1
5Y 5/1
5Y 2.5/1
5Y 4/1
5Y 5/1
5Y 3/1
80
100
120
140
160
180
200
100
300
Magnetic Susceptibility (μ SI)
10
30
50
weight % (>63 μm)
20
50
80
% volume (<63 μm)

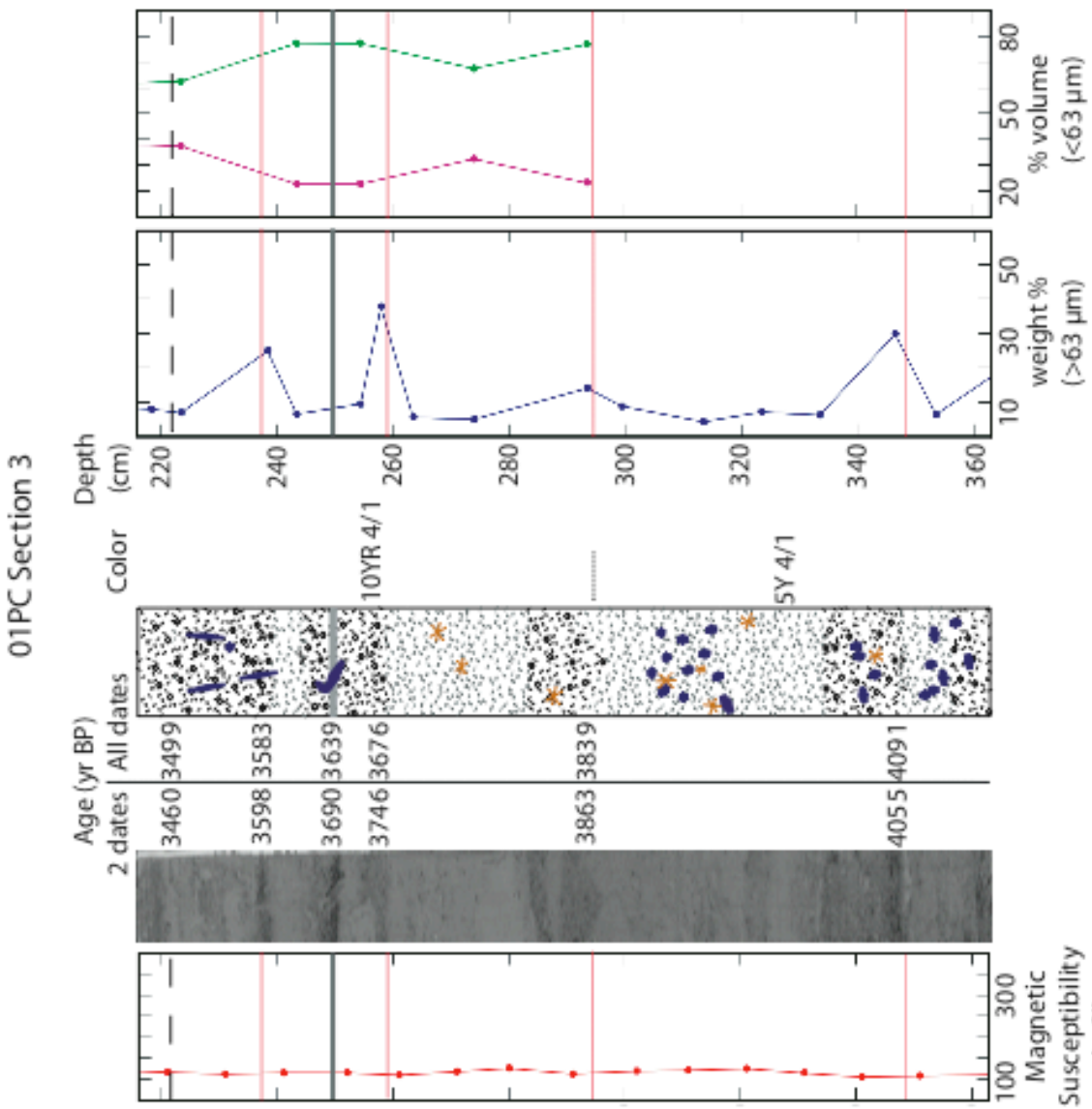
01PC Section 3
Age (yr BP)
2 dates
All dates
3460
3499
3598
3583
3690
3639
3746
3676
3863
3839
4055
4091
Color
10YR 4/1
5Y 4/1
Depth (cm)
220
240
260
280
300
320
340
360
10
30
50
weight %
(>63 µm)
20
50
80
% volume
(<63 µm)
100
300
Magnetic
Susceptibility
(µ SI)

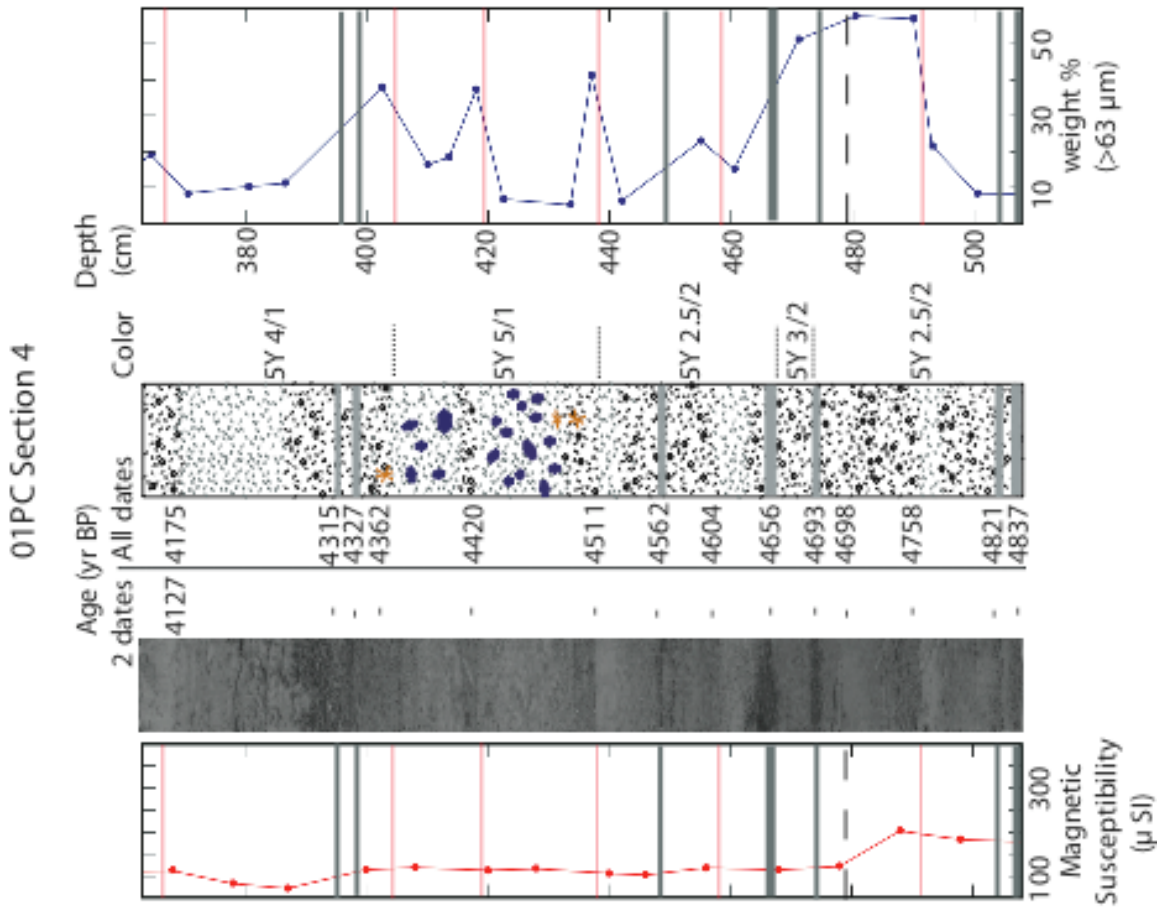
01PC Section 4
Age (yr BP)
2 dates
All dates
Color
Depth (cm)
4127
4175
4315
4327
4362
4420
4511
4562
4604
4656
4693
4698
4758
4821
4837
5Y 4/1
5Y 5/1
5Y 2.5/2
5Y 3/2
5Y 2.5/2
380
400
420
440
460
480
500
10
30
50
weight %
(>63 µm)
100
300
Magnetic
Susceptibility
(µ SI)

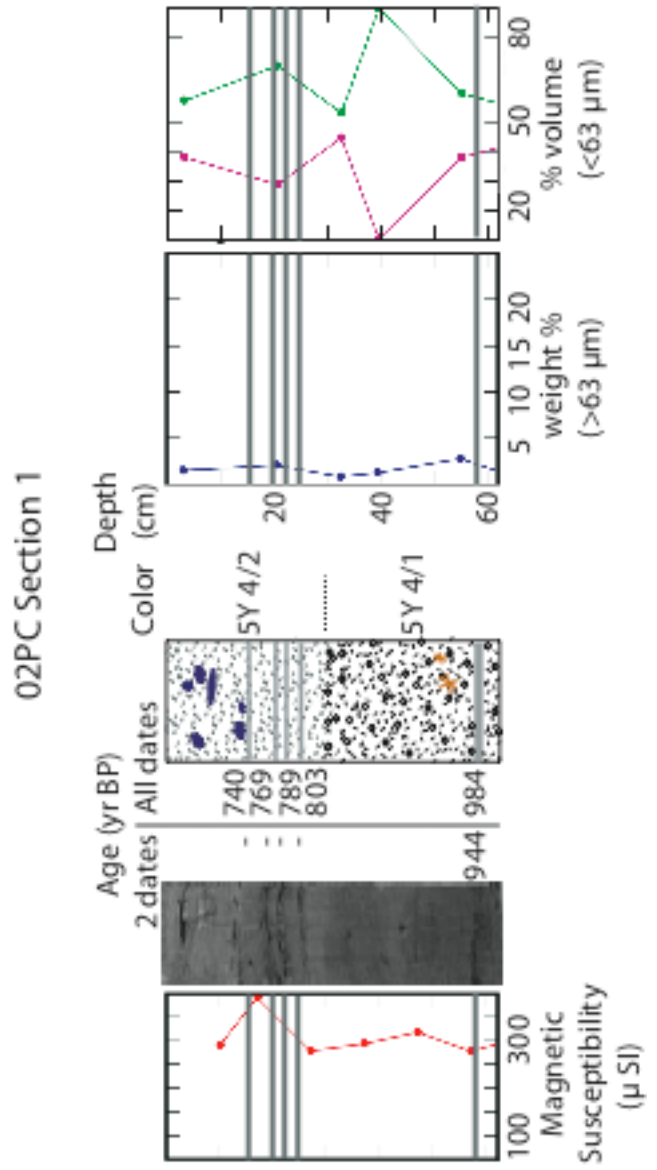
02PC Section 1
Age (yr BP)
2 dates
All dates
740
769
789
803
944
984
Color
5Y 4/2
5Y 4/1
Depth
(cm)
20
40
60
5 10 15 20
weight %
(>63 µm)
20 50 80
% volume
(<63 µm)
100 300
Magnetic
Susceptibility
(µ SI)

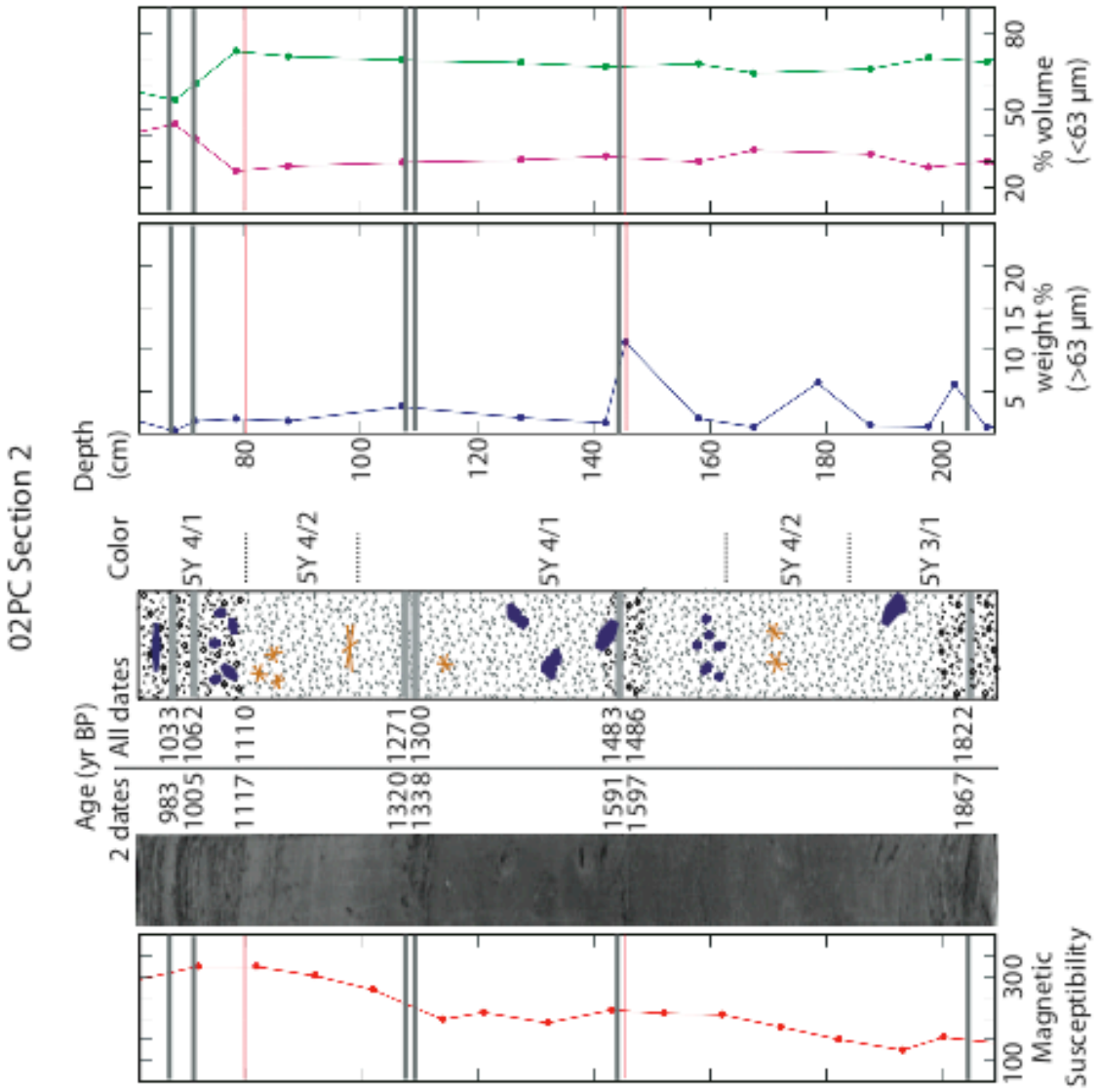
02PC Section 2
Age (yr BP)
2 dates
All dates
983
1005
1033
1062
1117
1110
1320
1338
1271
1300
1591
1597
1483
1486
1867
1822
Color
5Y 4/1
5Y 4/2
5Y 4/1
5Y 4/2
5Y 3/1
Depth
(cm)
80
100
120
140
160
180
200
5 10 15 20
weight %
(>63 µm)
20 50 80
% volume
(<63 µm)
100 300
Magnetic
Susceptibility
(µ SI)

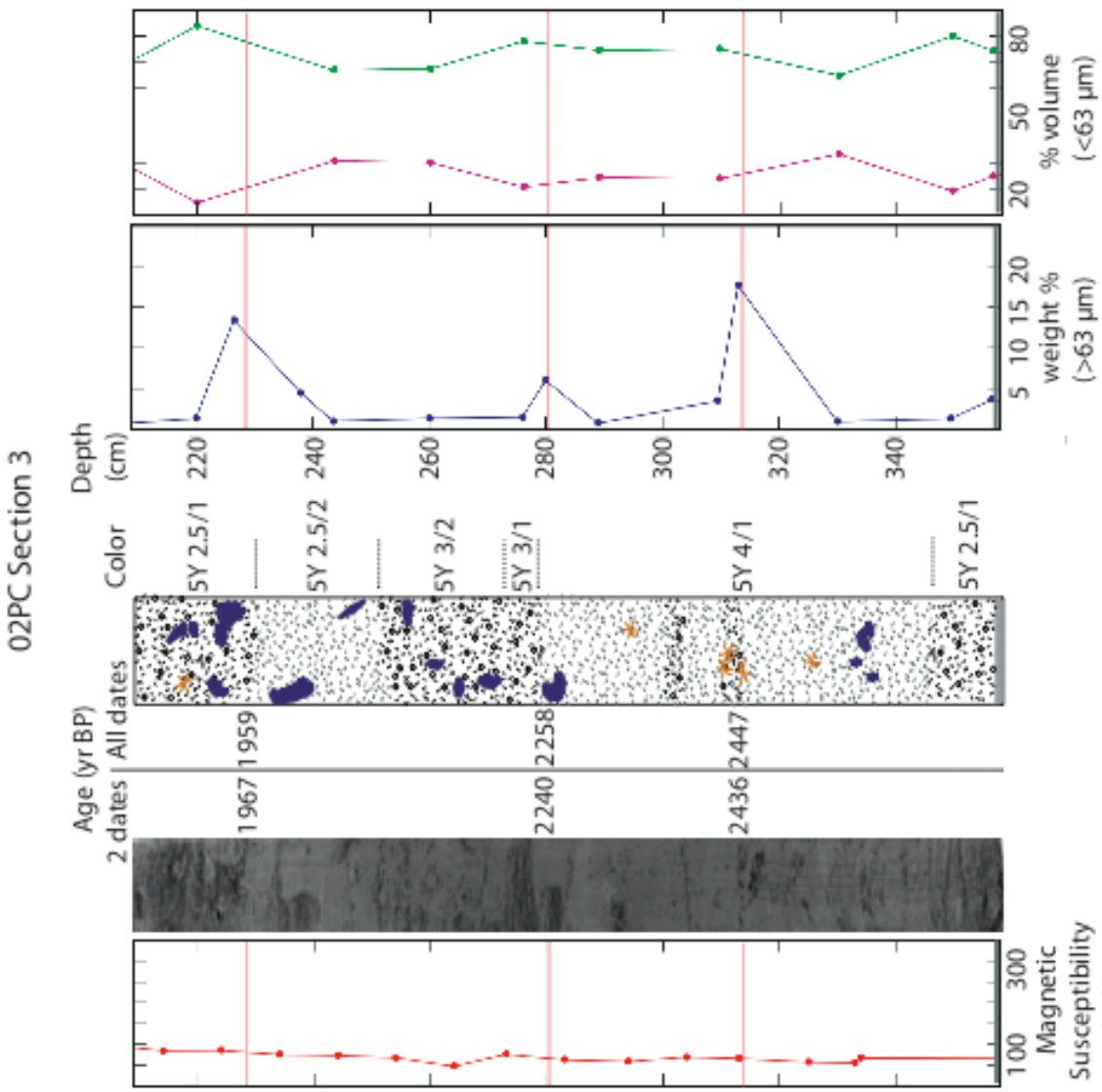
02PC Section 3
Age (yr BP)
2 dates
All dates
1967
1959
2240
2258
2436
2447
Color
5Y 2.5/1
5Y 2.5/2
5Y 3/2
5Y 3/1
5Y 4/1
5Y 2.5/1
Depth (cm)
220
240
260
280
300
320
340
Magnetic Susceptibility (μ SI)
100
300
weight % (>63 μm)
5
10
15
20
% volume (<63 μm)
20
50
80

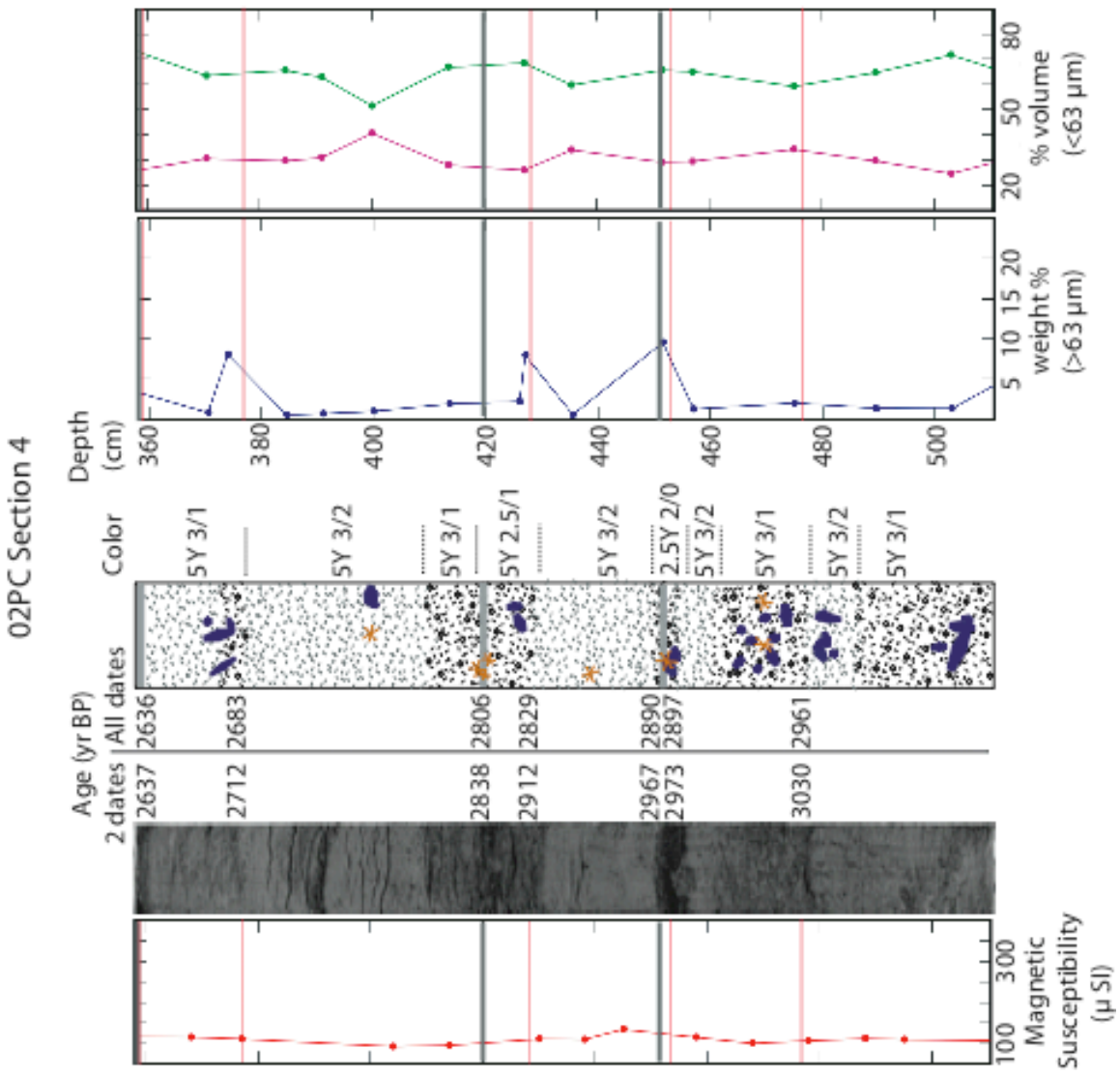
02PC Section 4
Age (yr BP)
2 dates
All dates
Color
Depth (cm)
Magnetic Susceptibility (μ SI)
% volume (<63 μm)
weight % (>63 μm)
2637
2712
2838
2912
2967
2973
3030
2636
2683
2806
2829
2890
2897
2961
5Y 3/1
5Y 3/2
5Y 3/1
5Y 2.5/1
5Y 3/2
2.5Y 2/0
5Y 3/2
5Y 3/1
5Y 3/2
5Y 3/1
360
380
400
420
440
460
480
500
100
300
20
50
80
5
10
15
20

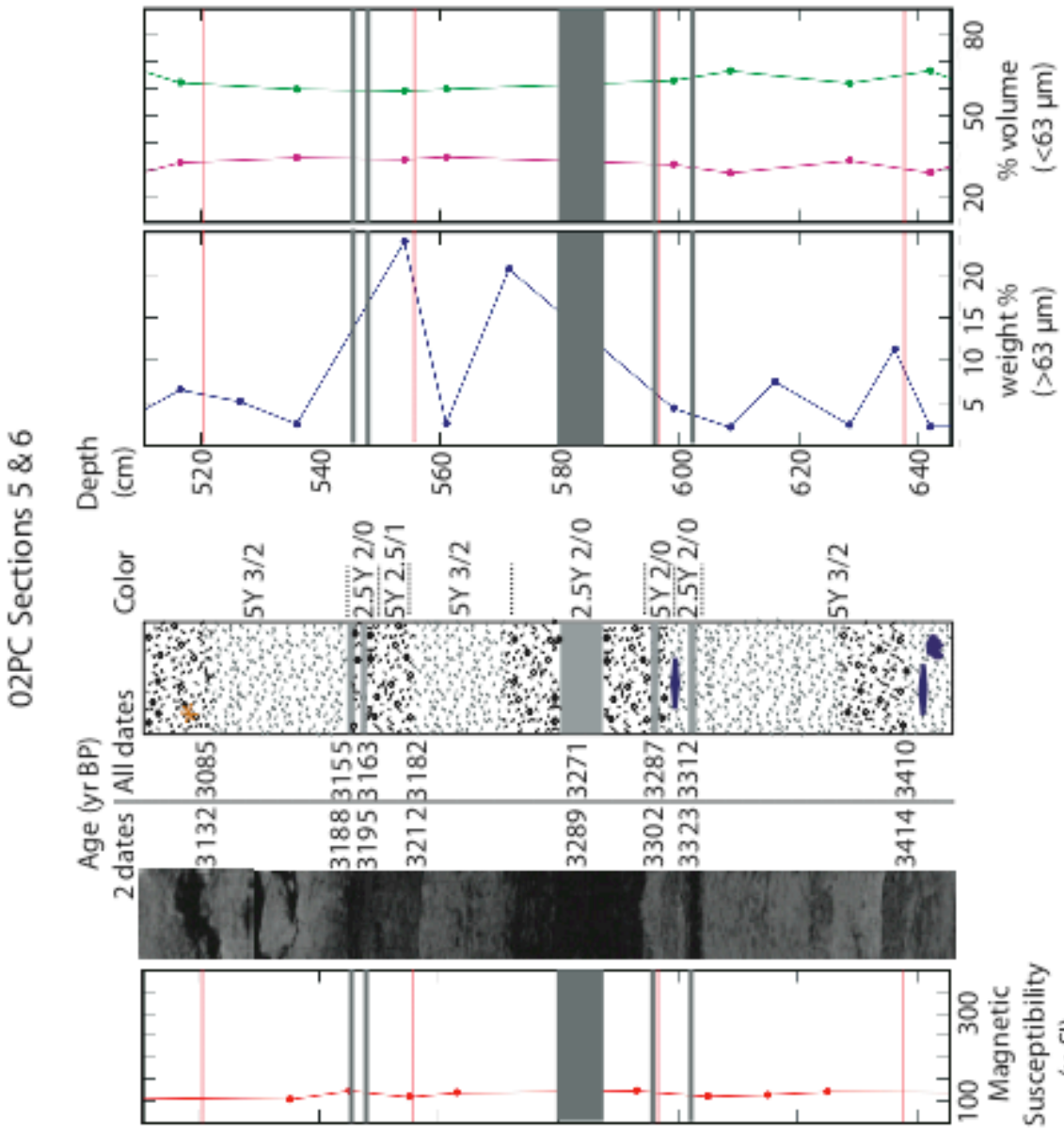
02PC Sections 5 & 6
Age (yr BP)
2 dates
All dates
3132
3085
3188
3155
3195
3163
3212
3182
3289
3271
3302
3287
3323
3312
3414
3410
Color
5Y 3/2
2.5Y 2/0
5Y 2.5/1
5Y 3/2
2.5Y 2/0
5Y 2/0
2.5Y 2/0
5Y 3/2
Depth
(cm)
520
540
560
580
600
620
640
100
300
Magnetic
Susceptibility
(μ SI)
5
10
15
20
weight %
(>63 μm)
20
50
80
% volume
(<63 μm)

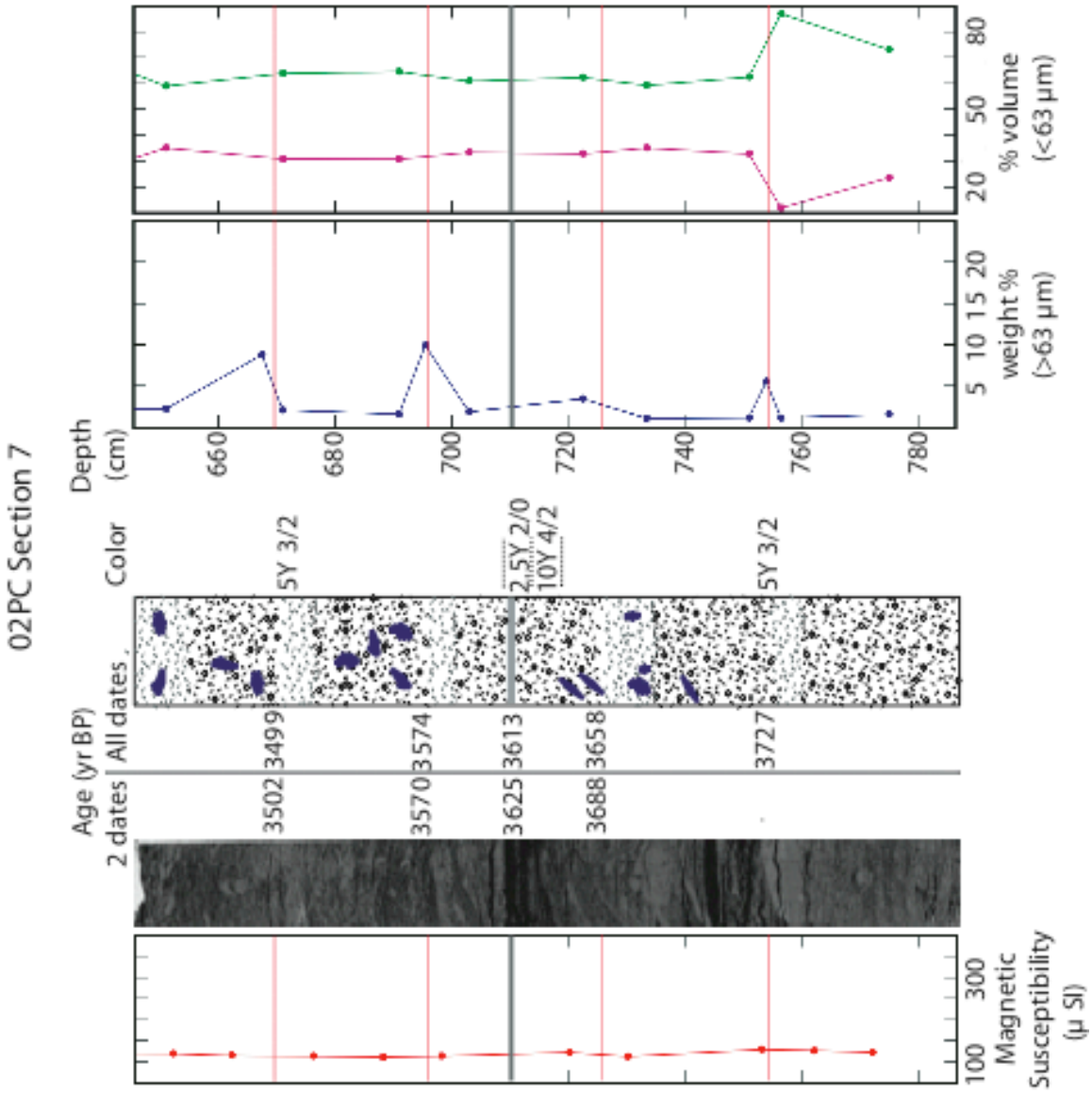
02PC Section 7
Age (yr BP)
2 dates
All dates
Color
Depth
(cm)
3502
3499
3570
3574
3625
3613
3688
3658
3727
5Y 3/2
2.5Y 2/0
10Y 4/2
5Y 3/2
660
680
700
720
740
760
780
5 10 15 20
weight %
(>63 µm)
20 50 80
% volume
(<63 µm)
100 300
Magnetic
Susceptibility
(µ SI)

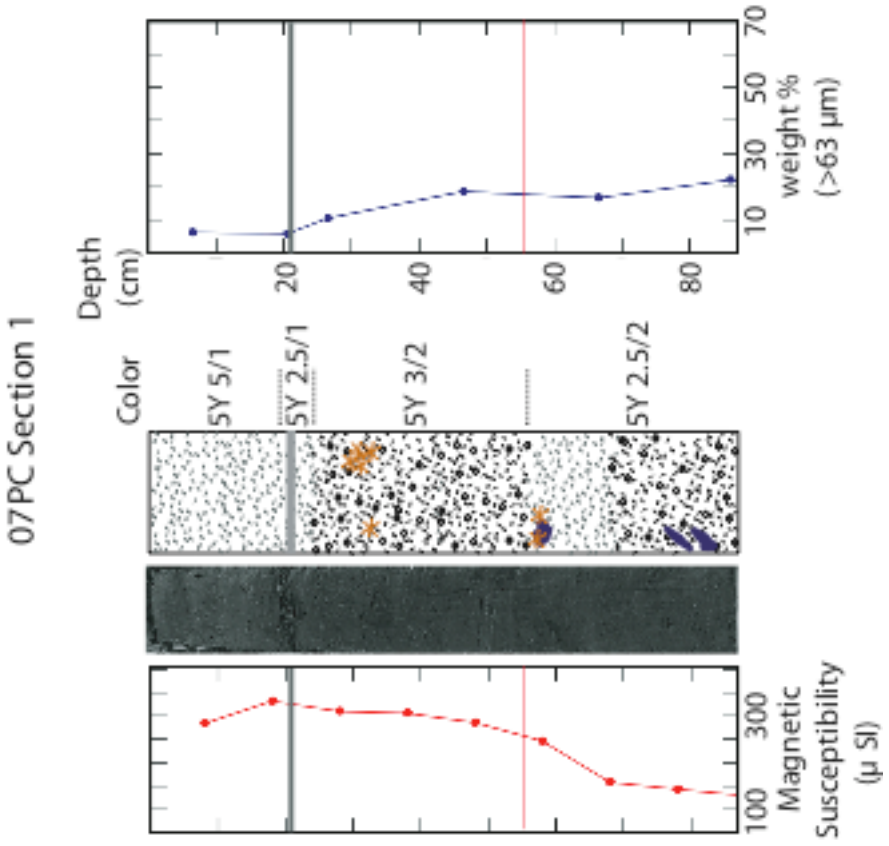
07PC Section 1
Depth (cm)
20
40
60
80
Color
5Y 5/1
5Y 2.5/1
5Y 3/2
5Y 2.5/2
10
30
50
70
weight %
(>63 µm)
100
300
Magnetic Susceptibility (µ SI)

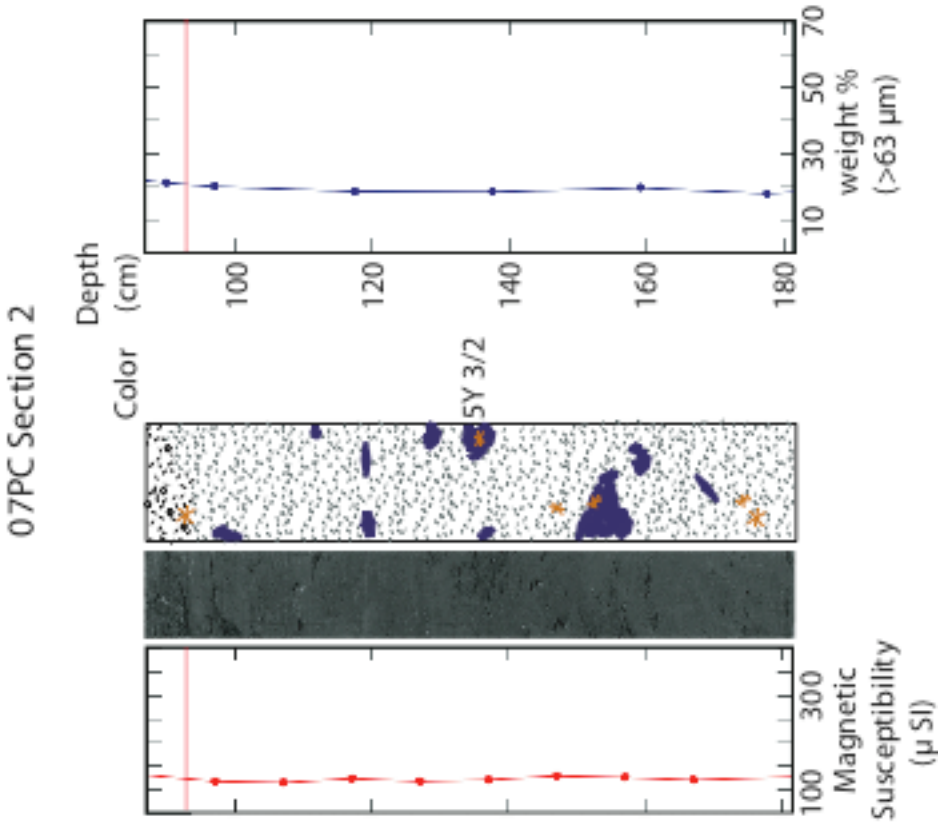
07PC Section 2
Depth (cm)
100
120
140
160
180
Color
5Y 3/2
10
30
50
70
weight %
(>63 µm)
100
300
Magnetic Susceptibility (µ SI)

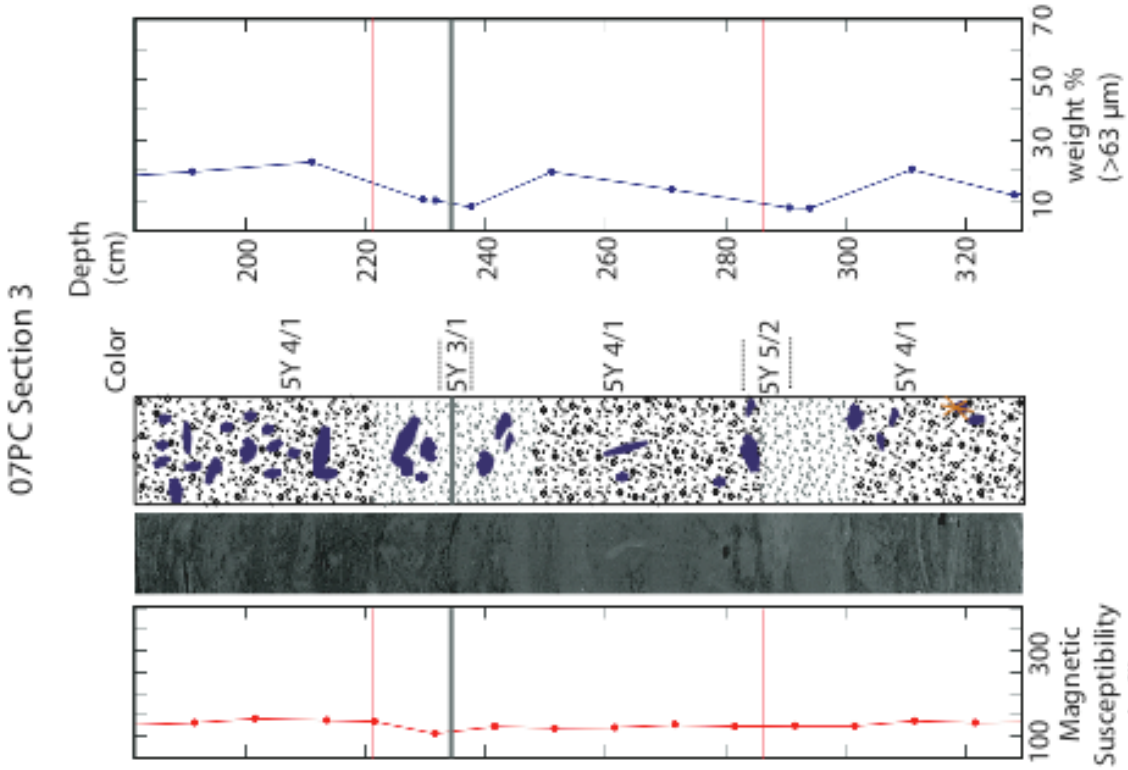
07PC Section 3
Depth (cm)
200
220
240
260
280
300
320
Color
5Y 4/1
5Y 3/1
5Y 4/1
5Y 5/2
5Y 4/1
10 30 50 70
weight %
(>63 µm)
100 300
Magnetic Susceptibility (µ SI)

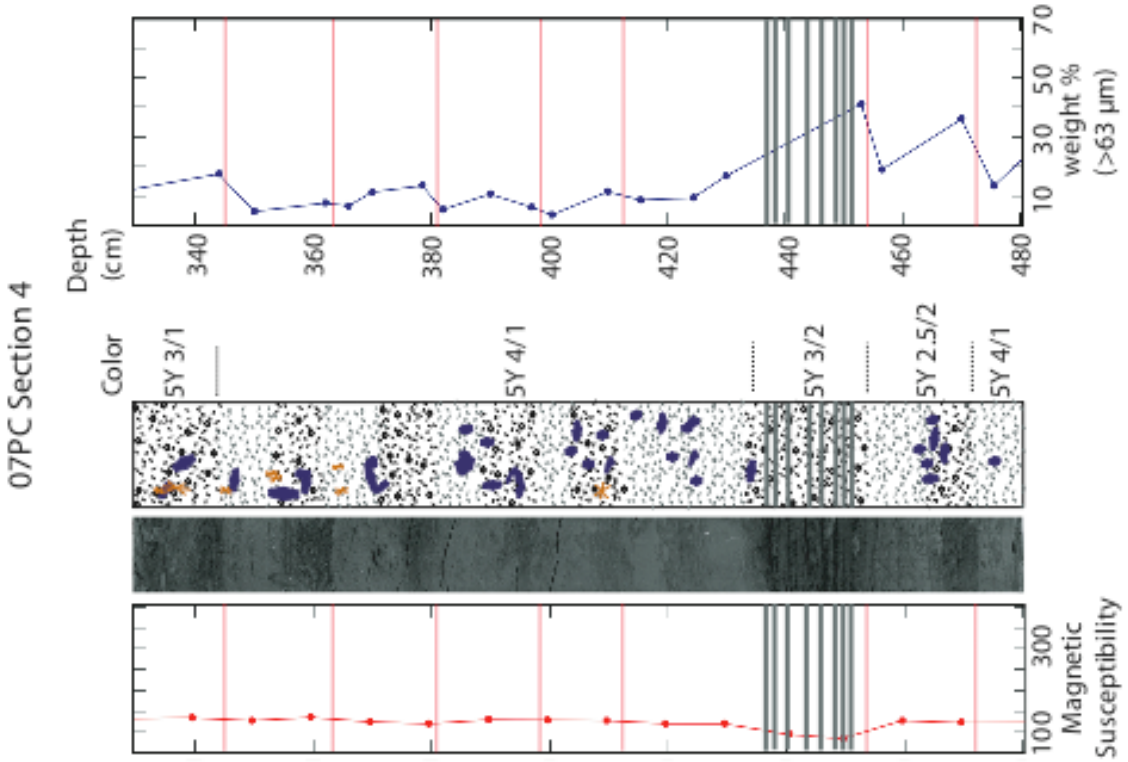
07PC Section 4
Depth (cm)
340
360
380
400
420
440
460
480
Color
5Y 3/1
5Y 4/1
5Y 3/2
5Y 2.5/2
5Y 4/1
10
30
50
70
weight %
(>63 µm)
100
300
Magnetic Susceptibility (µ SI)

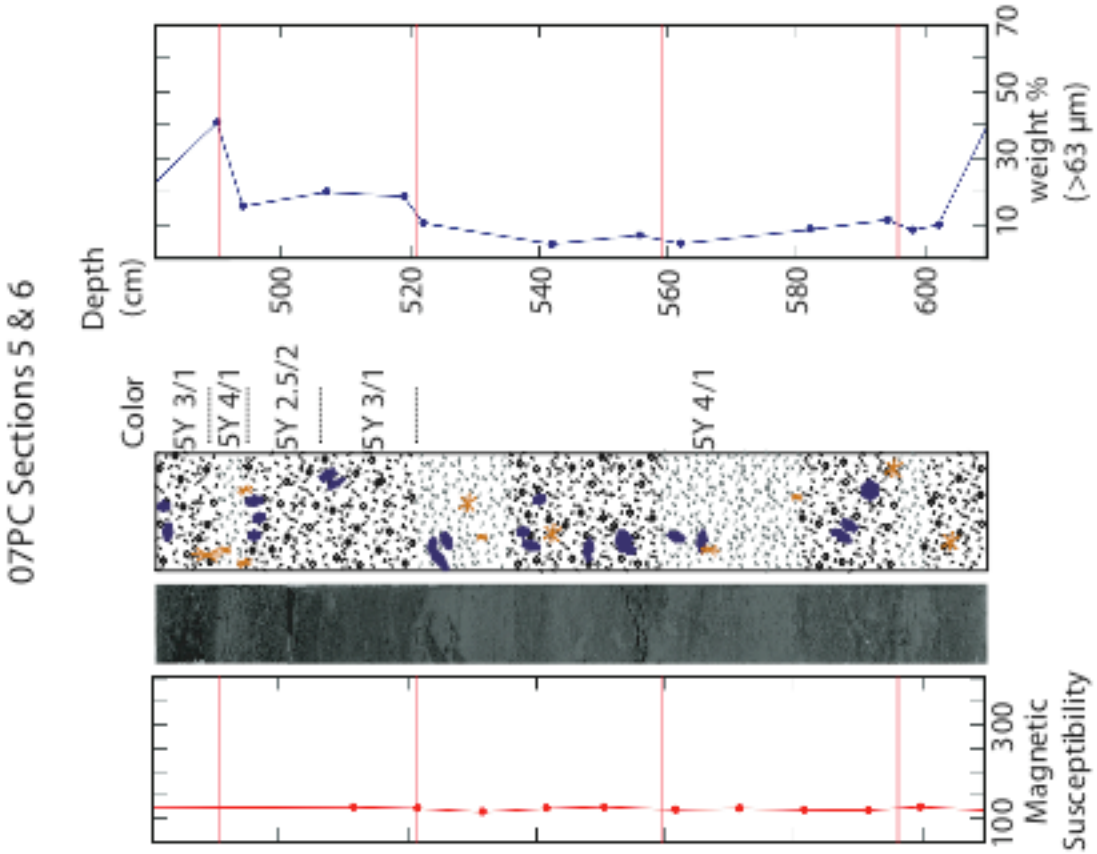
07PC Sections 5 & 6
Depth (cm)
Color
5Y 3/1
5Y 4/1
5Y 2.5/2
5Y 3/1
5Y 4/1
500
520
540
560
580
600
10 30 50 70
weight %
(>63 µm)
100 300
Magnetic Susceptibility (µ SI)

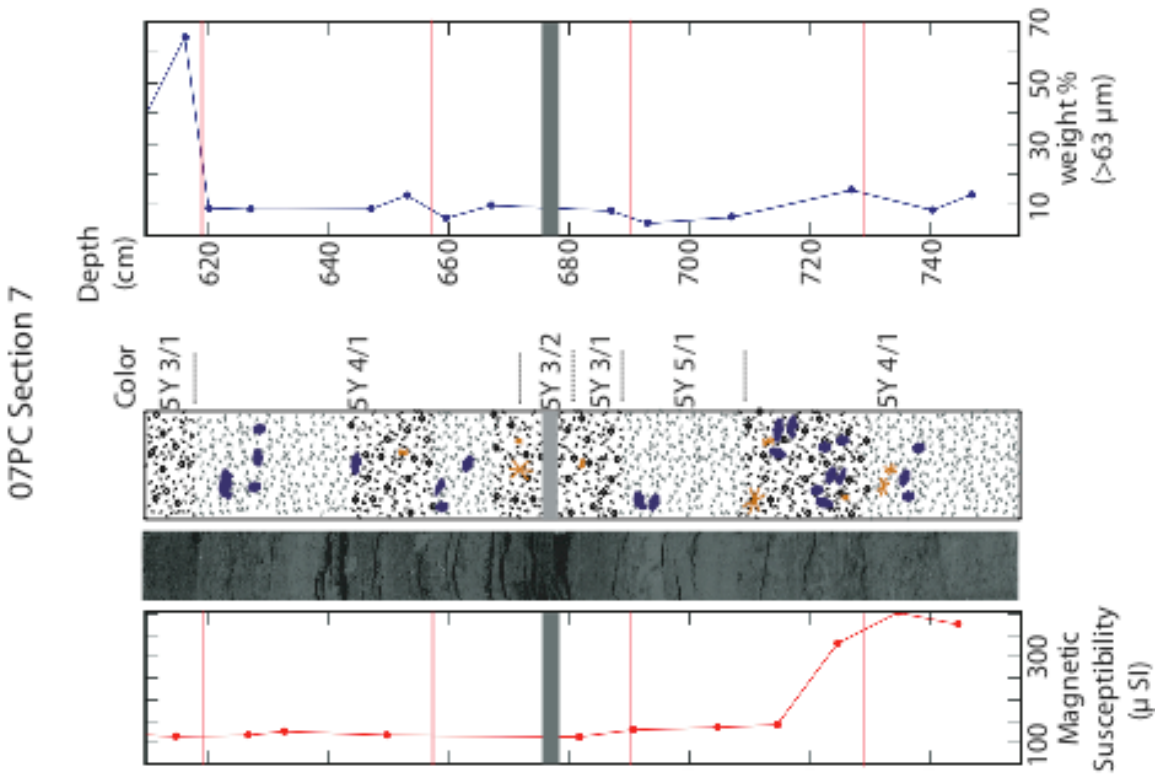
07PC Section 7
Depth (cm)
620
640
660
680
700
720
740
Color
5Y 3/1
5Y 4/1
5Y 3/2
5Y 3/1
5Y 5/1
5Y 4/1
10 30 50 70
weight % (>63 µm)
100 300
Magnetic Susceptibility (µ SI)

References

References

[1] Alexander, C.R. and Simoneau, A.M., 1999. Spatial variability in sedimentary processes on the Eel continental slope. Marine Geology, 154(1-4): 243-254.

[2] Allen, R.B., Bellingham, P.J. and Wiser, S.K., 1999. Immediate damage by an earthquake to a temperate montane forest. Ecology, 80(2): 708-714.

[3] Aller, R.C., Blair, N.E., Xia, Q. and Rude, P.D., 1996. Remineralization rates, recycling, and storage of carbon in Amazon shelf sediments. Continental Shelf Research, 16(5-6): 753-786.

[4] Benda, L. and Dunne, T., 1997a. Stochastic forcing of sediment supply to channel networks from landsliding and debris flow. Water Resources Research, 33(12): 2849-2863.

[5] Benda, L. and Dunne, T., 1997b. Stochastic forcing of sediment routing and storage in channel networks. Water Resources Research, 33(12): 2865-2880.

[6] Benda, L., Miller, D., Bigelow, P. and Andras, K., 2003. Effects of post-wildfire erosion on channel environments, Boise River, Idaho, Forest Ecology and Management 178, 105-119.

[7] Brown, S. and Lugo, A.E., 1984. Biomass of tropical forests: A new estimate based on forest volumes. Science, 223(4642): 1290-1293.

[8] Brown, W.M., III and Ritter, J.R., 1971. Sediment transport and turbidity in the Eel River basin, California. U.S. Geol. Survey Water Supply Paper 1986, 70 p.

[9] Cannon, S.H., Bigio, E.R. and Mine, E., 2001a. A process for fire-related debris flow initiation, Cerro Grande fire, New Mexico. Hydrological Processes, 15(15): 3011-3023.

[10] Cannon, S.H. and Gartner, J.E., 2005. Wildfire-related debris flow from a hazards perspective. In: M. Jakob and O. Hungr (Eds), Debris-flow hazards and related phenomena. Springer Praxis Books, Berlin, 363-385.

[11] Cannon, S.H., Kirkham, R.M. and Parise, M., 2001b. Wildfire-related debris-flow initiation processes, Storm King Mountain, Colorado. Geomorphology, 39(3-4): 171-188.

[12] Chao, Y., Ghil, M. and McWilliams, J.C., 2000. Pacific interdecadal variability in this century's sea surface temperatures. Geophysical Research Letters, 27(15): 2261-2264.

[13] Chen, R.F., Chang, K.-J., Angelier, J., Chan, Y.-C., Deffontaines, B., Lee, C.-T., Lin, M.-L., 2006. Topographical changes revealed by high-resolution airborne LiDAR data: The 1999 Tsaoling landslide induced by the Chi-Chi earthquake, Engineering Geology 88, 160-172.

[14] Clarke, S.H. and Carver, G.A., 1992. Late Holocene tectonics and paleoseismicity, southern Cascadia Subduction Zone. Science, 255(5041): 188-192.

[15] Cochrane, M.A. Alencar, A., Schulze, M. D., Souza, C. M. Jr., Nepstad, D. C., Lefebvre, P., Davidson, E. A., 1999. Positive feedbacks in the fire dynamic of closed canopy tropical forests. Science, 284(5421): 1832-1835.

[16] Costa, J.E. and Schuster, R.L., 1988. The formation and failure of natural dams. Geological Society of America Bulletin, 100(7): 1054-1068.

[17] Crouch, J.K. and Bachman, S.B., 1987. Exploration potential, offshore Point Arena and Eel River basins. In: H. Schymiczek and R. Suchsland (Eds.), Tectonics, sedimentation and evolution of the Eel River and associated coastal basins of northern California. San Joaquin Geologic Society, 37: 99–111

[18] Dadson, S.J., Hovius, N., Chen, H., Dade, W.B., Lin, J.-C., Hsu, M.-L., Lin, C.-W., Horng, M.-J., Chen, T.-C., Milliman, J., Stark, C.P., 2004. Earthquake-triggered increase in sediment delivery from an active mountain belt. Geology, 32(8): 733-736.

[19] Driscoll, N., Orange, D., Yun, J., Fonseca, L., Mayer, L., 1998. High resolution side-scan and seismic images of landslides on the Northern California continental shelf. In: Eos, Transactions of the American Geophysical Union, 79 (45, Suppl.). American Geophysical Union, Washington D.C., F811.

[20] Eglinton, T.I., Benitez-Neelson, B. C., Pearson, A., McNichol, A. P., Bauer, J. E., Druffel, E. R. M., 1997. Variability in radiocarbon ages of individual organic compounds from marine sediments. Science, 277(5327): 796-799.

[21] Field, M.E., Gardner, J.V. and Prior, D.B., 1999. Geometry and significance of stacked gullies on the northern California slope. Marine Geology, 154(1-4): 271-286.

[22] Field, M.E. and Kvenvolden, K.A., 1987. Preliminary report on gaseous hydrocarbons in sediment and seeps, offshore Eel River basin, California. In: H. Schymiczek and R. Suchsland (Eds.), Tectonics, sedimentation and evolution of the Eel River and associated coastal basins of northern California. San Joaquin Geologic Society, 37: 55–60.

[23] Flood, R.D., 1988. A lee wave model for deep-sea mudwave activity. Deep-Sea Research - Oceanographic Research Papers, 35(6): 973-983.

[24] Gardner, J.V., Prior, D.B. and Field, M.E., 1999. Humboldt Slide - a large shear-dominated retrogressive slope failure. Marine Geology, 154(1-4): 323-338.

[25] Garwood, N.C., Janos, D.P. and Brokaw, N., 1979. Earthquake-caused landslides: A major disturbance to tropical forests. Science, 205(4410): 997-999.

[26] Geyer, W.R., 1993. The importance of suppression of turbulence by stratification on the estuarine turbidity maximum. Estuaries, 16(1): 113-125.

[27] Goldfinger, C., Nelson, C.H., Johnson, J.E. and Shipboard Scientific Party, 2003. Holocene earthquake records from the Cascadia Subduction Zone and northern San Andreas Fault based on precise dating of offshore turbidites. Annual Review of Earth and Planetary Sciences, 31: 555-577.

[28] Guariguata, M.R., 1990. Landslide disturbance and forest regeneration in the Upper Luquillo Mountains of Puerto Rico. Journal of Ecology, 78(3): 814-832.

[29] Hadley, J.B., 1964. Landslides and related phenomena accompanying the Hebgen Lake earthquake of August 17, 1959. U. S. Geological Survey Professional Paper 435: 107-138.

[30] Hare, S.R., Mantua, N.J. and Francis, R.C., 1999. Inverse production regimes: Alaska and West Coast Pacific salmon. Fisheries, 24(1): 6-14.

[31] Hayhurst, C.A., 2006. A case study of shallow landslide occurrence and magnitude-frequency due to rainfall events after earthquakes in northwestern California. MS Thesis, Humboldt State University, 60p.

[32] Heaton, T.H. and Hartzell, S.H., 1986. Source characteristics of hypothetical subduction earthquakes in the northwestern United States. Bulletin of the Seismological Society of America, 76(3): 675-708.

[33] Hedges, J.I. and Keil, R.G., 1995. Sedimentary organic matter preservation: An assessment and speculative synthesis. Marine Chemistry, 49(2-3): 81-115.

[34] Heede, B.H., Harvey, M.D. and Laird, J.R., 1988. Sediment delivery linkages in a chaparral watershed following a wildfire. Environmental Management, 12(3): 349-358.

[35] Hovius, N., Stark, C.P. and Allen, P.A., 1997. Sediment flux from a mountain belt derived by landslide mapping. Geology, 25(3): 231-234.

[36] Hovius, N., Stark, C.P., Chu, H.T. and Lin, J.C., 2000. Supply and removal of sediment in a landslide-dominated mountain belt: Central Range, Taiwan. Journal of Geology, 108(1): 73-89.

[37] Hughen, K.A. , Baillie, M. G. L., Bard, E., Beck, J. W., Bertrand, C. J. H., Blackwell, P. G., Buck, C. E., Burr, G.S., Cutler, K. B., Damon, P.E., Edwards, R. L., Fairbanks, R. G., Friedrich, M., Guilderson, T. P., Kromer, B., McCormac, G., Manning, S., Ramsey, C. B., Reimer, P., Reimer, R. W., Remmele, S., Southon, J. R., Stuiver, M., Talamo, S., Taylor, F. W., van der Plicht, J., Weyhenmeyer, C. E., 2004. Marine04 marine radiocarbon age calibration, 0-26 cal kyr BP. Radiocarbon, 46(3): 1059-1086.

[38] Ice, G., 2003. Effects of Water on Soils and Watershed Processes, in: Conference on Post-fire Restoration & Salvage Harvesting: Applying Our Knowledge and Experience, sponsored by Central Oregon Society of American Foresters, Deschutes National Forest, Oregon State University Extension Forestry Program, and Oregon Department of Forestry, Bend, Oregon. October 21-23.

[39] Inbar, M., Tamir, M. and Wittenberg, L., 1998. Runoff and erosion processes after a forest fire in Mount Carmel, a Mediterranean area. Geomorphology, 24(1): 17-33.

[40] Kao, S.J. and Liu, K.K., 1996. Particulate organic carbon export from a subtropical mountainous river (Lanyang Hsi) in Taiwan. Limnology and Oceanography, 41(8): 1749-1757.

[41] Keefer, D.K., 1994. The importance of earthquake-induced landslides to long-term slope erosion and slope-failure hazards in seismically active regions. Geomorphology, 10: 265–284.

[42] Keil, R.G., Mayer, L.M., Quay, P.D., Richey, J.E. and Hedges, J.I., 1997. Loss of organic matter from riverine particles in deltas. Geochimica Et Cosmochimica Acta, 61(7): 1507-1511.

[43] Keil, R.G., Tsamakis, E., Fuh, C.B., Giddings, J.C. and Hedges, J.I., 1994. Mineralogical and textural controls on the organic composition of coastal marine sediments: Hydrodynamic separation using SPLITT-fractionation. Geochimica Et Cosmochimica Acta, 58(2): 879-893.

[44] Kelsey, H.M., Witter, R.C. and Hemphill-Haley, E., 2002. Plate-boundary earthquakes and tsunamis of the past 5500 yr, Sixes River estuary, southern Oregon. Geological Society of America Bulletin, 114(3): 298-314.

[45] Larsen, M., Wieczorek, G., Eaton, L. and Torres-Sierra, H., 2001. The rainfall-triggered landslide and flash flood disaster in northern Venezuela, December 1999. In: Proceedings of the 7*th* Federal Interagency Sedimentation Conference, Reno, NV, March 25-29, IV9-V16.

[46] Lee, H.J., Syvitski, P.M., Parker, G., Orange, D., Locat, J., Hutton, E.W.H., Imran, J., 2002. Distinguishing sediment waves from slope failure deposits: field examples, including the 'Humboldt slide' and modeling results. Marine Geology, 192(1-3): 79-104.

[47] Lee, K.L. and Duncan, J.M., 1975. Landslide of April 25, 1974 on the Mantaro River, Peru. In: Proceedings of the Committee on Natural Disasters. Commission of Sociotechnical Systems, National Research Council, Washington D.C., 72p.

[48] Leithold, E.L. and Blair, N.E., 2001. Watershed control on the carbon loading of marine sedimentary particles. Geochimica Et Cosmochimica Acta, 65(14): 2231-2240.

[49] Leithold, E.L. and Hope, R.S., 1999. Deposition and modification of a flood layer on the northern California shelf: Lessons from and about the fate of terrestrial particulate organic carbon. Marine Geology, 154(1-4): 183-195.

[50] Ludwig, W., Probst, J.L. and Kempe, S., 1996. Predicting the oceanic input of organic carbon by continental erosion. Global Biogeochemical Cycles, 10(1): 23-41.

[51] Mantua, N.J. and Hare, S.R., 2002. The Pacific decadal oscillation. Journal of Oceanography, 58(1): 35-44.

[52] Mantua, N.J., Hare, S.R., Zhang, Y., Wallace, J.M. and Francis, R.C., 1997. A Pacific interdecadal climate oscillation with impacts on salmon production. Bulletin of the American Meteorological Society, 78(6): 1069-1079.

[53] Meade, R.H., 1969. Landward transport of bottom sediments in estuaries of the Atlantic coastal plain. Journal of Sedimentary Petrology, 39(1): 222-234.

[54] Megahan, W.F., 1983. Hydrologic effects of clearcutting and wildfire on steep granitic slopes in Idaho. Water Resources Research, 19(3): 811-819.

[55] Meyer, G.A., Pierce, J.L., Wood, S.H. and Jull, A.J.T., 2001. Fire, storms, and erosional events in the Idaho batholith. Hydrological Processes, 15(15): 3025-3038.

[56] Meyer, G.A., Wells, S.G. and Jull, A.J.T., 1995. Fire and alluvial chronology in Yellowstone National Park: Climatic and intrinsic controls on Holocene geomorphic processes. Geological Society of America Bulletin, 107(10): 1211-1230.

[57] Milliman, J.D. and Kao, S.J., 2005. Hyperpycnal discharge of fluvial sediment to the ocean: Impact of Super-Typhoon Herb (1996) on Taiwanese rivers. Journal of Geology, 113(5): 503-516.

[58] Milliman, J.D. , Lin, S. W., Kao, S. J., Liu, J. P., Liu, C. S., Chiu, J. K., Lin, Y. C., 2007. Short-term changes in seafloor character due to flood-derived hyperpycnal discharge: Typhoon Mindulle, Taiwan, July 2004. Geology, 35(9): 779-782.

[59] Milliman, J.D. and Meade, R.H., 1983. World-wide delivery of river sediment to the oceans. Journal of Geology, 91(1): 1-21.

[60] Milliman, J.D. and Syvitski, J.P.M., 1992. Geomorphic/tectonic control of sediment discharge to the ocean: The importance of small mountainous rivers. Journal of Geology, 100(5): 525-544.

[61] Minobe, S., 1999. Resonance in bidecadal and pentadecadal climate oscillations over the North Pacific: Role in climatic regime shifts. Geophysical Research Letters, 26(7): 855-858.

[62] Minobe, S., 1997. A 50-70 year climatic oscillation over the North Pacific and North America. Geophysical Research Letters, 24(6): 683-686.

[63] Morris, S.E. and Moses, T.A., 1987. Forest fire and the natural soil erosion regime in the Colorado Front Range. Annals of the Association of American Geographers, 77(2): 245-254.

[64] Mulder, T. and Syvitski, J.P.M., 1995. Turbidity currents generated at river mouths during exceptional discharges to the world oceans. Journal of Geology, 103(3): 285-299.

[65] Nittrouer, C.A., 1999. STRATAFORM: overview of its design and synthesis of its results. Marine Geology, 154(1-4): 3-12.

[66] Norris, R.M. and Webb, R.W., 1990. Geology of California. New York: Wiley.

[67] Ogston, A.S. and Sternberg, R.W., 1999. Sediment-transport events on the northern California continental shelf. Marine Geology, 154(1-4): 69-82.

[68] Olson, J.S., Garrels, R. M., Berner, R. A., Armentano, T. V., Dyer, M. I., Yaalon, D. H., 1985. The natural carbon cycle. In: J. R. Trabalka (Ed.), Atmospheric carbon dioxide and the global carbon cycle. U.S. Dept. of Energy, Washington D.C., 175–213.

[69] Orange, D.L., 1999. Tectonics, sedimentation, and erosion in northern California: Submarine geomorphology and sediment preservation potential as a result of three competing processes. Marine Geology, 154(1-4): 369-382.

[70] Pain, C.F. and Bowler, J.M., 1973. Denudation following the November 1970 earthquake at Madang, Papua New Guinea. Zeitschrift fuer Geomorphologie Neue Fol. Suppl., 18: 92-104.

[71] Pearce, A.J. and Watson, A.J., 1986. Effects of earthquake-induced landslides on sediment budget and transport over a 50-yr period. Geology, 14(1): 52-55.

[72] Poppe, L.J. Eliason, A. H., Fredericks, J. J., Rendigs, R. R., Blackwood, D., Polloni, C. F., 2000. Grain-size analysis of marine sediments: Methodology and data processing. U.S. Geological Survey, open-file report 00-358, Chapter 1.

[73] Postma, H., 1967. Sediment transport and sedimentation in the estuarine environment. In: G.H. Lauff (Editor), Estuaries. American Association for the Advancement of Science, Washington D.C., 158-179.

[74] Prahl, F.G., Ertel, J.R., Goni, M.A., Sparrow, M.A. and Eversmeyer, B., 1994. Terrestrial organic carbon contributions to sediments on the Washington margin. Geochimica Et Cosmochimica Acta, 58(14): 3035-3048.

[75] Restrepo, J.D. and Kjerfve, B., 2000. Water discharge and sediment load from the western slopes of the Colombian Andes with focus on Rio San Juan. Journal of Geology, 108(1): 17-33.

[76] Roering, J.J. and Gerber, M., 2005. Fire and the evolution of steep, soil-mantled landscapes. Geology, 33(5): 349-352.

[77] Schuster, R.L. and Costa, J.E., 1986. A perspective on landslide dams. In: R.L. Schuster (Ed), Landslide dams: Processes, risk, and mitigation. American Society of Civil Engineers, New York, 1-20.

[78] Schwehr, K., Driscoll, N. and Tauxe, L., 2007. Origin of continental margin morphology: Submarine-slide or downslope current-controlled bedforms, a rock magnetic approach. Marine Geology, 240(1-4): 19-41.

[79] Shin, T.C., Kuo, K.W., Lee, W.H., Teng, T.L. and Tsai, Y.B., 2000. A preliminary report on the 1999 Chi-Chi (Taiwan) earthquake. Seismological Research Letters, 71(1): 24-30.

[80] Simonett, D.S., 1967. Landslide distribution and earthquakes in the Bewani and Torricelli mountains, New Guinea; a statistical analysis. In: J.N. Jennings and J.A. Mabbutt (Eds), Landform studies from Australia and New Guinea. Cambridge University Press, Cambridge, 64-84.

[81] Sloan, J., Miller, J.R. and Lancaster, N., 2001. Response and recovery of the Eel River, California, and its tributaries to floods in 1955, 1964, and 1997. Geomorphology, 36(3-4): 129-154.

[82] Snow, D.T., 1964. Landslide of Cerro Condor-Sencca, department of Ayacucho, Peru. In: G.A. Kiersch (Ed), Engineering geology case histories. Geological Society of America, 5: 1-6.

[83] Sommerfield, C.K., Aller, R.C. and Nittrouer, C.A., 2001. Sedimentary carbon, sulfur, and iron relationships in modern and ancient diagenetic environments of the Eel River Basin (USA). Journal of Sedimentary Research, 71(3): 335-345.

[84] Sommerfield, C.K. and Nittrouer, C.A., 1999. Modern accumulation rates and a sediment budget for the Eel shelf: A flood-dominated depositional environment. Marine Geology, 154(1-4): 227-241.

[85] Spencer, T. and Douglas, I., 1985. The significance of environmental change: Diversity, disturbance and tropical ecosystems. In: I. Douglas and T. Spencer (Eds), Environmental change and tropical geomorphology. George Allen & Unwin, London, 13-33.

[86] Stallard, R.F., 1998. Terrestrial sedimentation and the carbon cycle: Coupling weathering and erosion to carbon burial. Global Biogeochemical Cycles, 12(2): 231-257.

[87] Swanson, F.J., 1981. Fire and geomorphic processes. In: Proceedings of the Fire Regimes and Ecosystems Conference, Honolulu, HI, December 11-15, 1979. U.S. Department of Agriculture, Forest Service, General Technical Report WO-26, 401-420.

[88] Syvitski, J.P. and Morehead, M.D., 1999. Estimating river-sediment discharge to the ocean: Application to the Eel margin, northern California. Marine Geology, 154(1-4): 13-28.

[89] Tissot, B.P. and Welte, D.H., 1978. Petroleum formation and occurrence: A new approach to oil and gas exploration. Spring-Verlag, New York.

[90] Tourre, Y.M., Rajagopalan, B., Kushnir, Y., Barlow, M. and White, W.B., 2001. Patterns of coherent decadal and interdecadal climate signals in the Pacific Basin during the 20th century. Geophysical Research Letters, 28(10): 2069-2072.

[91] Twiss, R.J. and Moores, E.M., 1992. Structural geology. W.H. Freeman and Company, New York.

[92] Warrick, J.A. and Milliman, J.D., 2003. Hyperpycnal sediment discharge from semiarid southern California rivers: Implications for coastal sediment budgets. Geology, 31(9): 781-784.

[93] Wells, R.E., Blakely, R.J., Sugiyama, Y., Scholl, D., 2002. Coseismic slip beneath forearc basins in great subduction zone earthquakes: Implications for the size and mode of rupture on the Cascadia Subduction Zone. In: Eos, Transactions of the American Geophysical Union, 83 (47, Suppl.). American Geophysical Union, Washington D.C., F1073.

[94] Witter, R.C., Kelsey, H.M. and Hemphill-Haley, E., 2003. Great Cascadia earthquakes and tsunamis of the past 6700 years, Coquille River estuary, southern coastal Oregon. Geological Society of America Bulletin, 115(10): 1289-1306.

[95] Wondzell, S.M. and King, J.G., 2003. Postfire erosional processes in the Pacific Northwest and Rocky Mountain regions. Forest Ecology and Management, 178: 75-87.

[96] Woodruff, J.D., Geyer, W.R., Driscoll, N., Sommerfield, C., 1998. Sediment deposition within the Hudson River estuary. In: Eos, Transactions of the American Geophysical Union, 79 (45, Suppl.). American Geophysical Union, Washington D.C., F451.

Figures

Figure 1. Patterns of landsliding generated along the coastal ranges of northern Venezuela by prolonged heavy rains, December 14 - 16, 1999. Greyscale topographic map on top, contoured at 250 m, shows locations of images of landsliding below. (A) Oblique aerial view of landslide-affected coastal hills of the Los Corales region, north of the Venezuelan capital, with the developed strip along the coast in the background. (B) Part of low-level air photo over the Quebrada Seca area. Inset shows damaged buildings. Landslides are clearly visible as the light areas in aerial photography images. Darker areas are vegetation remaining on hillslopes, which reflect less solar radiation compared to landslide-denuded slopes.

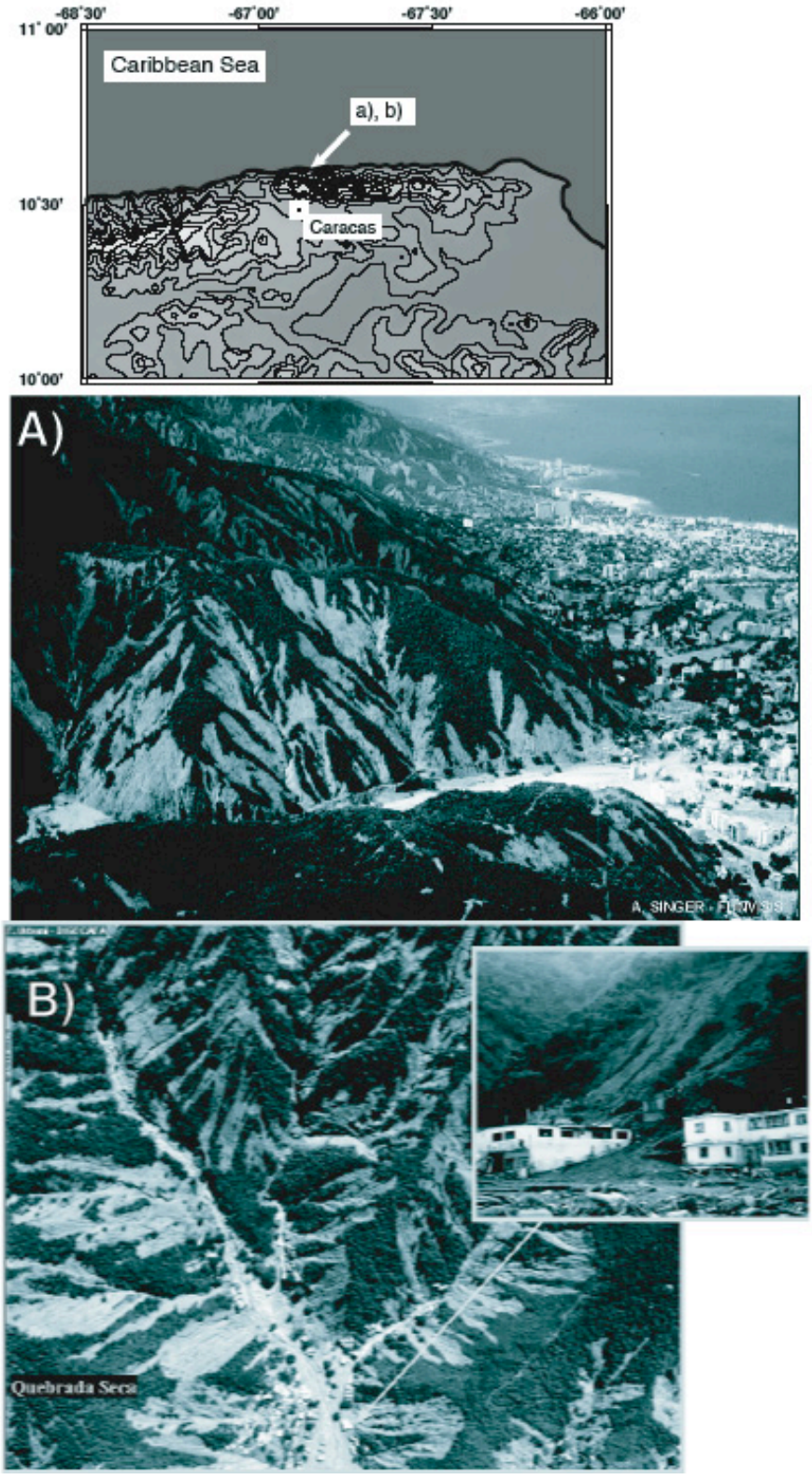
-68°30'
-67°00'
-67°30'
-66°00'
11° 00'
10°30'
10°00'
Caribbean Sea
a), b)
Caracas
A)
B)
Quebrada Seca

Figure 2. Patterns of landsliding generated in the western foothills region of central Taiwan by the 1999 M_w = 7.6 Chi-Chi earthquake. Location of epicenter for the Chi-Chi main shock is indicated by the filled yellow circle, the surface rupture produced by the event by the solid white line, offshore areas are blue, and locations of post-earthquake satellite remote sensing data shown on the right by the white rectangles. Landslides generated by the Chi-Chi earthquake show as light areas in these perspective views of Indian Research Satellite 5m panchromatic imagery draped over the 40m DEM. (A) View from the west with the Tsaoling landslide (.046 km^3) in the foreground. Note damming of the river upstream of slide, and large landslides from ridges marginal to the plateau area in the background. (B) View from the south showing extensive landsliding from the tops of ridges marginal to a large plateau area. View of Tsaoling Mountain from the south (C) before and (D) after the Chi-Chi earthquake, the latter showing the Tsaoling landslide. Photographs (C) and (D) taken from [13].

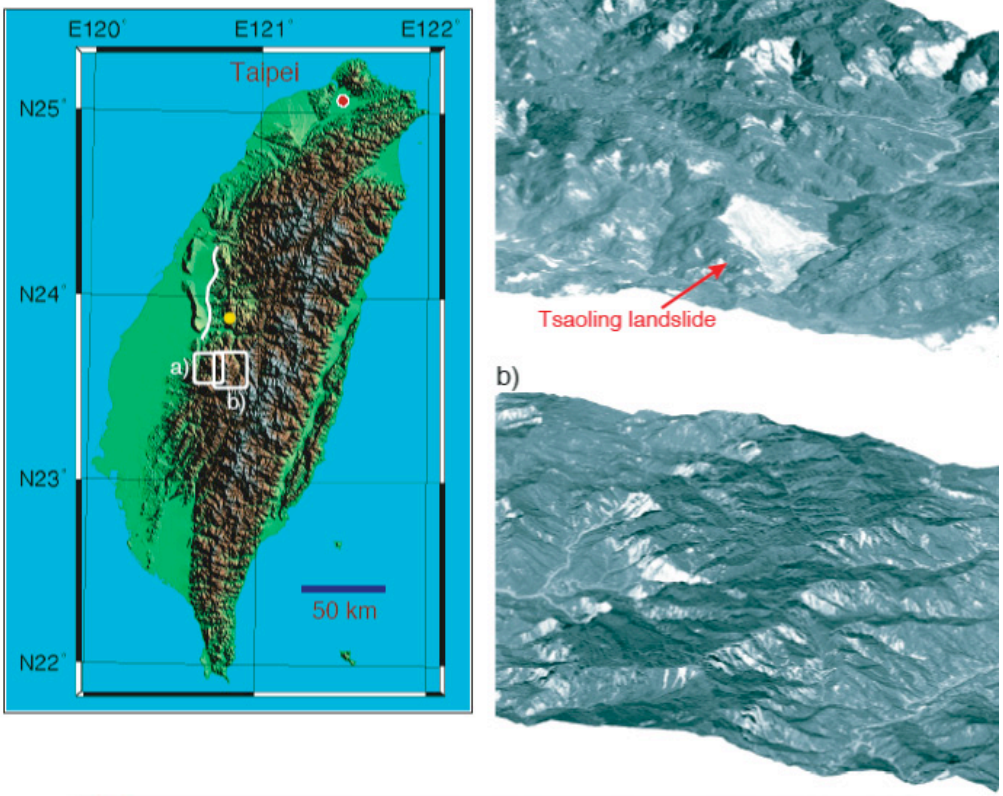
E120°
E121°
E122°
N25°
N24°
N23°
N22°
Taipei
a)
b)
50 km
a)
Tsaoling landslide
b)


c)


d)

Figure 3. Landsliding caused an enormous amount of sediment and biomass to be delivered to the valley floor after the Hebgen Lake, Montana earthquake of August 17, 1959. As a result of the landsliding, Madison River was dammed, creating Earthquake Lake, shown above. Photograph taken from [77].

Figure 4. Sediment and biomass liberated from landslides are capable of filling channels and damming rivers. The landslide resulting from the Wenchuan, China earthquake of 2008 dammed the Jian River, creating Tangjiashan Lake, which had a volume of .128 km^3.

Figure 5. High-resolution chirp and multi-channel seismic (MCS) profiles along the Eel margin illustrate that the surface morphology and subsurface structure are poorly correlated along the margin because the synclines and anticlines trend at high angles to the shoreline. (A). Note the erosional surface formed during the Holocene sea level rise has marked relief along the Eel margin indicative of recent tectonic deformation. (B). The MCS profile illustrates that the deformation is long lived and leads to large basin development (>2 km since early Miocene) with enhanced potential for preservation of sediment and organic matter. (C) Location map for profiles A and B. The blotchy acoustic character, lack of internal reflectors, and gas chimneys, together with geochemical evidence, attest to the regional presence of biogenic gas in the Eel Syncline.

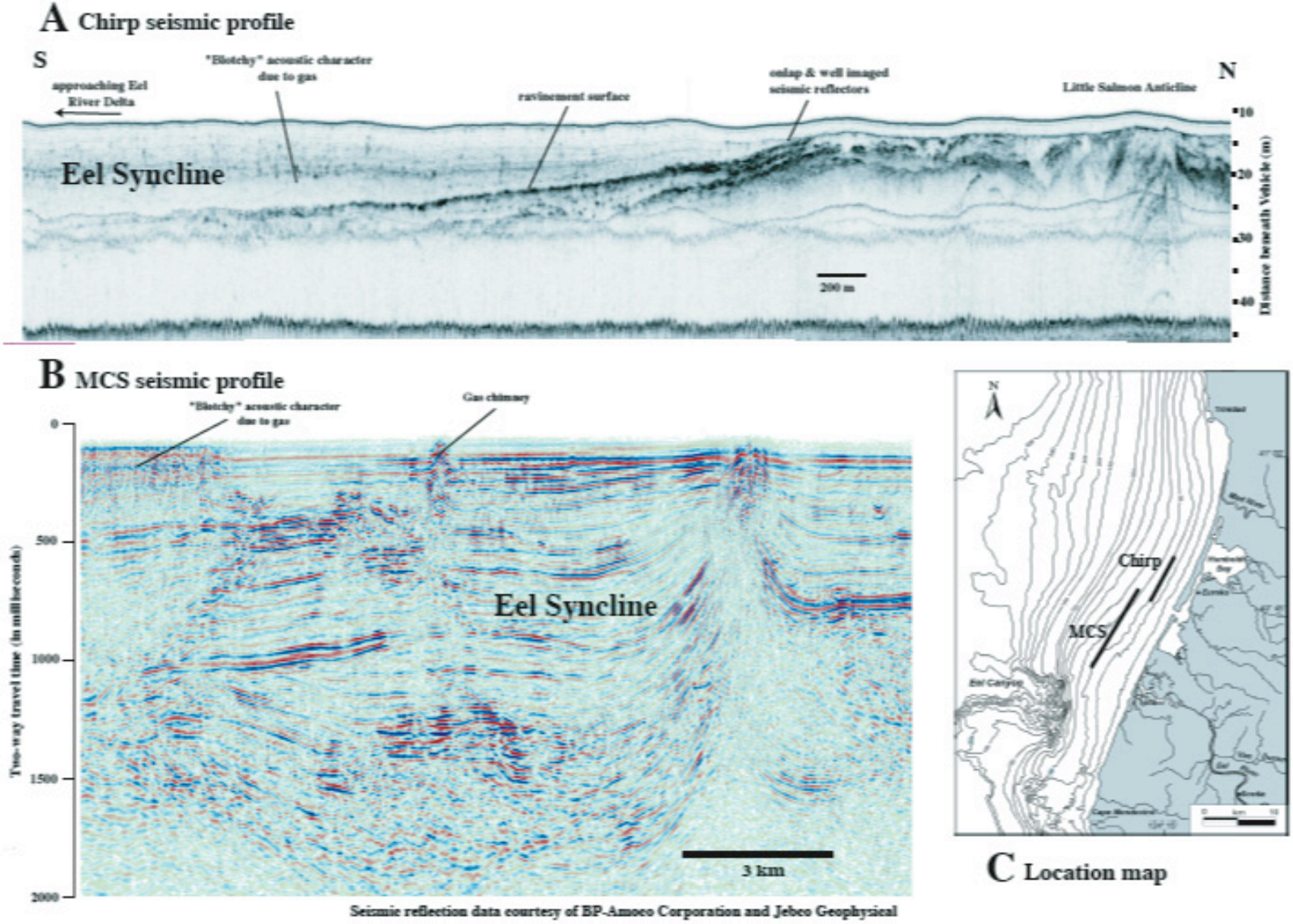

Seismic reflection data courtesy of BP-Amoco Corporation and Jebco Geophysical

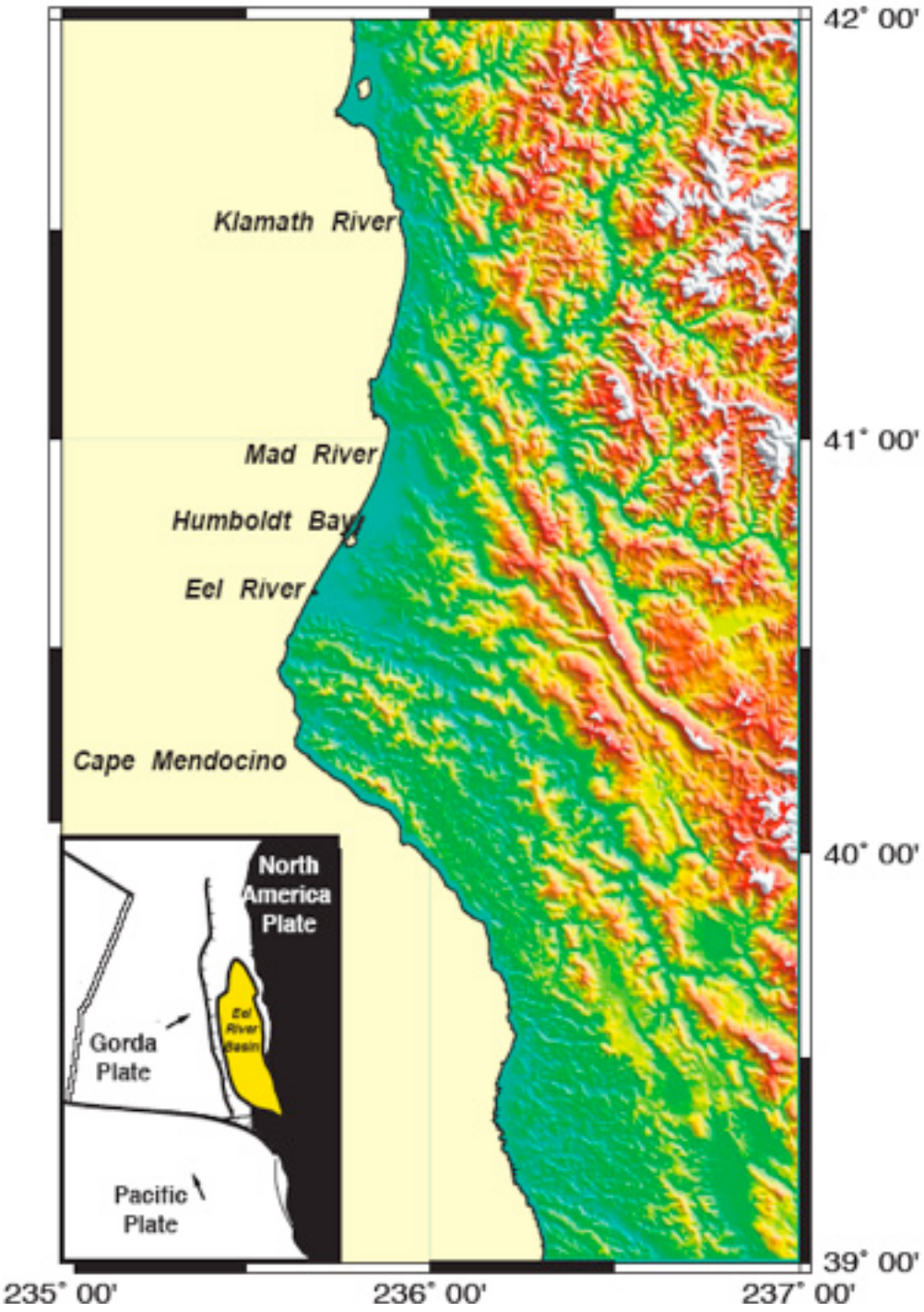

Figure 6. The Eel Margin resides north of the Mendocino Triple Junction, which causes the region to be characterized by many NW-SE trending folds and faults due to the compressional interaction between the three tectonic plates. The continuous deformation extending throughout the region increases the potential for landsliding.

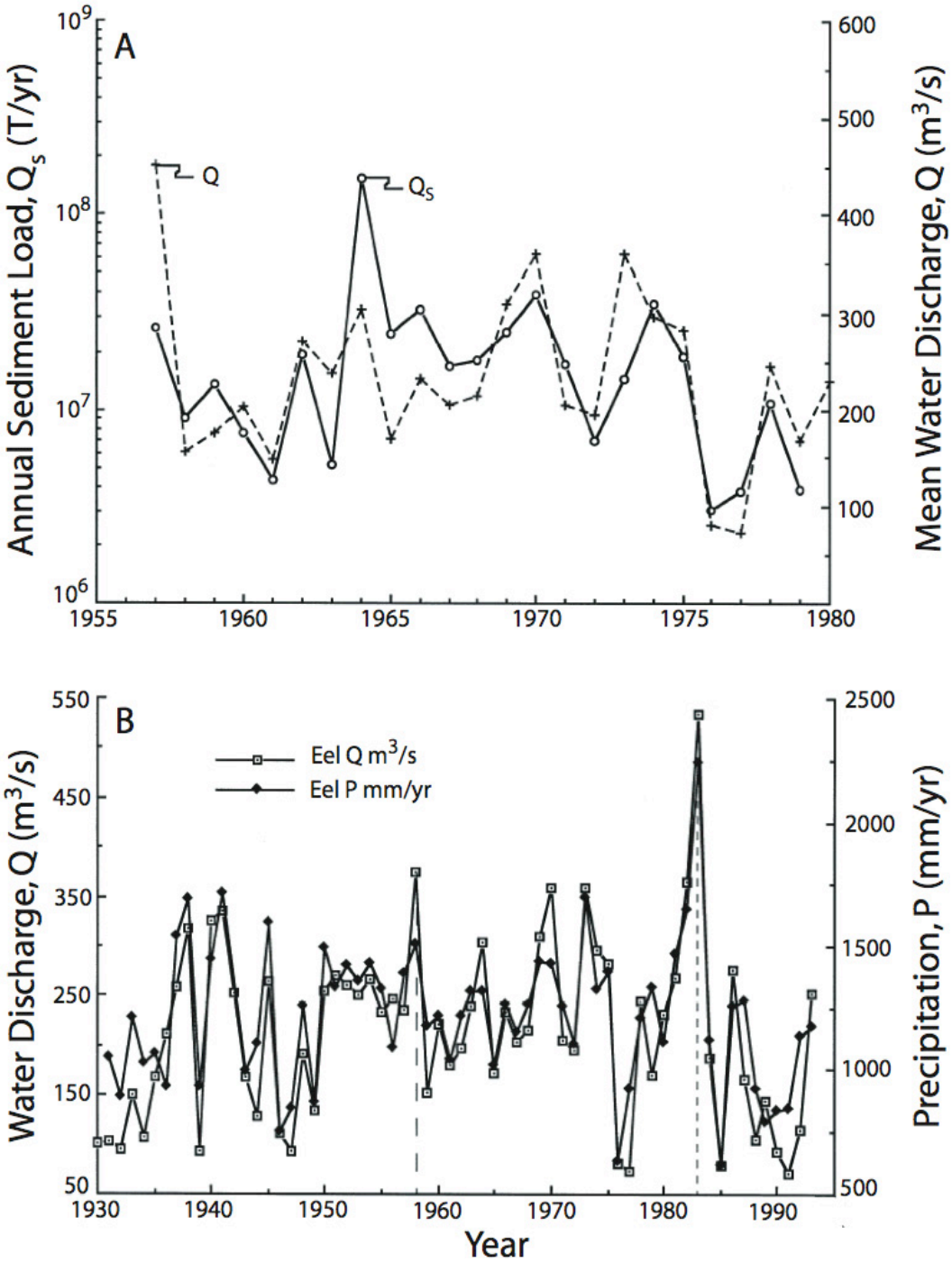

Figure 7. (A) A strong correlation exists between annual sediment load and mean water discharge of the Eel River. (B) A comparison between water discharge and precipitation measured at Scotia supports the idea that the Eel River is an event-driven system resulting in hyperpycnal discharges. Figures taken from [88].

Figure 8. EdgeTech XStar CHIRP seismic line collected in 1999. This NW-SE trending line images the sediment waves at the toe of the Humboldt slide discussed in the text. Locations of the cores are labeled, along with the error associated with the location of coring. Note the seaward-dipping layers migrating upslope. Figure modified from [78].

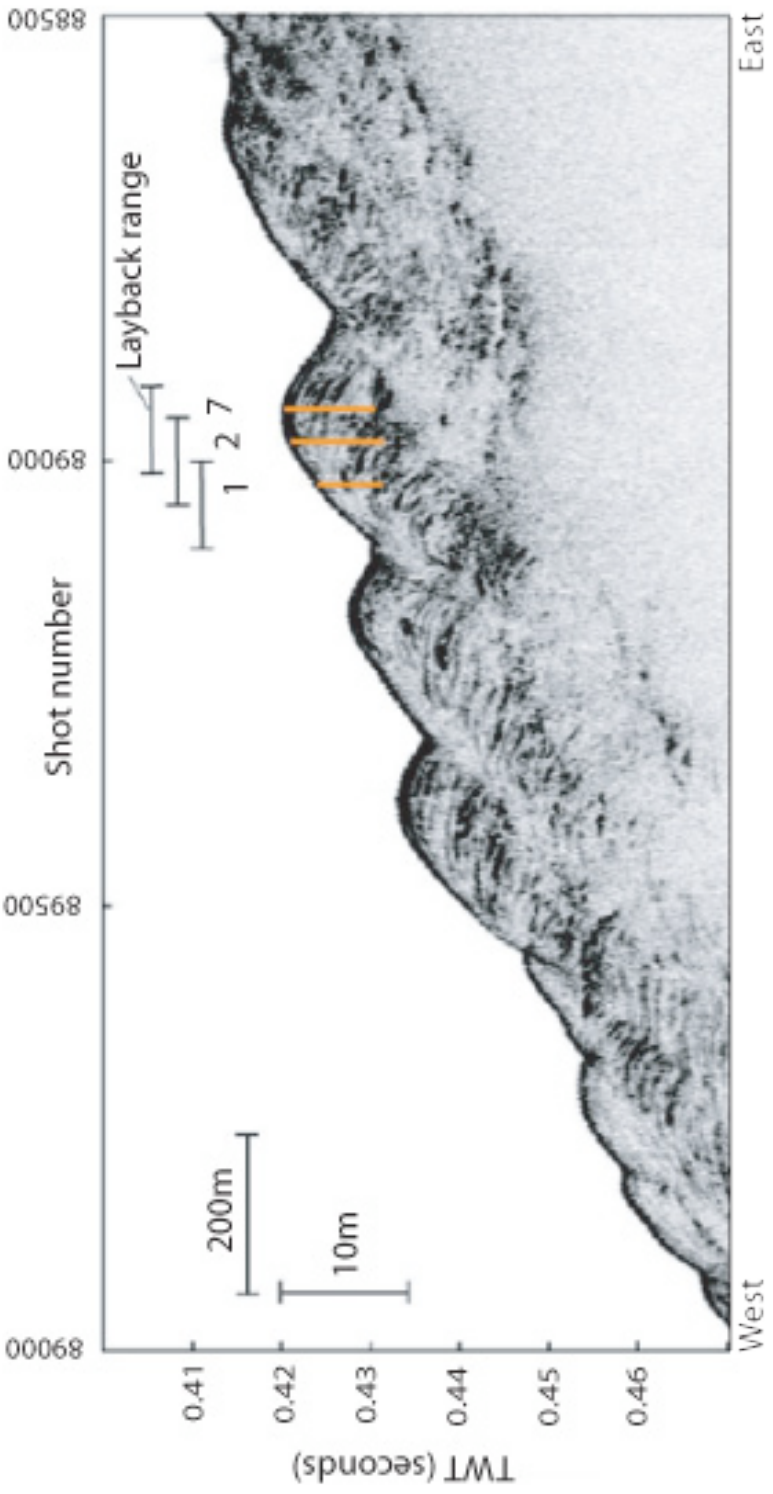
Layback range
1
2
7
200m
10m
East
West
Shot number
00068
89500
00068
0.41
0.42
0.43
0.44
0.45
0.46
TWT (seconds)

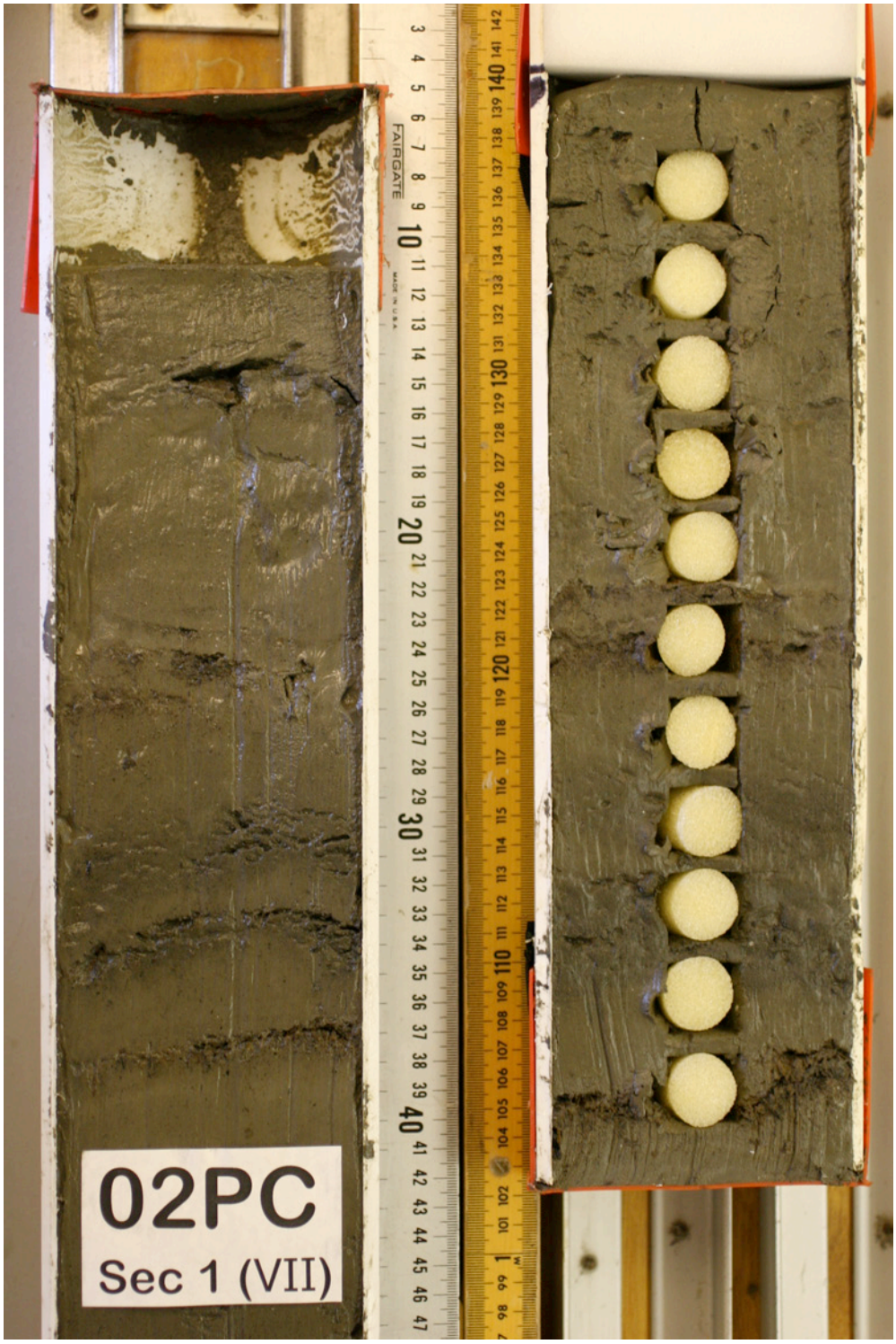

Figure 9. Photograph of the top piston core 02 (left) and its corresponding trigger core. Four POC layers can be identified in each core, indicating a correlation between the cores. It is evident that only ~5cm is missing from the top of the piston core (scale in cm).

Figure 10. Photographs of piston cores 01 and 02. Dark brown layers are those composed almost entirely of vascular plant debris (scale in cm). (A) Evidence for erosion into underlying sediment at the base of the fining-upward package. (B) Core 02PC exhibiting the largest layer of POC that is >8cm thick.

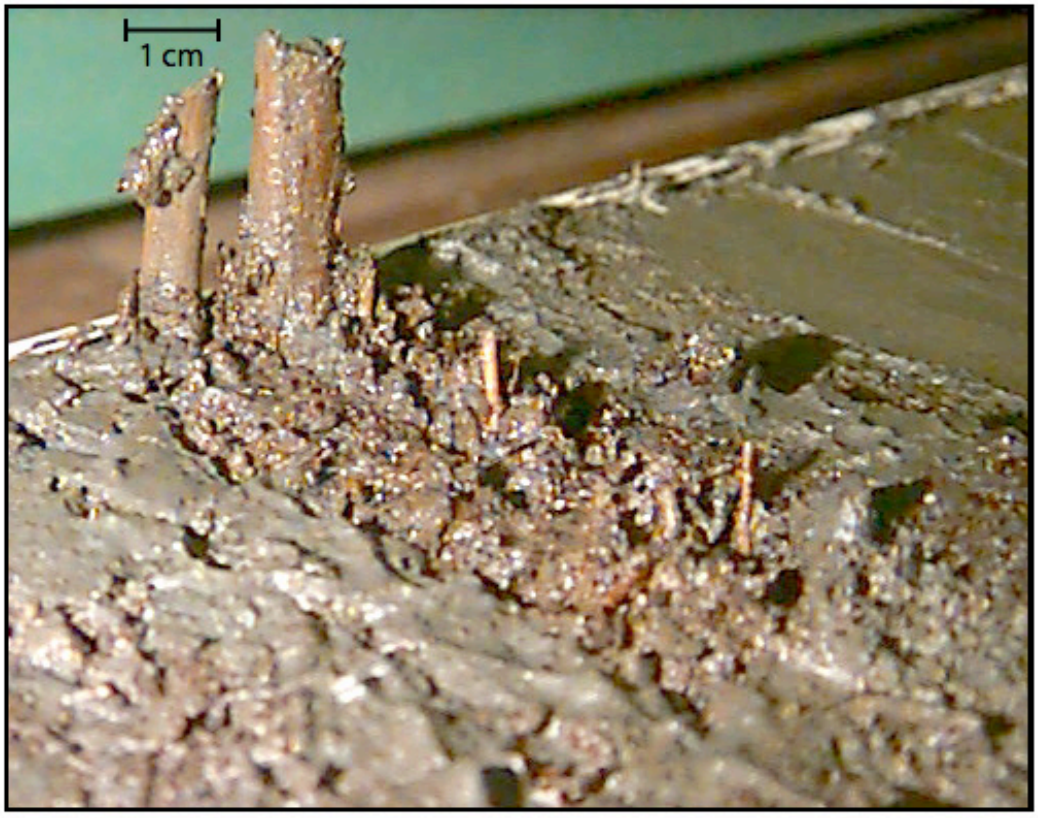

Figure 11. Photograph of vascular plant debris several centimeters in length within a POC layer (photograph courtesy of Kurt Schwehr).

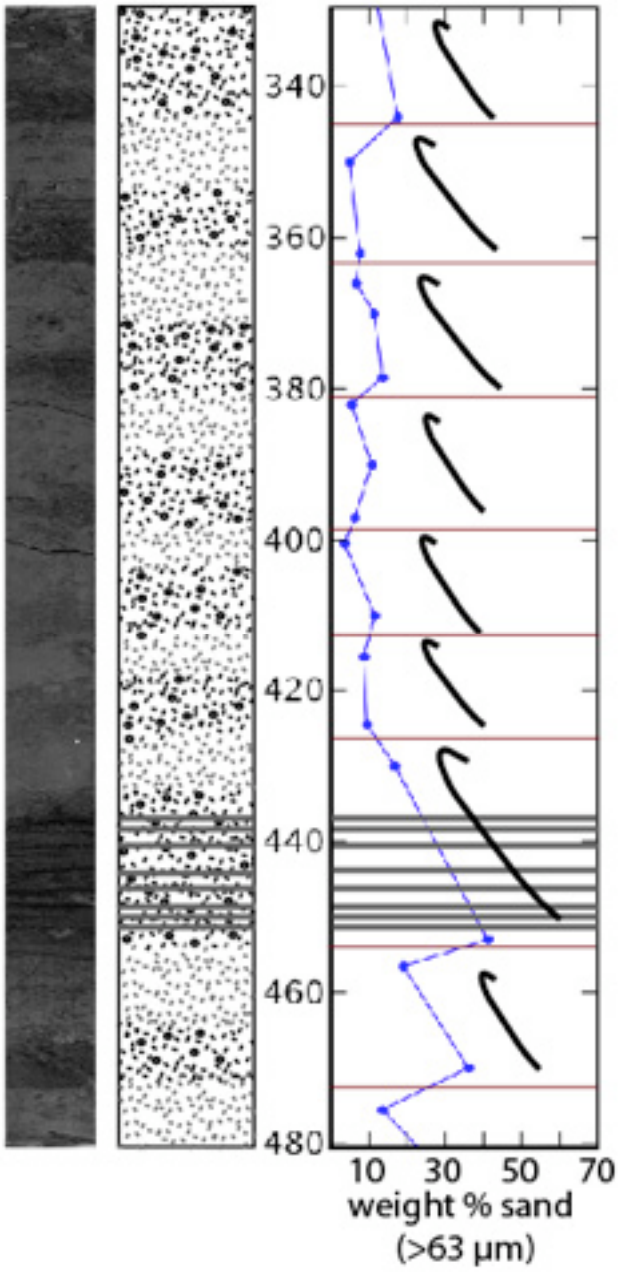

Figure 12A. Fining-Upward Packages. Photograph and depiction of section 4 of core 07PC, aligned with the corresponding coarse-grained weight percentages. Red lines indicate the bases of the fining-upward packages and arrows denote the normal grading found within each package. Gray bars represent POC layers.

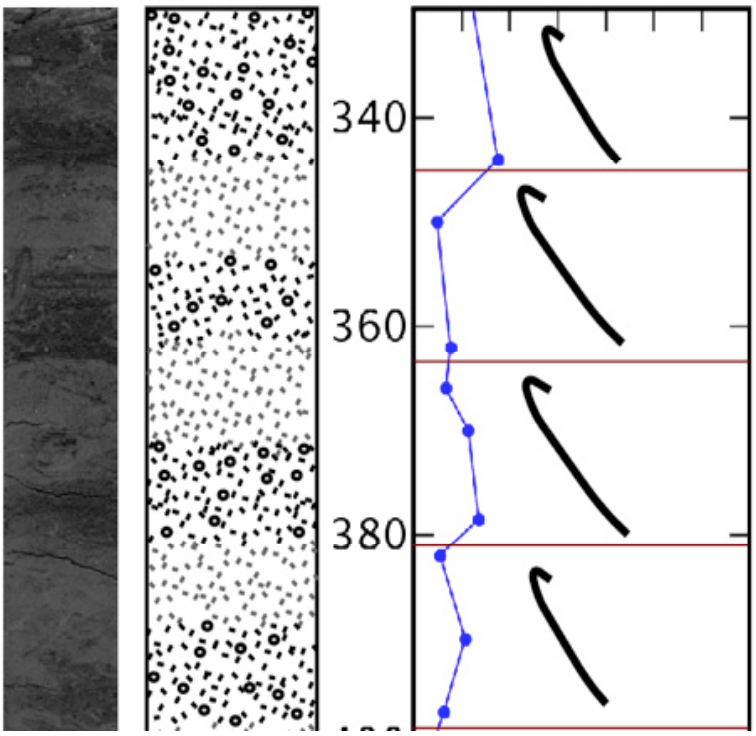

Figure 12B. Fining-Upward Packages, Continued. Enlargement of 12A. Notice a clear visual distinction of the bases of the fining-upward packages. Bioturbation in the middle of the fourth package near the bottom of the photograph may be responsible for the deviation from normal grading.

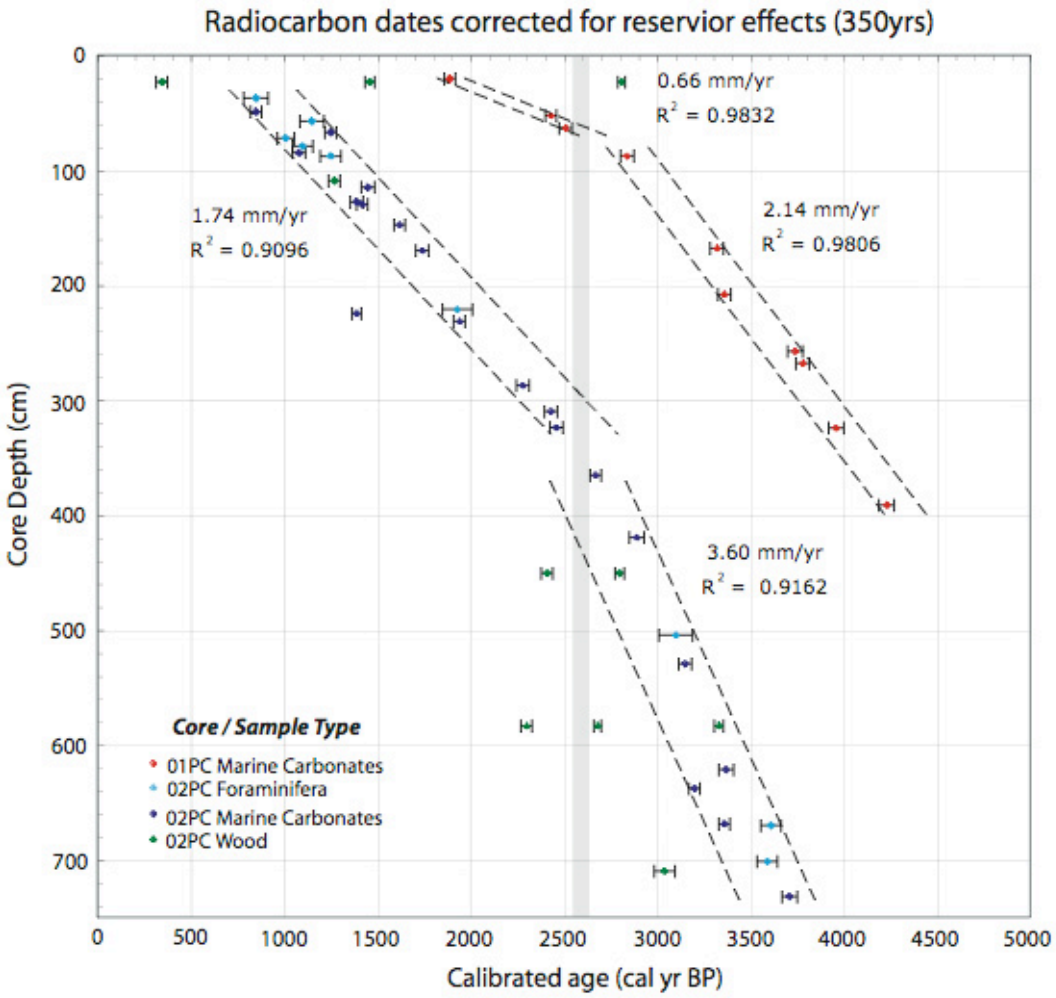

Figure 13. Accumulation rates for cores 01PC and 02PC based on linear regressions of radiocarbon ages of marine carbonate tests. Note accumulation rate for core 01PC is less than that of core 02PC. Solid lines, using the accumulation rates from the best fit line, envelope 95% of dates and are used to estimate age ranges of fining-upward packages and POC layers (see tables 5 and 6). Note also that both cores exhibit a change in accumulation rate at about 2600yr BP.

Figure 14. Core Correlations. The coarse grain size weight percentages are correlated with respect to the largest peak in each core (see text). The coarse grain size data for core 02PC is thought to be biased due to an instrumental defect of the sieve used for those particular samples because all samples have a significantly smaller weight percentage than samples from the other cores. The relative coarseness of each sample throughout the core, however, is accurate for the same sieve was used for each sample. Brown lines represent POC layers. Dates (yrs BP) to the right of the graphs in brown text, corresponding to the POC layers, were calculated linearly using the closest radiocarbon date above and below the base of the layer. Black lines represent bases of the fining-upward packages. Dates for core 01PC corresponding to the fining-upward packages were calculated using the above method. Dates for core 02PC corresponding to the fining-upward packages were calculated using the accumulation rates from figure 13. Small numbers next to the POC layers are the number of layers in close proximity. Question marks denote fining-upward packages that were not identified visually when examining the core and were reinterpreted to be bases based on the grain size distribution. Dashed lines represent those bases that were initially identified visually, but were reinterpreted and disregarded based on the grain size distribution.

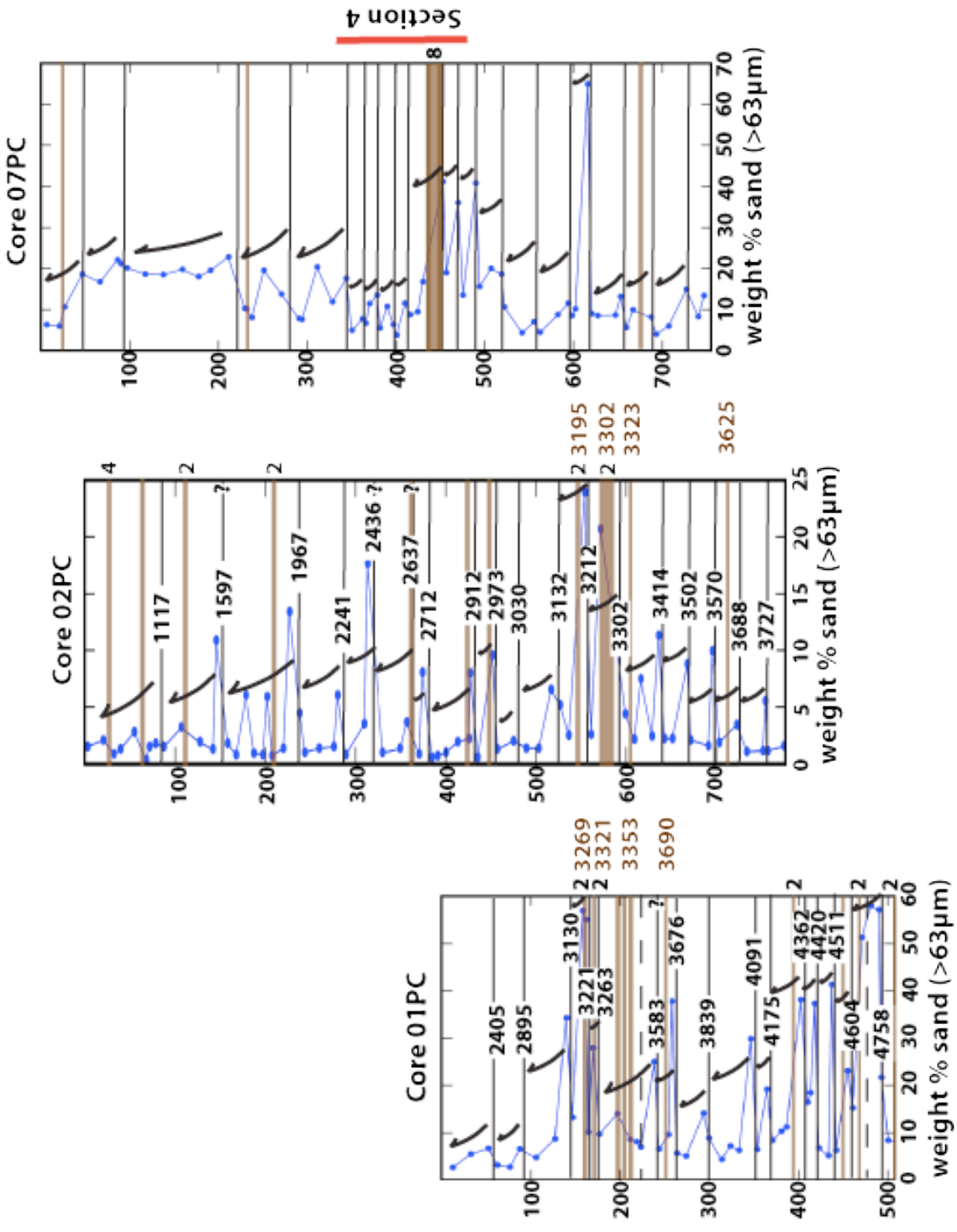
Core 07PC
Section 4
weight % sand (>63µm)
Core 02PC
1117
1597
1967
2241
2436
2637
2712
2912
2973
3030
3132
3212
3302
3414
3502
3570
3688
3727
3195
3302
3323
3625
weight % sand (>63µm)
Core 01PC
2405
2895
3130
3221
3263
3269
3321
3353
3583
3676
3690
3839
4091
4175
4362
4420
4511
4604
4758
weight % sand (>63µm)

Figure 15. The number of fining-upward packages binned (A) with respect to their thickness for cores 01PC, 02PC, and 07PC and (B) with respect to time for core 01PC and 02PC.

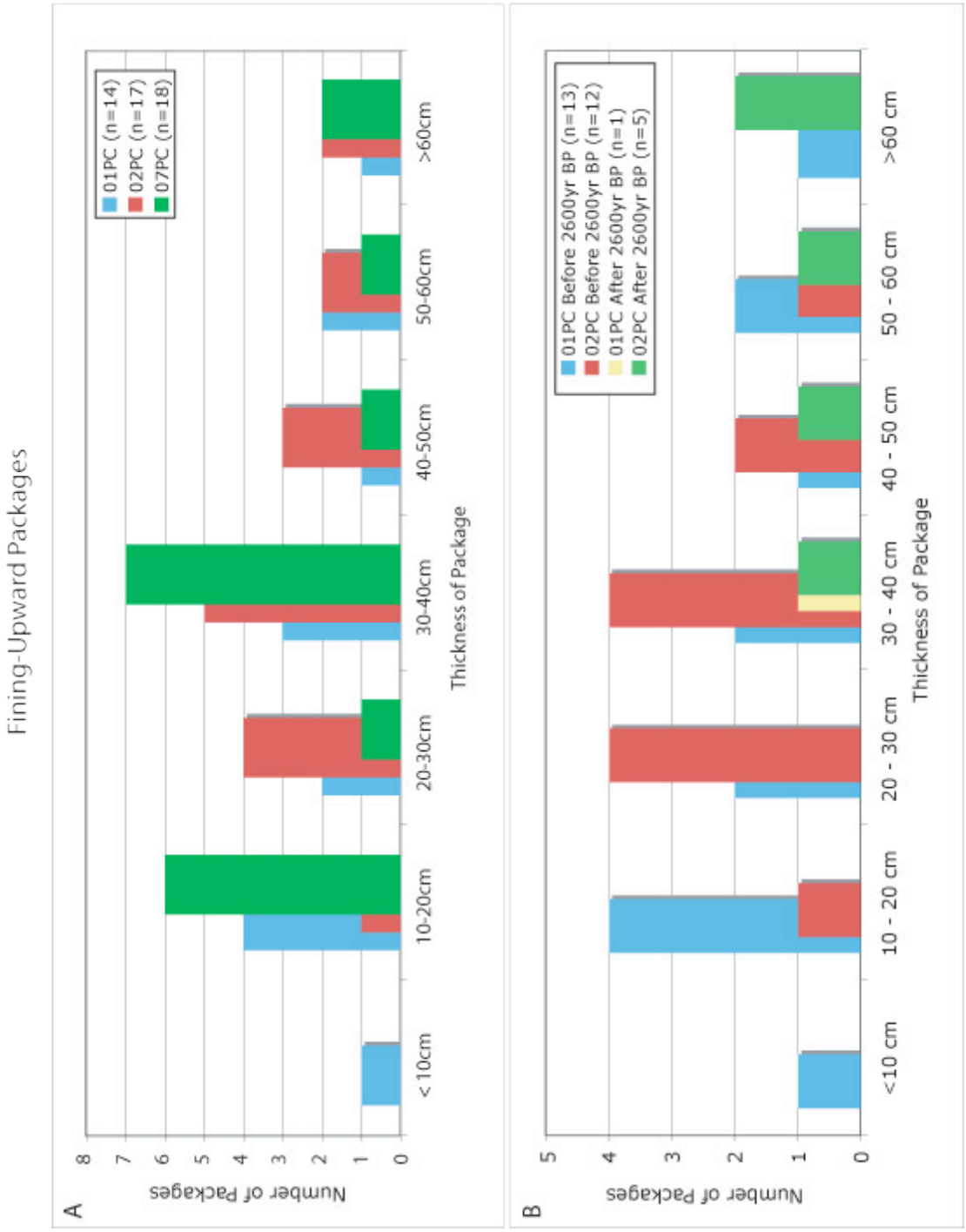
Fining-Upward Packages
A
01PC (n=14)
02PC (n=17)
07PC (n=18)
Number of Packages
0
1
2
3
4
5
6
7
8
< 10cm
10-20cm
20-30cm
30-40cm
40-50cm
50-60cm
>60cm
Thickness of Package
B
01PC Before 2600yr BP (n=13)
02PC Before 2600yr BP (n=12)
01PC After 2600yr BP (n=1)
02PC After 2600yr BP (n=5)
Number of Packages
0
1
2
3
4
5
<10 cm
10 - 20 cm
20 - 30 cm
30 - 40 cm
40 - 50 cm
50 - 60 cm
>60 cm
Thickness of Package

Figure 15, continued. (C) The number of fining-upward packages binned with respect to the duration of deposition.

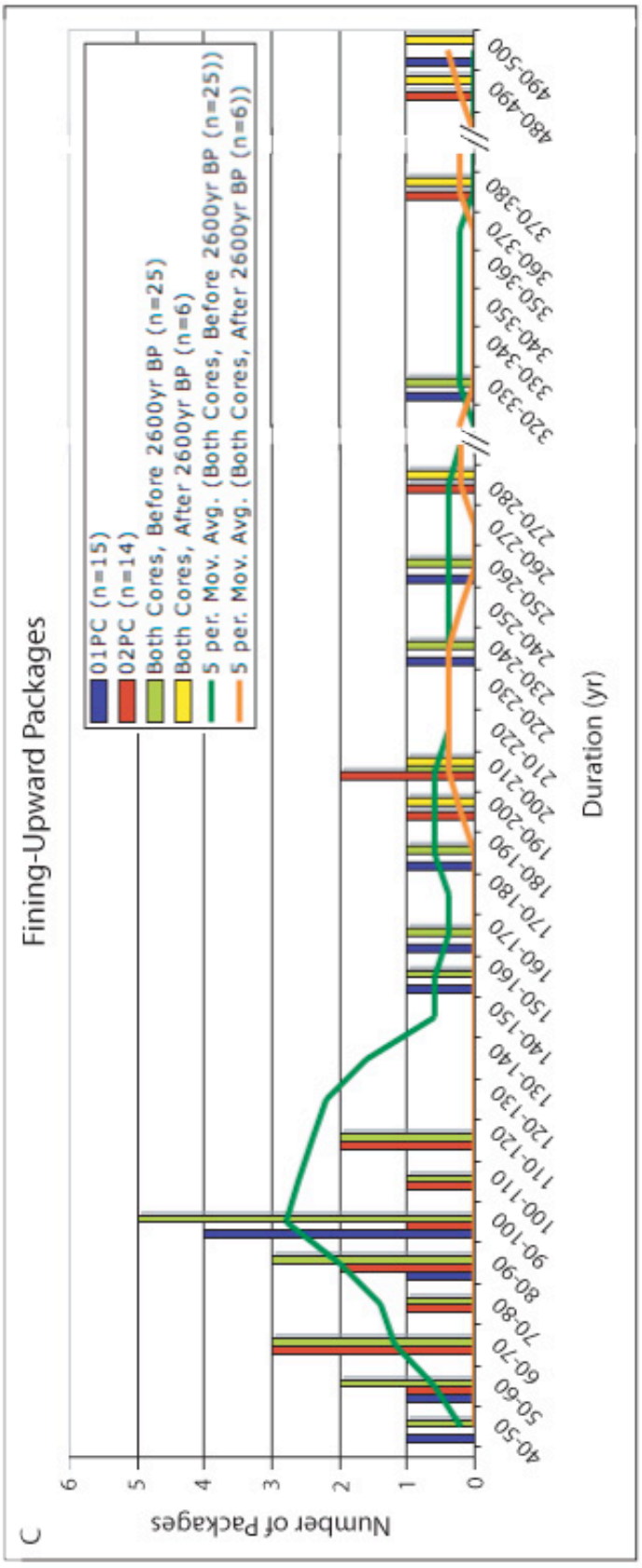
C
Fining-Upward Packages
Number of Packages
0
1
2
3
4
5
6
Duration (yr)
01PC (n=15)
02PC (n=14)
Both Cores, Before 2600yr BP (n=25)
Both Cores, After 2600yr BP (n=6)
5 per. Mov. Avg. (Both Cores, Before 2600yr BP (n=25))
5 per. Mov. Avg. (Both Cores, After 2600yr BP (n=6))
40-50
50-60
60-70
70-80
80-90
90-100
100-110
110-120
120-130
130-140
140-150
150-160
160-170
170-180
180-190
190-200
200-210
210-220
220-230
230-240
240-250
250-260
260-270
270-280
320-330
330-340
340-350
350-360
360-370
370-380
480-490
490-500

Figure 16. The release of Tangjiashan Lake and the resulting riverbank erosion.

Figure 17. A comparison of radiocarbon age estimates for earthquakes (EQ) along the Cascadia subduction zone (CSZ). The x-axis delineates the distance north along the CSZ away from the Humboldt slide and the y axis defines the calibrated ages of the POC layers, in calendar years before present (BP). All EQ ages determined by radiocarbon dating (^{14}C). Each colored bar at the Humboldt Slide represents one POC layer, with the various colors grouping the layers by the fining-upward package in which each layer has been deposited. Green bars represent ages of EQs determined by buried marsh soils or elevated terraces near Humboldt Bay [14]. Blue bars with 2σ error bars represent dated turbidites from the Juan de Fuca Canyon thought to record onshore EQs [27]. Gray vertical bars represent ages of EQs determined by buried marsh soils and tsunami deposits at specified sites. The grey circles represent approximate ages of EQs not directly dated by ^{14}C. For details on individual events, see [94] and references therein. This figure is modified from [94].

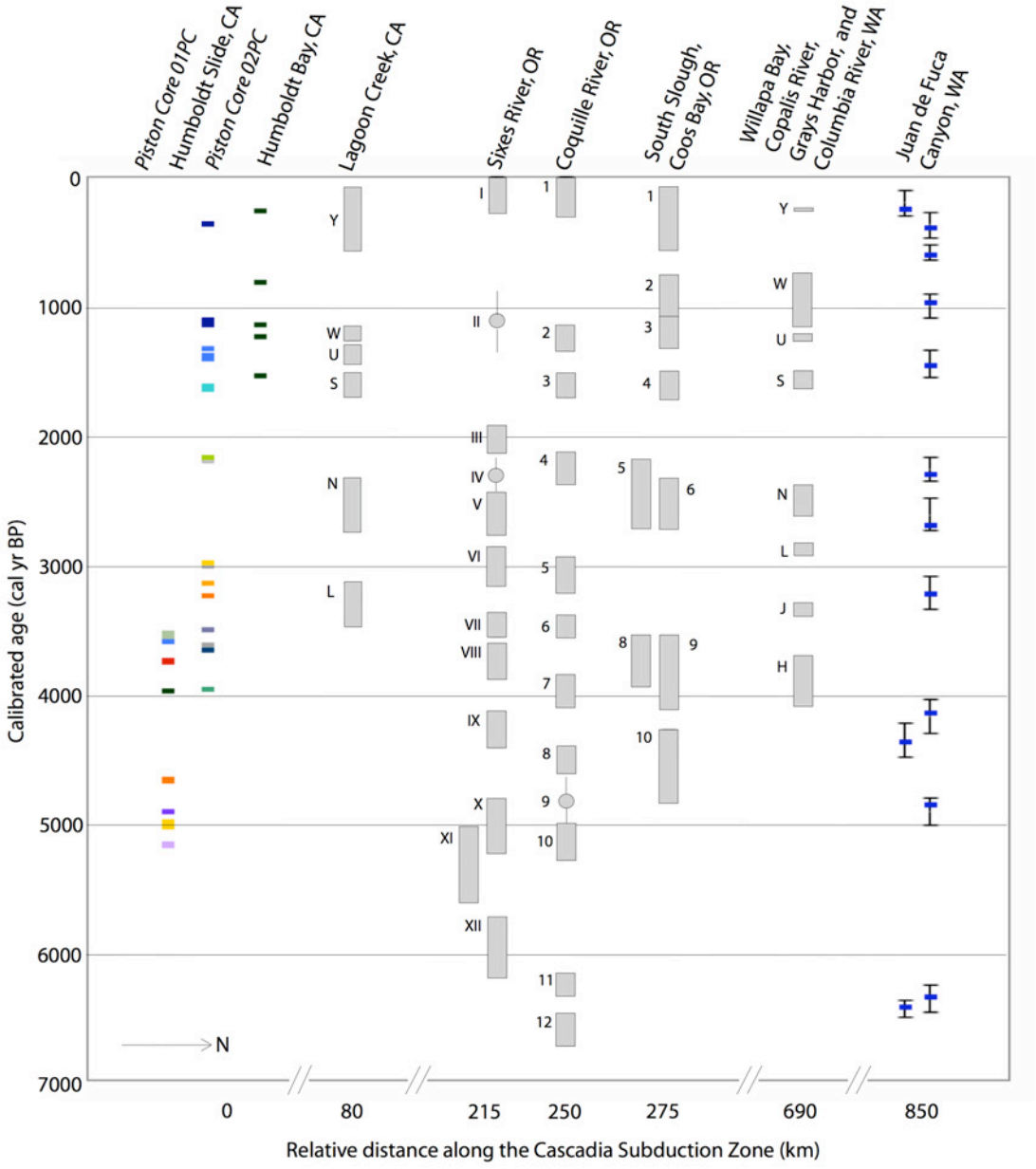
Piston Core 01PC
Humboldt Slide, CA
Piston Core 02PC
Humboldt Bay, CA
Lagoon Creek, CA
Sixes River, OR
Coquille River, OR
South Slough, Coos Bay, OR
Willapa Bay, Copalis River, Grays Harbor, and Columbia River, WA
Juan de Fuca Canyon, WA
Calibrated age (cal yr BP)
0
1000
2000
3000
4000
5000
6000
7000
N
0
80
215
250
275
690
850
Relative distance along the Cascadia Subduction Zone (km)

Figure 18. Huntec line L – 145X images the main body of the Humboldt slide. A transparent drape of hemipelagic sediment overlies the upslope-migrating sediment layers, evidence that typical sediment wave accumulation has ceased. This figure was modified from [24].

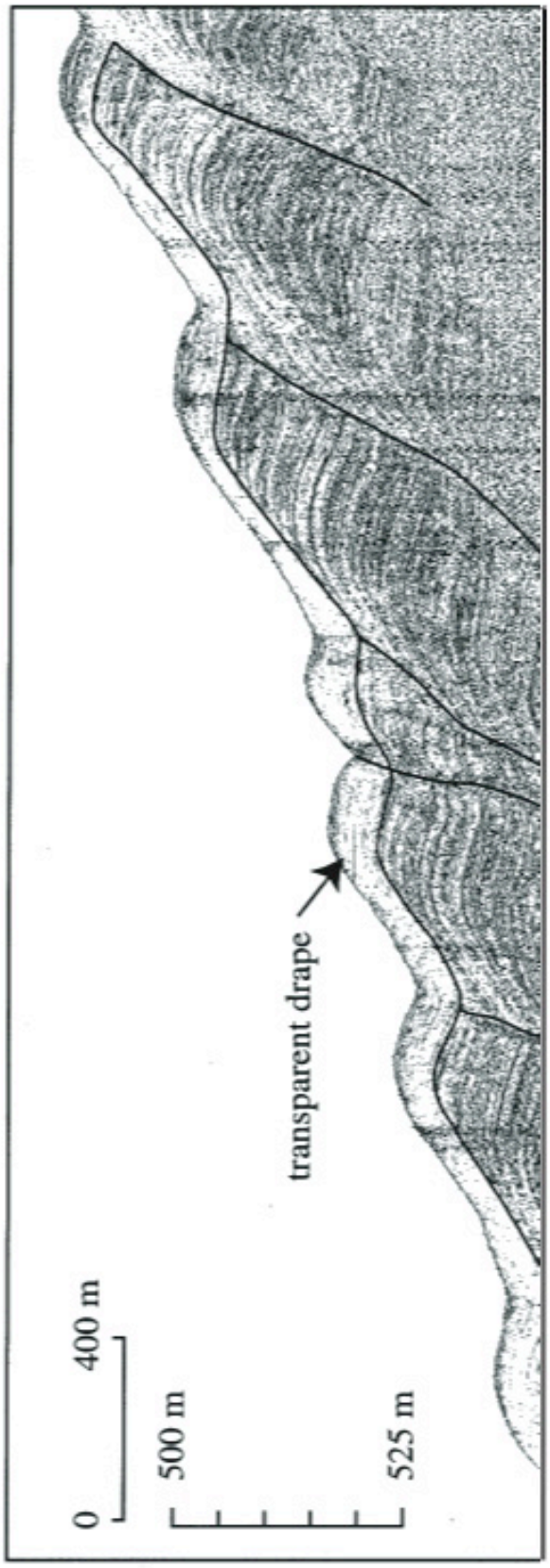
transparent drape
0
400 m
500 m
525 m

These figures, in part, are currently being prepared for submission for publication of the material. McCullough, Justin S.; Driscoll, Neal W. The thesis author was the primary investigator and author of this material.

Tables

Table 1: Core Locations and Lengths

Core #	Water Depth (m)	Latitude	Longitude	Length (cm)	Trigger Core Length (cm)	Trigger-Piston Correlation	Missing Sediment (cm)
01PC	460	124°30"09.96' W	40°50"20.16' N	508	119.5	No	>119.5
02PC	460	124°30"07.62' W	40°50"19.86' N	786.5	175.5	Yes	5
07PC	461	124°30"05.84' W	40°50"19.87' N	755	85.5	Yes	5

Table 2A. 01PC Sediment Sample Weights

#	depth (cm)	sample wt (g)	water wt. (g)	salt wt. (g)	sediment wt. (g)	>63µm wt. (g)	wt. % coarse
1	12.5	43.38	13.83	0.48	29.07	0.77	2.65
2	32.5	41.81	13.12	0.46	28.23	1.54	5.46
3	52.5	43.26	13.23	0.46	29.57	1.97	6.66
4	62.5	43.38	13.56	0.47	29.35	0.92	3.14
5	76.5	41.56	12.04	0.42	29.10	0.78	2.68
6	87.5	51.38	13.46	0.47	37.45	2.45	6.54
7	105.5	52.39	15.97	0.56	35.86	1.68	4.68
8	127	54.11	15.55	0.54	38.02	3.31	8.71
9	139.5	51.99	14.02	0.49	37.48	12.85	34.29
10	146.5	53.53	15.96	0.56	37.01	4.87	13.16
11	158	53.35	16.12	0.56	36.67	20.88	56.95
1a	161.5	50.46	12.37	0.43	37.66	20.70	54.97
12	164.5	52.60	15.66	0.55	36.39	3.67	10.08
2a	170	44.55	12.08	0.42	32.05	8.94	27.90
13	176.5	53.55	16.67	0.58	36.30	3.50	9.64
14	197	52.11	14.62	0.51	36.98	5.19	14.04
15	211	56.18	14.67	0.51	41.00	3.52	8.59
3a	218.5	54.19	14.45	0.51	39.23	3.14	8.00
16	223.5	55.99	15.16	0.53	40.30	2.78	6.90
4a	238.5	41.39	11.65	0.41	29.33	7.32	24.96
17	243.5	54.00	14.90	0.52	38.58	2.52	6.53
18	254.5	51.98	14.54	0.51	36.93	3.53	9.56
5a	258	43.92	11.94	0.42	31.56	11.92	37.77
6a	263.5	48.78	14.05	0.49	34.24	1.92	5.61
19	274	52.52	15.97	0.56	35.99	1.81	5.03
20	293.5	53.25	14.40	0.50	38.35	5.41	14.11
7a	299.5	60.12	17.56	0.61	41.95	3.71	8.84
21	313.5	57.01	16.14	0.56	40.31	1.74	4.32
8a	323.5	48.25	13.41	0.47	34.37	2.47	7.19
22	333.5	56.89	15.39	0.54	40.96	2.56	6.25
9a	346.5	46.87	13.89	0.49	32.49	9.68	29.79
23	353.5	51.50	14.42	0.50	36.58	2.35	6.43
10a	364.5	55.35	15.37	0.54	39.44	7.55	19.14
24	370.5	56.91	15.35	0.54	41.02	3.43	8.36
25	380.5	50.56	13.16	0.46	36.94	3.79	10.26
11a	386.5	40.45	10.97	0.38	29.10	3.25	11.17
26	402.5	51.25	12.31	0.43	38.51	14.65	38.04

Table 2A. 01PC Sediment Sample Weights, Continued

#	depth (cm)	sample wt (g)	water wt. (g)	salt wt. (g)	sediment wt. (g)	>63μm wt. (g)	wt. % coarse
12a	410	53.60	14.93	0.52	38.15	6.27	16.44
13a	413.5	76.33	21.63	0.76	53.94	9.93	18.41
14a	418	52.80	13.92	0.49	38.39	14.30	37.25
27	422.5	51.46	14.53	0.51	36.42	2.46	6.75
28	433.5	58.88	16.28	0.57	42.03	2.15	5.12
15a	437	50.59	12.60	0.44	37.55	15.52	41.33
29	442	59.12	18.43	0.65	40.04	2.51	6.27
16a	455	53.08	12.43	0.44	40.21	9.26	23.03
30	460.5	52.70	13.75	0.48	38.47	5.85	15.21
31	471	56.59	12.75	0.45	43.39	22.23	51.23
32	480.5	54.47	11.25	0.39	42.83	24.79	57.89
17a	490	46.44	11.68	0.41	34.35	19.61	57.09
18a	493	45.01	13.44	0.47	31.10	6.73	21.64
33	500.5	54.62	14.87	0.52	39.23	3.27	8.34

Table 2B. 02PC Sediment Sample Weights

#	depth (cm)	sample wt (g)	water wt. (g)	salt wt. (g)	sediment wt. (g)	>63μm wt. (g)	wt. % coarse
1	3	49.93	17.26	0.60	32.07	0.49	1.53
2	20.5	52.33	16.02	0.56	35.75	0.75	2.10
3	32.5	50.10	17.60	0.62	31.88	0.27	0.85
4	39.5	54.39	19.98	0.70	33.71	0.43	1.28
5	55	56.96	18.15	0.64	38.17	1.07	2.80
6	68	51.62	17.01	0.60	34.01	0.11	0.32
7	71.5	50.07	15.68	0.55	33.84	0.50	1.48
8	78.5	50.82	15.38	0.54	34.90	0.62	1.78
9	87.5	52.58	16.76	0.59	35.23	0.53	1.50
10	107	50.89	15.46	0.54	34.89	1.12	3.21
11	127.5	48.93	15.30	0.54	33.09	0.63	1.90
12	142	50.05	15.19	0.53	34.33	0.44	1.28
1a	145.5	50.46	14.34	0.50	35.62	3.87	10.87
13	167.5	51.13	15.24	0.53	35.36	0.28	0.79
14	187.5	50.10	16.33	0.57	33.20	0.32	0.96
15	207.5	49.38	15.41	0.54	33.43	0.25	0.75
16	158	57.88	17.78	0.62	39.48	0.72	1.82
2a	178.5	51.94	15.30	0.54	36.10	2.18	6.04
17	197.5	51.68	16.49	0.58	34.61	0.28	0.81
3a	202	53.72	14.20	0.50	39.02	2.29	5.87
18	220	53.61	14.92	0.52	38.17	0.52	1.36
4a	226.5	49.78	14.06	0.49	35.23	4.71	13.37
5a	238	50.28	15.41	0.54	34.33	1.54	4.49
19	243.5	52.13	15.90	0.56	35.67	0.37	1.04
20	260	55.79	15.96	0.56	39.27	0.54	1.38
21	276	50.25	14.49	0.51	35.25	0.54	1.53
6a	280	49.52	14.98	0.52	34.02	2.05	6.03
22	289	50.33	16.69	0.58	33.06	0.26	0.79
23	309.5	55.02	15.93	0.56	38.53	1.35	3.50
7a	313	49.09	13.60	0.48	35.01	6.17	17.62
24	330	53.17	16.86	0.59	35.72	0.35	0.98
25	349.5	53.64	16.63	0.58	36.43	0.49	1.35
26	356.5	50.80	15.25	0.53	35.02	1.28	3.66
27	370.5	52.66	15.60	0.55	36.51	0.31	0.85
8a	374	49.55	14.01	0.49	35.05	2.82	8.05
28	384.5	51.95	18.16	0.64	33.15	0.19	0.57
29	391	53.77	16.84	0.59	36.34	0.26	0.72

Table 2B. 02PC Sediment Sample Weights, Continued

#	depth (cm)	sample wt (g)	water wt. (g)	salt wt. (g)	sediment wt. (g)	>63μm wt. (g)	wt. % coarse
30	400	50.24	15.29	0.54	34.41	0.35	1.02
31	413.5	51.44	15.29	0.54	35.61	0.69	1.94
32	426	50.07	13.84	0.48	35.75	0.80	2.24
9a	427	48.25	13.29	0.47	34.49	2.75	7.97
33	435.5	50.57	16.18	0.57	33.82	0.20	0.59
34	451.5	46.93	18.22	0.64	28.07	2.69	9.58
35	457	50.25	15.38	0.54	34.33	0.44	1.28
36	475	50.85	15.01	0.53	35.31	0.72	2.04
37	489.5	49.02	14.19	0.50	34.33	0.48	1.40
38	503	51.60	15.04	0.53	36.03	0.49	1.36
40	516.5	53.70	14.90	0.52	38.28	2.50	6.53
10a	526.5	50.45	15.04	0.53	34.88	1.80	5.16
41	536	53.66	16.91	0.59	36.16	0.92	2.54
42	554	53.83	13.95	0.49	39.39	9.40	23.86
43	561	56.32	17.37	0.61	38.34	0.99	2.58
11a	571.5	46.66	14.01	0.49	32.16	6.64	20.65
44	599	54.57	14.27	0.50	39.80	1.75	4.40
45	608.5	52.81	16.93	0.59	35.29	0.76	2.15
12a	616	52.51	16.82	0.59	35.10	2.63	7.49
46	628.5	51.95	15.83	0.55	35.57	0.86	2.42
13a	636	51.46	14.87	0.52	36.07	4.08	11.31
47	642	54.13	15.10	0.53	38.50	0.86	2.23
48	651	52.48	13.56	0.47	38.45	0.86	2.24
14a	667.5	66.16	17.51	0.61	48.04	4.22	8.78
49	671	51.53	14.05	0.49	36.99	0.78	2.11
50	691	53.39	14.41	0.50	38.48	0.62	1.61
15a	695.5	49.91	13.47	0.47	35.97	3.57	9.93
51	703	53.87	14.78	0.52	38.57	0.73	1.89
52	722.5	53.14	13.47	0.47	39.20	1.36	3.47
53	733.5	53.69	16.59	0.58	36.52	0.40	1.10
54	751	56.36	16.36	0.57	39.43	0.46	1.17
16a	754	40.06	11.59	0.41	28.06	1.56	5.56
55	756.5	54.34	16.22	0.57	37.55	0.44	1.17
56	775	54.25	14.63	0.51	39.11	0.61	1.56

Table 2C. 07PC Sediment Sample Weights

#	depth (cm)	sample wt (g)	water wt. (g)	salt wt. (g)	sediment wt. (g)	>63μm wt. (g)	wt. % coarse
1	6.5	55.58	20.83	0.73	34.02	2.12	6.23
1a	20.5	49.92	17.41	0.61	31.90	1.87	5.86
2	26.5	56.68	20.35	0.71	35.62	3.75	10.53
3	46.5	52.40	17.10	0.60	34.70	6.46	18.62
4	66.5	47.51	16.29	0.57	30.65	5.11	16.67
5	86	58.79	17.15	0.60	41.04	9.07	22.10
2a	90	51.82	15.26	0.53	36.03	7.63	21.18
6	97	55.03	16.86	0.59	37.58	7.55	20.09
7	117.5	61.23	18.49	0.65	42.09	7.84	18.63
8	137.5	62.40	17.17	0.60	44.63	8.24	18.46
9	159	50.52	13.70	0.48	36.34	7.16	19.70
10	177.5	49.40	13.07	0.46	35.87	6.44	17.95
11	191	56.67	14.56	0.51	41.60	8.12	19.52
12	211	48.11	12.82	0.45	34.84	7.94	22.79
13	229.5	43.74	11.70	0.41	31.63	3.24	10.24
3a	231.5	59.97	15.36	0.54	44.07	4.44	10.07
4a	237.5	53.75	14.71	0.51	38.53	3.07	7.97
14	251	52.51	14.33	0.50	37.68	7.36	19.53
15	271	52.05	15.53	0.54	35.98	4.93	13.70
16	290.5	48.39	14.36	0.50	33.53	2.59	7.73
5a	294	52.04	15.65	0.55	35.84	2.69	7.51
17	311	51.67	14.13	0.49	37.05	7.51	20.27
18	328	52.40	13.74	0.48	38.18	4.51	11.81
6a	344	53.41	13.18	0.46	39.77	6.95	17.48
19	350	57.54	16.11	0.56	40.87	1.97	4.82
7a	362	54.17	13.50	0.47	40.20	3.07	7.64
8a	366	49.32	13.66	0.48	35.18	2.34	6.65
20	370	54.69	14.79	0.52	39.38	4.47	11.35
9a	378.5	56.09	14.06	0.49	41.54	5.61	13.51
10a	382	51.69	14.12	0.49	37.08	2.01	5.42
21	390	47.17	12.92	0.45	33.80	3.61	10.68
11a	397	60.06	15.14	0.53	44.39	2.79	6.29
12a	400.5	54.57	14.64	0.51	39.42	1.44	3.65
22	410	50.18	12.99	0.45	36.74	4.23	11.51
13a	415.5	54.26	15.25	0.53	38.48	3.34	8.68
14a	424.5	54.37	14.38	0.50	39.49	3.72	9.42
23	430	50.36	14.21	0.50	35.65	5.97	16.74

Table 2C. 07PC Sediment Sample Weights, Continued

#	depth (cm)	sample wt (g)	water wt. (g)	salt wt. (g)	sediment wt. (g)	>63μm wt. (g)	wt. % coarse
24	453	57.58	14.89	0.52	42.17	17.32	41.07
15a	456.5	51.78	13.35	0.47	37.96	7.19	18.94
25	470	53.56	12.27	0.43	40.86	14.73	36.05
16a	475.5	59.68	16.13	0.56	42.99	5.78	13.45
17a	490	70.30	16.47	0.58	53.25	21.68	40.71
26	494	89.14	23.64	0.83	64.67	10.08	15.59
27	507	87.31	20.73	0.73	65.85	13.13	19.94
18a	519	63.09	15.52	0.54	47.03	8.72	18.54
28	522	48.89	12.55	0.44	35.90	3.80	10.58
29	542	51.15	13.68	0.48	36.99	1.59	4.30
19a	555.5	48.82	12.96	0.45	35.41	2.46	6.95
30	562	61.08	17.02	0.60	43.46	1.91	4.39
31	582	44.96	11.82	0.41	32.73	2.83	8.65
20a	594	48.93	12.56	0.44	35.93	4.14	11.52
21a	598	61.65	16.40	0.57	44.68	3.81	8.53
32	602	46.74	11.89	0.42	34.43	3.46	10.05
22a	616	58.50	12.45	0.44	45.61	29.63	64.96
23a	620	62.24	15.40	0.54	46.30	4.13	8.92
33	627	44.77	11.61	0.41	32.75	2.79	8.52
34	647	50.45	13.38	0.47	36.60	3.15	8.61
24a	653	50.51	12.83	0.45	37.23	4.90	13.16
25a	659.5	48.33	13.68	0.48	34.17	1.91	5.59
35	667	49.79	15.36	0.54	33.89	3.33	9.83
36	687	51.63	12.99	0.45	38.19	3.08	8.07
26a	693	58.41	16.08	0.56	41.77	1.65	3.95
37	707	44.96	12.63	0.44	31.89	1.90	5.96
38	727	48.49	12.64	0.44	35.41	5.25	14.83
27a	740.5	57.47	15.11	0.53	41.83	3.47	8.30
39	747	53.89	15.00	0.53	38.37	5.13	13.37

Table 3A. 01PC Volumetric Percentages of the Sediment Fine-fraction

#	depth (cm)	colloidal clay (% <1um)	clay (% 1-4um)	silt (% 4-63um)
1	12.5	1.36	41.35	57.30
2	32.5	0.76	27.15	72.10
3	52.5	0.61	22.54	76.85
4	62.5	0.60	20.29	79.11
5	76.5	0.43	16.64	82.93
6	87.5	0.49	17.68	81.82
7	105.5	1.10	35.02	63.88
8	127	1.08	31.11	67.82
9	139.5	1.18	35.19	63.63
10	146.5	0.42	17.86	81.72
11	158	1.02	32.77	66.21
12	164.5	0.37	17.29	82.33
13	176.5	0.32	37.37	62.31
14	197	0.20	31.44	68.35
15	211	0.30	38.31	61.39
16	223.5	0.28	37.34	62.38
17	243.5	0.13	22.60	77.27
18	254.5	0.14	22.68	77.18
19	274	0.24	32.32	67.44
20	293.5	0.13	23.06	76.81

Table 3B. 02PC Volumetric Percentages of the Sediment Fine-fraction

#	depth (cm)	colloidal clay (% <1um)	clay (% 1-4um)	silt (% 4-63um)
1	3	3.84	38.38	57.79
2	20.5	1.20	28.88	69.91
3	32.5	1.34	45.03	53.63
4	39.5	0.17	10.13	89.70
5	55	1.33	38.27	60.40
6	68	1.58	44.51	53.91
7	71.5	1.25	38.70	60.05
8	78.5	0.81	26.32	72.88
9	87.5	0.85	28.26	70.89
10	107	0.90	29.67	69.43
11	127.5	0.93	30.68	68.40
12	142	1.16	32.00	66.84
16	158	2.09	29.97	67.93
13	167.5	1.19	34.41	64.40
14	187.5	1.07	32.97	65.96
17	197.5	1.96	27.73	70.30
15	207.5	1.18	30.14	68.68
18	220	1.15	14.83	84.02
19	243.5	2.26	31.17	66.57
20	260	2.24	30.55	67.21
21	276	0.70	20.95	78.36
22	289	0.87	24.69	74.44
23	309.5	0.75	24.18	75.07
24	330	1.08	33.82	65.10
25	349.5	0.59	19.42	79.99
26	356.5	0.52	25.16	74.32
27	370.5	5.98	30.52	63.51
28	384.5	4.91	29.53	65.56
29	391	6.23	30.85	62.93
30	400	7.92	40.58	51.50
31	413.5	5.32	27.90	66.78
32	427	5.56	25.92	68.53
33	435.5	6.33	33.93	59.73
34	451.5	5.27	29.09	65.63
35	457	5.52	29.44	65.04
36	475	6.66	34.14	59.20
37	489.5	5.78	29.55	64.66
38	503	3.79	24.54	71.67
39	516.5	5.41	32.36	62.23

Table 3B. 02PC Volumetric Percentages of the Sediment Fine-fraction, Continued

#	depth (cm)	colloidal clay (% <1um)	clay (% 1-4um)	silt (% 4-63um)
40	536	6.00	34.19	59.81
41	554	6.97	33.57	59.46
42	561	5.70	34.49	59.81
43	599	5.30	31.63	63.07
44	608.5	4.85	28.50	66.64
45	628.5	4.88	33.09	62.04
46	642	4.69	28.56	66.75
47	651	5.99	35.03	58.98
48	671	5.24	30.82	63.94
49	691	4.73	30.73	64.55
50	703	5.81	33.36	60.84
51	722.5	4.97	32.75	62.28
52	733.5	5.67	35.05	59.28
53	751	4.80	32.75	62.44
54	756.5	1.18	11.87	86.95
55	775	3.36	23.54	73.11

Table 4. Radiocarbon Data for Marine and Terrestrial Carbon

Core #	Sample depth (cm)	Material dated	Lab reported ages (^{14}C yr BP ± ε)$^{\#}$
01PC	20.5	marine carbonate	1890 ± 30
	52.5	marine carbonate	2430 ± 30
	63.5	marine carbonate	2510 ± 35
	87.5	marine carbonate	2840 ± 35
	168	marine carbonate	3320 ± 35
	208	marine carbonate	3360 ± 35
	257.5	marine carbonate	3740 ± 40
	268	marine carbonate	3780 ± 35
	324.5	marine carbonate	3960 ± 40
	391.5	marine carbonate	4230 ± 40
02PC	23.5	terrestrial plant debris	345 ± 30
	23.5	terrestrial plant debris	1460 ± 25
	23.5	terrestrial plant debris	2810 ± 20
	37.5	foraminiferal microfossil	850 ± 65
	49.5	marine carbonate	850 ± 30
	57.5	foraminiferal microfossil	1150 ± 65
	67	marine carbonate	1250 ± 30
	72.5	foraminiferal microfossil	1010 ± 45
	79	foraminiferal microfossil	1100 ± 55
	85	marine carbonate	1080 ± 35
	88	foraminiferal microfossil	1250 ± 55
	109.5	terrestrial plant debris	1270 ± 30
	115	marine carbonate	1450 ± 35
	128	marine carbonate	1390 ± 35
	130	marine carbonate	1420 ± 30
	147.5	marine carbonate	1620 ± 30
	170	marine carbonate	1740 ± 35
	221	foraminiferal microfossil	1930 ± 80
	224.5	marine carbonate	1390 ± 25
	231.5	marine carbonate	1940 ± 30
	287.5	marine carbonate	2280 ± 35
	310	marine carbonate	2430 ± 35
	324	marine carbonate	2460 ± 35
	365.5	marine carbonate	2670 ± 30
	419.5	marine carbonate	2890 ± 40
	450.5	terrestrial plant debris	2410 ± 30
	450.5	terrestrial plant debris	2800 ± 25

Table 4. Radiocarbon Data for Marine and Terrestrial Carbon, Continued

Core #	Sample depth (cm)	Material dated	Lab reported ages (^{14}C yr BP ± ε)#
02PC	504.5	foraminiferal microfossil	3100 ± 90
	529.5	marine carbonate	3150 ± 35
	583.5	terrestrial plant debris	2300 ± 30
	583.5	terrestrial plant debris	2680 ± 20
	583.5	terrestrial plant debris	3330 ± 25
	621.5	marine carbonate	3370 ± 40
	638	marine carbonate	3200 ± 30
	669	marine carbonate	3360 ± 30
	670	foraminiferal microfossil	3610 ± 55
	701.5	foraminiferal microfossil	3590 ± 55
	710	terrestrial plant debris	3040 ± 55
	732	marine carbonate	3710 ± 40

Radiocarbon dating was performed at National Ocean Sciences Accelerator Mass Spectrometry (NOSAMS) Facility at Woods Hole Oceanographic Institution.

Table 5. Particulate Organic Carbon Layers (>90% by volume)

All dates in yr BP (1950), calibrated for reservoir corrections (350 yrs)

01PC				02PC				07PC	
depth (cm)	**thickness (cm)**	**Two Dates**	**All Dates**	**depth (cm)**	**thickness (cm)**	**Two Dates**	**All Dates**	**depth (cm)**	**thickness (cm)**
153.5-154.5	1	3240	3189 (3075-3299)	15-15.5	0.5	-	740 (625-984)	21.5-22.5	1
157-157.5	0.5	3257	3203 (3089-3313)	20-20.5	0.5	-	769 (653-1013)	234-234.5	0.5
159-159.5	0.5	3269	3212 (3099-3323)	23.5-24	0.5	-	789 (674-1033)	439	< 0.5
167-167.5	0.5	3317	3249 (3136-3360)	26-26.5	0.5	-	803 (689-1047)	441	< 0.5
168-168.5	0.5	3321	3254 (3141-3365)	56-58	2	944	984 (869-1228)	442	< 0.5
199	< 0.5	3351	3396 (3283-3507)	65-66.5	1.5	983	1033 (917-1277)	443	< 0.5
200	< 0.5	3352	3401 (3288-3512)	70-71.5	1.5	1005	1062 (946-1306)	446-446.5	0.5
200.5-201	0.5	3353	3405 (3292-3516)	107.5-108	0.5	1320	1271 (1155-1515)	448.5	< 0.5
249-251	2	3690	3639 (3525-3750)	112.5-113	0.5	1338	1300 (1184-1544)	450	< 0.5
393-396	3	-	4315 (4202-4426)	144.5-145	0.5	1591	1483 (1368-1727)	451	< 0.5
397-398.5	1.5	-	4327 (4213-4438)	203-204	1	1867	1822 (1706-2066)	673.5-676.5	3
448.5-449	0.5	-	4562 (4449-4673)	354-359	5	2637	2636 (2394-2800)		
467-469	2	-	4656 (4542-4766)	419-420	1	2838	2806 (2564-2970)		
475-477	2	-	4693 (4580-4804)	450-450.5	0.5	2967	2890 (2649-3055)		
504-504.5	0.5	-	4821 (4708-4932)	543.5-545.5	2	3188	3155 (2913-3312)		
506-508	2	-	4837 (4724-4948)	548-548.5	0.5	3195	3163 (2921-3327)		
				579.5-587.5	8	3289	3271 (3029-3435)		
				591-593	2	3302	3287 (3045-3451)		
				600.5-602	1.5	3323	3312 (3070-3476)		
				710-710.5	0.5	3625	3613 (3371-3777)		

- no radiocarbon data available for dating using this method (see text).

Table 6. Fining-upward Package Analysis

Core #	# visually defined	# w/ distinct contact	# exhibiting normal grading	# w/ bioturb. at contact	# w/ bioturb. that do not exhibit grading	# w/ bioturb. and no contact	total # after redefining
01PC	16	13	14	3	1 of 2	0 of 3	14
02PC	15	13	13	9	2 of 2	2 of 2	17
07PC	19	13	14	14	5 of 5	5 of 6	18

Table 7. Fining-upward Packages

All dates in yr BP (1950), calibrated for reservoir corrections (350 yrs)

Core #		Depths (cm)	Two Dates	All Dates	Ages w/ Error	Thickness (cm)	Age Span
01PC		54	2441	2405	2336-2482	-	-
		91.5	2864	2895	2781-3006	37.5	490
		142	3165	3130	3017-3241	50.5	236
		161.5	3281	3221	3108-3332	19.5	91
		170.5	3323	3263	3150-3374	9	42
	*	221	3460	3499	3386-3610	-	-
	†	239	3598	3583	3469-3694	68.5	320
		259	3746	3676	3563-3787	20	93
		294	3863	3839	3726-3950	35	163
		348	4055	4091	3978-4202	54	252
		366	4127	4175	4062-4286	18	84
		406	-	4362	4248-4472	40	187
		418.5	-	4420	4307-4531	12.5	58
		438	-	4511	4397-4622	19.5	91
		458	-	4604	4491-4715	20	93
	*	478	-	4698	4584-4808	-	-
		491	-	4758	4645-4869	33	154
02PC		80	1117	1110	995-1354	-	-
	†	145.5	1597	1486	1370-1730	65.5	480
		228	1967	1959	1844-2203	82.5	370
		280	2240	2258	2142-2502	52	273
	†	313	2436	2447	2332-2691	33	196
	†	359	2637	2636	2394-2800	46	201
		376	2712	2683	2441-2847	17	75
		428.5	2912	2829	2587-2993	52.5	200
		453	2973	2897	2655-3061	24.5	61
		476	3030	2961	2719-3125	23	57
		520.5	3132	3085	2843-3249	44.5	102
		555.5	3212	3182	2940-3346	35	80
		593	3302	3287	3044-3451	37.5	90
		637.5	3414	3410	3168-3574	44.5	112
		669.5	3502	3499	3257-3663	32	88
		696.5	3570	3574	3332-3738	27	68
		726.5	3688	3658	3416-3822	30	118
		751.5	-	3727	3485-3891	25	69

* Boundaries were defined visually and excluded based on grain size distribution.

† Boundaries that were added based on grain size distribution.

- No radiocarbon data available for dating using the two-date method.

The method using all radiocarbon data is calculated based on linear regressions to find average accumulation rates. Refer to the text for explanations of the different dating methods.

Table 7. Fining-upward Packages, Continued

All dates in yr BP (1950), calibrated for reservoir corrections (350 yrs)

Core #		Depths (cm)	Thickness (cm)
07PC	†	55	-
		94.5	39.5
	†	220.5	126
	*	235.5	-
	†	275	54.5
	*	291.5	-
		345	70
		363	18
		380.5	17.5
		397.5	17
		413.5	16
	*	426.5	-
		454	40.5
		472.5	18.5
		490.5	18
		521.5	31
		559.5	38
		595	35.5
		618.5	23.5
		657	38.5
		689.5	32.5
		727.5	38

* Boundaries were defined visually and excluded based on grain size distribution.

† Boundaries that were added based on grain size distribution.

These tables, in part, are currently being prepared for submission for publication of the material. McCullough, Justin S.; Driscoll, Neal W. The thesis author was the primary investigator and author of this material.